

EFFECT OF CONSTITUTIVE MODELING IN SHEET METAL FORMING

A THESIS SUBMITTED TO  
THE GRADUATE SCHOOL OF NATURAL AND APPLIED SCIENCES  
OF  
MIDDLE EAST TECHNICAL UNIVERSITY

BY

MERİÇ UÇAN

IN PARTIAL FULFILLMENT OF THE REQUIREMENTS  
FOR  
THE DEGREE OF MASTER OF SCIENCE  
IN  
MECHANICAL ENGINEERING

JULY 2011

Approval of the thesis:

**EFFECT OF CONSTITUTIVE MODELING IN SHEET METAL FORMING**

submitted by **MERİÇ UÇAN** in partial fulfilment of the requirements for the degree of **Master of Science in Mechanical Engineering, Middle East Technical University** by,

Prof. Dr. Canan Özgen  
Dean, Graduate School of **Natural and Applied Sciences** \_\_\_\_\_

Prof. Dr. Suha Oral  
Head of the Department, **Mechanical Engineering** \_\_\_\_\_

Prof. Dr. Haluk Darendeliler  
Supervisor, **Mechanical Engineering Dept., METU** \_\_\_\_\_

**Examining Committee Members:**

Prof. Dr. Metin Akkök  
Mechanical Engineering Dept., METU \_\_\_\_\_

Prof. Dr. Haluk Darendeliler  
Mechanical Engineering Dept., METU \_\_\_\_\_

Prof. Dr. Suha Oral  
Mechanical Engineering Dept., METU \_\_\_\_\_

Prof. Dr. Can Çoğun  
Mechanical Engineering Dept., METU \_\_\_\_\_

Prof. Dr. Yavuz Yaman  
Aerospace Engineering Dept., METU \_\_\_\_\_

**Date:** July 21st, 2011

**I hereby declare that all information in this document has been obtained and presented in accordance with academic rules and ethical conduct. I also declare that, as required by these rules and conduct, I have fully cited and referenced all material and results that are not original to this work.**

Name, Last name: Meriç Uçan

Signature:

## **ABSTRACT**

### **EFFECT OF CONSTITUTIVE MODELING IN SHEET METAL FORMING**

Uçan, Meriç

M.Sc., Department of Mechanical Engineering

Supervisor: Prof. Dr. Haluk Darendeliler

July 2011, 134 pages

This study focuses on the effects of different constitutive models in sheet metal forming operations by considering the cylindrical and square cup drawing and V-bending simulations. Simulations are performed using eight different constitutive models; elastic plastic constitutive model with isotropic hardening, elastic plastic constitutive model with kinematic hardening, elastic plastic constitutive model with combined hardening, power law isotropic plasticity, piecewise linear isotropic plasticity, Barlat three-parameter, cyclic elastoplastic and Hill'48 model. The numerical analyses are accomplished by using three different 1 mm thick sheet materials; St12 steel, Al-5182 aluminum and stainless steel 409 Ni. An explicit finite element code is used in the simulations. For square cup drawing, three different blank holder forces; 2 kN, 4 kN and 5 kN are considered for St12 steel, whereas only 5 kN blank holder force is applied for stainless steel 409 Ni and Al-5182 aluminum.

A number of experiments are carried out and analytical calculations are utilized to evaluate the results of simulations. In cylindrical cup drawing, simulation results of different constitutive models show good agreement with analytical calculations for thickness strain and effective stress distributions. In square cup drawing, simulation results of all the models displayed good agreement with the experimental results for

edge contour comparisons, although the distributions of effective stress vary for different models within the cup. The numerically and experimentally obtained springback amounts are also in good agreement. The simulation results obtained for piecewise linear isotropic plasticity and power law isotropic plasticity models show better agreement with the analytical solutions and experiments.

**Keywords:** Constitutive Models, Hardening Laws, Deep Drawing, Springback, Sheet Metals, Finite Element Method

## ÖZ

### BÜNYE DENKLEMLERİNİN SAC METAL ŞEKİLLENDİRME ÜZERİNDEKİ ETKİSİ

Uçan, Meriç

Yüksek Lisans, Makina Mühendisliği Bölümü  
Tez Yöneticisi: Prof. Dr. Haluk Darendeliler

Temmuz 2011, 134 sayfa

Bu çalışmada metal levha şekillendirme işlemlerinde bünye modellerin etkisi incelenmiş ve bu amaçla aksel simetrik ve kare levha çekme ile V-bükme işlemlerinin simülasyonları yapılmıştır. Simülasyonlar sekiz değişik bünye modeli için uygulanmıştır. Numerik analizler 1 mm kalınlığında üç değişik malzeme; St12 çelik, Al-5182 alüminyum ve paslanmaz çelik 409 Ni kullanılarak gerçekleştirilmiştir. Simülasyonlarda açık sonlu eleman kodu kullanılmıştır. Kare levha çekme işleminde, St12 çeliği için 2 kN, 4 kN ve 5 kN'luk üç değişik pot çember kuvveti uygulanmış ancak, paslanmaz çelik ve Al-5182 alüminyum için sadece 5 kN'luk pot çember kuvveti uygulanmıştır.

Simülasyon sonuçlarını değerlendirmek için çeşitli deneyler gerçekleştirilmiş ve analitik hesaplamalar yapılmıştır. Silindirik levha çekme işlemi için değişik bünye modelleri kullanılarak elde edilen simülasyon sonuçları, kalınlık gerinim ve eşdeğer gerilme dağılımları göz önüne alındığında analitik hesaplama sonuçları ile tutarlılık göstermektedir. Kare levha çekme işlemlerinde, simülasyonlar ve deneyler ile elde edilen şekillendirilmiş levhaların kenar geometrileri tutarlı olmasına rağmen eşdeğer gerilme dağılımları şekillendirilmiş levha içerisinde değişik modeller için farklılık

göstermektedir. Nümerik ve deneysel olarak elde edilen geri yaylanma miktarlarıda tutarlılık göstermektedir. Parçalı doğrusal plastisite ve Swift kanunu bağlantılı plastisite bünye modelleri ile elde edilen simülasyon sonuçları, analitik sonuçlar ve deneyler ile tutarlılık göstermektedir.

**Anahtar Kelimeler:** Bünye Denklemleri, Sertleştirme Yasaları, Derin Çekme, Geri Yaylanma, Sac Metal, Sonlu Elemanlar Metodu

**To My Family**

## ACKNOWLEDGEMENTS

First and foremost, I would like to express my gratitude to my supervisor Prof. Dr. Haluk Darendeliler for his continuous guidance, excellent advice and insight throughout the study.

The author was supported by TÜBİTAK. I owe TÜBİTAK a great debt of gratitude for their pillar of support during my study.

I also would like to thank to director of METU-BILTİR Research and Application Center, Prof. Dr. Mustafa İlhan Gökler for providing me access all necessary research applications performed during the study.

I wish to thank to my friends Remzi Çöl, Selim Gürgen, Ulaş Göçmen, Sinem Demirkaya, Başak Orhan, Sevgi Saraç and Tuğra Erol. Further, thanks go to Servet Şehirli, Mehmet Ali Sarıhan and Mehmet Erili for their valuable support and assistance.

I also would like to thank to my aunts, my uncles and my cousins for their encouragement and faith in me.

Last, I owe my deepest gratitude to my family: my parents, Naciye and Erdal Uçan and my brothers, Serkan and Raşit Uçan for the support they provided me through my entire life and encouragement to pursue my interests and believing in me.

## TABLE OF CONTENTS

ABSTRACT.....	iv
ÖZ.....	vi
ACKNOWLEDGEMENTS.....	ix
TABLE OF CONTENTS.....	x
LIST OF TABLES.....	xiii
LIST OF FIGURES.....	xiv
CHAPTERS	
1. INTRODUCTION.....	1
1.1 Sheet Forming Operations.....	2
1.1.1 Bending.....	3
1.1.2 Stretch Forming.....	4
1.1.3 Deep Drawing.....	4
1.2 Constitutive Modeling.....	9
1.3 Scope of Thesis.....	10
2. LITERATURE SURVEY.....	11
3. FINITE ELEMENT METHOD .....	21
3.1 Introduction to Finite Element Method.....	21
3.1.1 Geometrical Nonlinearity.....	23
3.1.2 Material Nonlinearity.....	23
3.1.3 Nonlinear Boundary Conditions.....	24
3.2 Large Displacement and Large Strain Behavior.....	24
3.3 Explicit and Implicit Time Integration.....	25

3.4 Finite Element Formulation.....	26
4. CONSTITUTIVE MODELS.....	28
4.1 Introduction to Constitutive Models.....	28
4.2 Introduction to Plastic Anisotropy.....	30
4.3 Hardening Rules.....	31
4.3.1 Perfect Plasticity.....	32
4.3.2 Isotropic Hardening.....	32
4.3.3 Kinematic Hardening.....	34
4.3.4 Combined Hardening.....	35
4.4 Yield Functions.....	36
4.4.1 von Mises Yield Function.....	36
4.4.2 Hill'48 Yield Criterion.....	36
4.4.3 Hill's 1979 Yield Criterion.....	39
4.4.4 Hill's 1990 Yield Criterion.....	40
4.4.5 Hill's 1993 Quadratic Anisotropy Yield Criterion.....	40
4.4.6 Hosford's Yield Criterion.....	42
4.4.7 Barlat's 1991 Yield Criterion.....	42
4.4.8 Barlat's 1994 Yield Criteria.....	43
4.4.9 Barlat's 1996 Yield Criteria.....	44
4.4.10 Barlat's Yld2000-2D Yield Criterion.....	46
4.5 Stress Strain Relations in Plastic Range.....	47
4.5.1 Elastic Plastic Model with Isotropic, Kinematic and Combined Hardening.....	47
4.5.2 Power Law Isotropic Plasticity.....	49
4.5.3 Piecewise Linear Isotropic Plasticity.....	50

4.5.4	Barlat Three-Parameter.....	51
4.5.5	Cyclic elastoplastic.....	55
4.5.6	Hill'48.....	55
5.	RESULTS .....	58
5.1	Introduction.....	58
5.2	Cylindrical Cup Drawing.....	60
5.3	Square Cup Drawing.....	65
5.3.1	Stainless Steel 409 Ni.....	71
5.3.2	Al-5182 Aluminum.....	80
5.3.3	St12 Steel.....	88
5.3.4	Comparison with Experiments.....	113
5.4	V-Bending .....	119
5.5	Comparison of the Results.....	121
6.	CONCLUSION AND FUTURE WORK.....	125
6.1	Conclusions.....	125
6.2	Future Works.....	126
	REFERENCES.....	128

## LIST OF TABLES

### TABLES

Table 5.1 Mechanical Properties of Used Materials.....	59
--	----

## LIST OF FIGURES

### FIGURES

Figure 1.1 Sheet metal forming examples in automotive industry.....	2
Figure 1.2 Bending forces during die bending.....	3
Figure 1.3 Stress distributions after bending.....	3
Figure 1.4 Stretch forming.....	4
Figure 1.5 Principle elements of deep drawing.....	5
Figure 1.6 Stress zones during deep drawing.....	5
Figure 1.7 Some examples of conventional deep drawing products.....	6
Figure 1.8 Typical failure modes in deep drawing: a) tearing, b) wrinkling, c) earing.....	6
Figure 1.9 Springback phenomenon .....	8
Figure 4.1 Schematics of coordinate systems of a sheet (X-Y-Z) and a sheet rolling directions.....	30
Figure 4.2 Uniaxial test and $\pi$ - plane representation of perfect plasticity.....	32
Figure 4.3 Uniaxial test and $\pi$ - plane representation of isotropic hardening.....	33
Figure 4.4 Uniaxial test and $\pi$ - plane representation of kinematic hardening and Bauschinger effect.....	34
Figure 4.5 Schematic view of combined hardening.....	35
Figure 4.6 Orientation of test specimen with the rolling direction of the sheet.....	38
Figure 4.7 Determination of the anisotropy parameter $2\theta$ from Mohr Circle.....	46
Figure 5.1 True stress vs. true strain curve for used materials.....	59

Figure 5.2 Dimensions of the die, blank holder and punch used in cylindrical cup deep drawing.....	60
Figure 5.3 FEM model used in cylindrical cup deep drawing.....	61
Figure 5.4 Section of partially drawn cup in cylindrical cup drawing.....	62
Figure 5.5 Effective stress distributions in cylindrical drawing.....	64
Figure 5.6 Thickness strain distributions in cylindrical drawing.....	64
Figure 5.7 Dimensions of the die, blank holder and punch used in square cup deep drawing.....	65
Figure 5.8 FEM model of square cup drawing.....	66
Figure 5.9 Thickness strain distribution of elastic plastic constitutive model with combined hardening for punch travel of 20 mm.....	67
Figure 5.10 Effective stress distribution of elastic plastic constitutive model with combined hardening for punch travel of 20 mm.....	68
Figure 5.11 Thickness strain distribution of elastic plastic constitutive model with combined hardening for punch travel of 25 mm.....	68
Figure 5.12 Effective stress distribution of elastic plastic constitutive model with combined hardening for punch travel of 25 mm.....	69
Figure 5.13 Thickness strain distribution of power law isotropic plasticity for punch travel of 20 mm.....	69
Figure 5.14 Effective stress distribution of power law isotropic plasticity for punch travel of 20 mm.....	70
Figure 5.15 Thickness strain distribution of power law isotropic plasticity for punch travel of 25 mm.....	70
Figure 5.16 Effective stress distribution of power law isotropic plasticity for punch travel of 25 mm.....	71
Figure 5.17 Comparison of the thickness strain distributions obtained for different models for 10 mm punch travel (Stainless steel 409 Ni, diagonal direction).....	72

Figure 5.18 Comparison of the effective stress distributions obtained for different models for 10 mm punch travel (Stainless steel 409 Ni, diagonal direction).....	72
Figure 5.19 Comparison of the thickness strain distributions obtained for different models for 10 mm punch travel (Stainless steel 409 Ni, transverse direction).....	73
Figure 5.20 Comparison of the effective stress distributions obtained for different models for 10 mm punch travel (Stainless steel 409 Ni, transverse direction).....	73
Figure 5.21 Comparison of the thickness strain distributions obtained for different models for 15 mm punch travel (Stainless steel 409 Ni, diagonal direction).....	74
Figure 5.22 Comparison of the effective stress distributions obtained for different models for 15 mm punch travel (Stainless steel 409 Ni, diagonal direction).....	74
Figure 5.23 Comparison of the thickness strain distributions obtained for different models for 15 mm punch travel (Stainless steel 409 Ni, transverse direction).....	75
Figure 5.24 Comparison of the effective stress distributions obtained for different models for 15 mm punch travel (Stainless steel 409 Ni, transverse direction).....	75
Figure 5.25 Comparison of the thickness strain distributions obtained for different models for 20 mm punch travel (Stainless steel 409 Ni, diagonal direction).....	76
Figure 5.26 Comparison of the effective stress distributions obtained for different models for 20 mm punch travel (Stainless steel 409 Ni, diagonal direction).....	76
Figure 5.27 Comparison of the thickness strain distributions obtained for different models for 20 mm punch travel (Stainless steel 409 Ni, transverse direction).....	77

Figure 5.28 Comparison of the effective stress distributions obtained for different models for 20 mm punch travel (Stainless steel 409 Ni, transverse direction).....	77
Figure 5.29 Comparison of the thickness strain distributions obtained for different models for 25 mm punch travel (Stainless steel 409 Ni, diagonal direction).....	78
Figure 5.30 Comparison of the effective stress distributions obtained for different models for 25 mm punch travel (Stainless steel 409 Ni, diagonal direction).....	78
Figure 5.31 Comparison of the thickness strain distributions obtained for different models for 25 mm punch travel (Stainless steel 409 Ni, transverse direction).....	79
Figure 5.32 Comparison of the effective stress distributions obtained for different models for 25 mm punch travel (Stainless steel 409 Ni, transverse direction).....	79
Figure 5.33 Comparison of the thickness strain distributions obtained for different models for 10 mm punch travel (Al-5182, diagonal direction).....	80
Figure 5.34 Comparison of the effective stress obtained for different models for 10 mm punch travel (Al-5182, diagonal direction).....	81
Figure 5.35 Comparison of the thickness strain distributions obtained for different models for 10 mm punch travel (Al-5182 transverse direction).....	81
Figure 5.36 Comparison of the effective stress obtained for different models for 10 mm punch travel (Al-5182, transverse direction).....	82
Figure 5.37 Comparison of the thickness strain distributions obtained for different models for 15 mm punch travel (Al-5182, diagonal direction).....	82
Figure 5.38 Comparison of the effective stress obtained for different models for 15 mm punch travel (Al-5182 diagonal direction).....	83
Figure 5.39 Comparison of the thickness strain distributions obtained for different models for 15 mm punch travel (Al-5182, transverse direction).....	83
Figure 5.40 Comparison of the effective stress obtained for different models for 15 mm punch travel (Al-5182, transverse direction).....	84

Figure 5.41 Comparison of the thickness strain distributions obtained for different models for 20 mm punch travel (Al-5182, diagonal direction).....	84
Figure 5.42 Comparison of the effective stress obtained for different models for 20 mm punch travel (Al-5182, diagonal direction).....	85
Figure 5.43 Comparison of the thickness strain distributions obtained for different models for 20 mm punch travel (Al-5182, transverse direction).....	85
Figure 5.44 Comparison of the effective stress obtained for different models for 20 mm punch travel (Al-5182, transverse direction).....	86
Figure 5.45 Comparison of the thickness strain distributions obtained for different models for 25 mm punch travel (Al-5182, diagonal direction).....	86
Figure 5.46 Comparison of the effective stress obtained for different models for 25 mm punch travel (Al-5182, diagonal direction).....	87
Figure 5.47 Comparison of the thickness strain distributions obtained for different models for 25 mm punch travel (Al-5182, transverse direction).....	87
Figure 5.48 Comparison of the effective stress obtained for different models for 25 mm punch travel (Al-5182, transverse direction).....	88
Figure 5.49 Comparison of the thickness strain distributions obtained for different models for 10 mm punch travel (St12 steel, diagonal direction, blank holder 2 kN).....	89
Figure 5.50 Comparison of the effective stress distributions obtained for different models for 10 mm punch travel (St12 steel, diagonal direction, blank holder 2 kN).....	89
Figure 5.51 Comparison of the thickness strain distributions obtained for different models for 10 mm punch travel (St12 steel, transverse direction, blank holder 2 kN).....	90
Figure 5.52 Comparison of the effective stress distributions obtained for different models for 10 mm punch travel (St12 steel, transverse direction, blank holder 2 kN).....	90
Figure 5.53 Comparison of the thickness strain distributions obtained for different models for 15 mm punch travel (St12 steel, diagonal direction, blank holder 2 kN).....	91

Figure 5.54 Comparison of the effective stress distributions obtained for different models for 15 mm punch travel (St12 steel, diagonal direction, blank holder 2 kN).....	91
Figure 5.55 Comparison of the thickness strain distributions obtained for different models for 15 mm punch travel (St12 steel, transverse direction, blank holder 2 kN).....	92
Figure 5.56 Comparison of the effective stress distributions obtained for different models for 15 mm punch travel (St12 steel, transverse direction, blank holder 2 kN).....	92
Figure 5.57 Comparison of the thickness strain distributions obtained for different models for 20 mm punch travel (St12 steel, diagonal direction, blank holder 2 kN).....	93
Figure 5.58 Comparison of the effective stress distributions obtained for different models for 20 mm punch travel (St12 steel, diagonal direction, blank holder 2 kN).....	93
Figure 5.59 Comparison of the thickness strain distributions obtained for different models for 20 mm punch travel (St12 steel, transverse direction, blank holder 2 kN).....	94
Figure 5.60 Comparison of the effective stress distributions obtained for different models for 20 mm punch travel (St12 steel, transverse direction, blank holder 2 kN).....	94
Figure 5.61 Comparison of the thickness strain distributions obtained for different models for 25 mm punch travel (St12 steel, diagonal direction, blank holder 2 kN).....	95
Figure 5.62 Comparison of the effective stress distributions obtained for different models for 25 mm punch travel (St12 steel, diagonal direction, blank holder 2 kN).....	95
Figure 5.63 Comparison of the thickness strain distributions obtained for different models for 25 mm punch travel (St12 steel, transverse direction, blank holder 2 kN).....	96

Figure 5.64 Comparison of the effective stress distributions obtained for different models for 25 mm punch travel (St12 steel, transverse direction, blank holder 2 kN).....	96
Figure 5.65 Comparison of the thickness strain distributions obtained for different models for 10 mm punch travel (St12 steel, diagonal direction, blank holder 4 kN).....	97
Figure 5.66 Comparison of the effective stress distributions obtained for different models for 10 mm punch travel (St12 steel, diagonal direction, blank holder 4 kN).....	97
Figure 5.67 Comparison of the thickness strain distributions obtained for different models for 10 mm punch travel (St12 steel, transverse direction, blank holder 4 kN).....	98
Figure 5.68 Comparison of the effective stress distributions obtained for different models for 10 mm punch travel (St12 steel, transverse direction, blank holder 4 kN).....	98
Figure 5.69 Comparison of the thickness strain distributions obtained for different models for 15 mm punch travel (St12 steel, diagonal direction, blank holder 4 kN).....	99
Figure 5.70 Comparison of the effective stress distributions obtained for different models for 15 mm punch travel (St12 steel, diagonal direction, blank holder 4 kN).....	99
Figure 5.71 Comparison of the thickness strain distributions obtained for different models for 15 mm punch travel (St12 steel, transverse direction, blank holder 4 kN).....	100
Figure 5.72 Comparison of the effective stress distributions obtained for different models for 15 mm punch travel (St12 steel, transverse direction, blank holder 4 kN).....	100
Figure 5.73 Comparison of the thickness strain distributions obtained for different models for 20 mm punch travel (St12 steel, diagonal direction, blank holder 4 kN).....	101

Figure 5.74 Comparison of the effective stress distributions obtained for different models for 20 mm punch travel (St12 steel, diagonal direction, blank holder 4 kN).....	101
Figure 5.75 Comparison of the thickness strain distributions obtained for different models for 20 mm punch travel (St12 steel, transverse direction, blank holder 4 kN).....	102
Figure 5.76 Comparison of the effective stress distributions obtained for different models for 20 mm punch travel (St12 steel, transverse direction, blank holder 4 kN).....	102
Figure 5.77 Comparison of the thickness strain distributions obtained for different models for 25 mm punch travel (St12 steel, diagonal direction, blank holder 4 kN).....	103
Figure 5.78 Comparison of the effective stress distributions obtained for different models for 25 mm punch travel (St12 steel, diagonal direction, blank holder 4 kN).....	103
Figure 5.79 Comparison of the thickness strain distributions obtained for different models for 25 mm punch travel (St12 steel, transverse direction, blank holder 4 kN).....	104
Figure 5.80 Comparison of the effective stress distributions obtained for different models for 25 mm punch travel (St12 steel, transverse direction, blank holder 4 kN).....	104
Figure 5.81 Comparison of the thickness strain distributions obtained for different models for 10 mm punch travel (St12 steel, diagonal direction, blank holder 5 kN).....	105
Figure 5.82 Comparison of the effective stress distributions obtained for different models for 10 mm punch travel (St12 steel, diagonal direction, blank holder 5 kN).....	105
Figure 5.83 Comparison of the thickness strain distributions obtained for different models for 10 mm punch travel (St12 steel, transverse direction, blank holder 5 kN).....	106

Figure 5.84 Comparison of the effective stress distributions obtained for different models for 10 mm punch travel (St12 steel, transverse direction, blank holder 5 kN).....	106
Figure 5.85 Comparison of the thickness strain distributions obtained for different models for 15 mm punch travel (St12 steel, diagonal direction, blank holder 5 kN).....	107
Figure 5.86 Comparison of the effective stress distributions obtained for different models for 15 mm punch travel (St12 steel, diagonal direction, blank holder 5 kN).....	107
Figure 5.87 Comparison of the thickness strain distributions obtained for different models for 15 mm punch travel (St12 steel, transverse direction, blank holder 5 kN).....	108
Figure 5.88 Comparison of the effective stress distributions obtained for different models for 15 mm punch travel (St12 steel, transverse direction, blank holder 5 kN).....	108
Figure 5.89 Comparison of the thickness strain distributions obtained for different models for 20 mm punch travel (St12 steel, diagonal direction, blank holder 5 kN).....	109
Figure 5.90 Comparison of the effective stress distributions obtained for different models for 20 mm punch travel (St12 steel, diagonal direction, blank holder 5 kN).....	109
Figure 5.91 Comparison of the thickness strain distributions obtained for different models for 20 mm punch travel (St12 steel, transverse direction, blank holder 5 kN).....	110
Figure 5.92 Comparison of the effective stress distributions obtained for different models for 20 mm punch travel (St12 steel, transverse direction, blank holder 5 kN).....	110
Figure 5.93 Comparison of the thickness strain distributions obtained for different models for 25 mm punch travel (St12 steel, diagonal direction, blank holder 5 kN).....	111

Figure 5.94 Comparison of the effective stress distributions obtained for different models for 25 mm punch travel (St12 steel, diagonal direction, blank holder 5 kN).....	111
Figure 5.95 Comparison of the thickness strain distributions obtained for different models for 25 mm punch travel (St12 steel, transverse direction, blank holder 5 kN).....	112
Figure 5.96 Comparison of the effective stress distributions obtained for different models for 25 mm punch travel (St12 steel, transverse direction, blank holder 5 kN).....	112
Figure 5.97 Edge contour comparison obtained for different models and experiments for 10 mm punch travel (blank holder 2 kN).....	113
Figure 5.98 Edge contour comparison obtained for different models and experiments for 15 mm punch travel (blank holder 2 kN).....	114
Figure 5.99 Edge contour comparison obtained for different models and experiments for 20 mm punch travel (blank holder 2 kN).....	114
Figure 5.100 Edge contour comparison obtained for different models and experiments for 25 mm punch travel (blank holder 2 kN).....	115
Figure 5.101 Edge contour comparison obtained for different models and experiments for 10 mm punch travel (blank holder 4 kN).....	115
Figure 5.102 Edge contour comparison obtained for different models and experiments for 15 mm punch travel (blank holder 4 kN).....	116
Figure 5.103 Edge contour comparison obtained for different models and experiments for 20 mm punch travel (blank holder 4 kN).....	116
Figure 5.104 Edge contour comparison obtained for different models and experiments for 25 mm punch travel (blank holder 4 kN).....	117
Figure 5.105 Edge contour comparison obtained for different models and experiments for 10 mm punch travel (blank holder 5 kN).....	117
Figure 5.106 Edge contour comparison obtained for different models and experiments for 15 mm punch travel (blank holder 5 kN).....	118
Figure 5.107 Edge contour comparison obtained for different models and experiments for 20 mm punch travel (blank holder 5 kN).....	118

Figure 5.108 Edge contour comparison obtained for different models and experiments for 25 mm punch travel (blank holder 5 kN).....	119
Figure 5.109 FEM Model of V-bending Operation.....	120
Figure 5.110 Springback amount comparison obtained for different models and experiments.....	120

## **CHAPTER 1**

### **INTRODUCTION**

Sheet metal is one of the most used form in metal working applications, which can be cut and bent into a variety of different shapes [1]. The parts produced by sheet forming generally are stiff and have a good strength to weight ratio. Sheet metal forming is used to manufacture a remarkable net shape in material shaping. Great deals of everyday objects are made of sheet metals [2]. Two major commercial sectors in which sheet forming used are: automotive industry and the home appliance industry. These industries require large quantities of low-carbon sheet steel [1].

The raw material for sheet metal manufacturing processes is the output of the rolling process. Then, the correct shaped and sized 'blank' is cut from the larger sheet. In sheet forming, a metal blank is shaped by tools or dies, primarily under the action of tensile stresses often without a significant change in its thickness or surface characteristics. In contrast to bulk forming, sheet forming often involves local deformations. The design and control of such processes depend on the characteristics of the workpiece material, the conditions at the tool workpiece interface, the mechanics of plastic deformation (metal flow), the equipment used, and the finished product requirements. Selection of tool geometry and material as well as processing conditions (workpiece and tooling temperatures, lubrication, etc.) are affected by the mentioned factors [1].

Sheet metal forming operations can be classified into two categories: separation (cutting) processes, and sheet forming (stamping) processes. In cutting process, sheet is worked above its ultimate strength, and separated partially or completely.

Separation caused by highly localized plastic deformation around the cutter edges where the excess shear stresses are higher than the material shear resistance [3]. Sheet forming is plastic deformation process originating from the dislocation motion in the material which undergoes a permanent shape change at stress above its elastic limit but below its ultimate strength. On the contrary of the cutting process, localized deformation should be avoided in forming processes [3]. In manufacturing, many sheet metal parts are undergo combinations of cutting and forming operations. Several sheet metal forming processes which are commonly used in the industry are: stretching, drawing, bending and flanging, punching and shearing, spinning, press forming and roll forming. In sheet metal forming, the deformation usually causes significant changes in the shape, but not necessarily the cross sectional area, of the sheet and in some cases, the magnitudes of permanent plastic and recoverable elastic deformations are comparable; therefore, elastic recovery or springback may be significant [4].

### 1.1 Sheet Forming Operations

Sheet forming operations are often called as press working processes, since the presses fulfill the forming [5]. Bending, deep drawing and stretch forming are widely used operations in sheet metal forming. Particularly, deep drawing and bending process are often used in automotive industry applications, such as forming of inner profiles and outer panels of automobiles as shown in Figure 1.1.

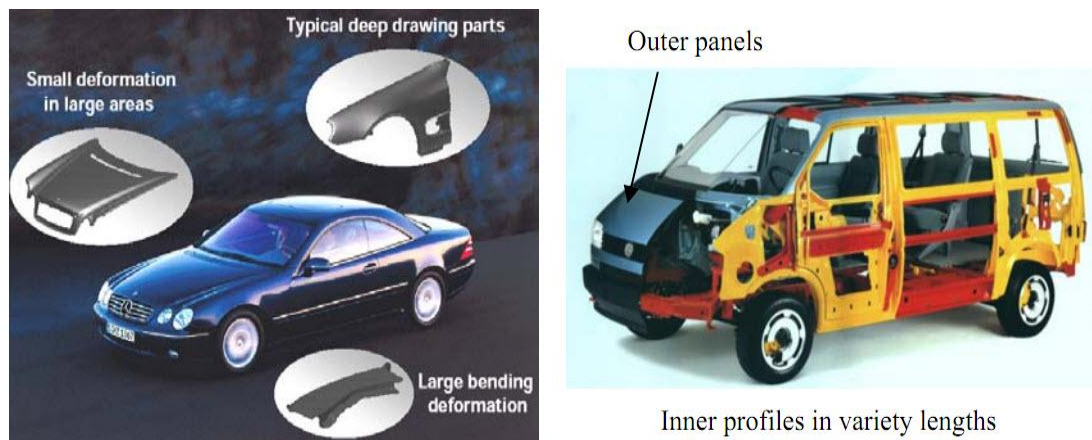


Figure 1.1: Sheet forming examples in automotive industry [6].

### 1.1.1 Bending

In bending, metal is shaped by stressing beyond its yield strength. Bending forces which result in plastic distortion of metal without failure occurs [3]. Bending operations: V-die bending and Single-die bending are shown in Figure 1.2 as an illustration.

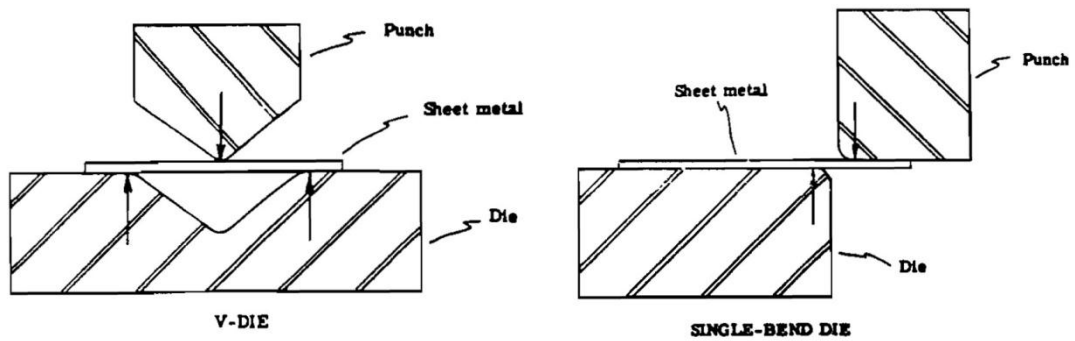


Figure 1.2: Bending forces during die bending [3].

During bending, the material is locally stressed at the bend radii along a line. The stress distribution on a sheet metal after bending is shown in Figure 1.3. The metal outside of the bend radius has been stretched, indicating that a tensile stress has been applied. The metal on the inside of the bend radius has been placed under a compressive stress [7].

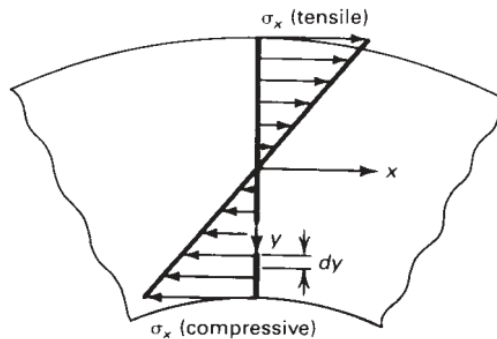


Figure 1.3: Stress distributions after bending [7].

### 1.1.2 Stretch Forming

Stretch forming is a method that combines controlled stretching and bending of sheet metal blanks and roll formed sections to produce accurately contoured parts without wrinkles. Stretch forming operation is shown in Figure 1.4. Benefit of stretch forming is, application of stretching prior to or during bending operations, prevents wrinkling and reduces the effect of springback. As an advantage of stretch forming tensile strength and hardness are increased [8].

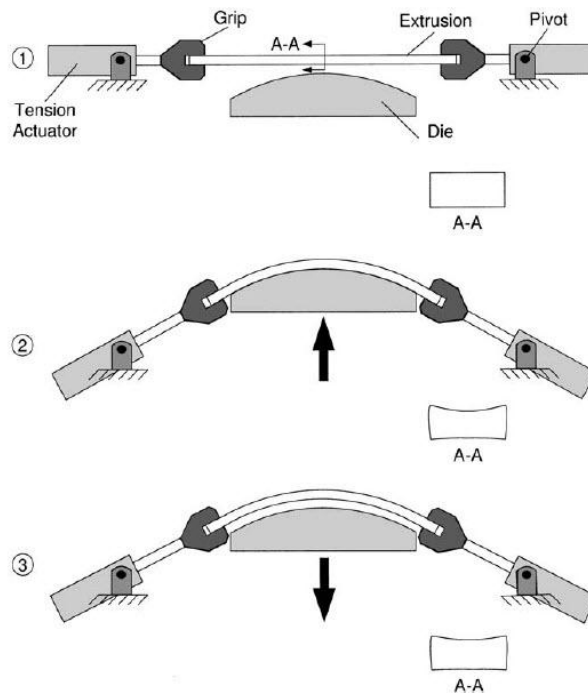


Figure 1.4: Stretch forming operation [9].

Stretch forming is used for forming body panels, such as doors, roofs, or fenders for trucks, busses, and special vehicles, and in the aircraft industry [10].

### 1.1.3 Deep Drawing

Deep drawing is a cold forming process by which a flat sheet of metal is formed into specific shape of geometry. The undeformed sheet, called the blank, which is placed

over the die and pressed into the die cavity using a punch [11]. Principal elements of deep drawing operation are shown in Figure 1.5.

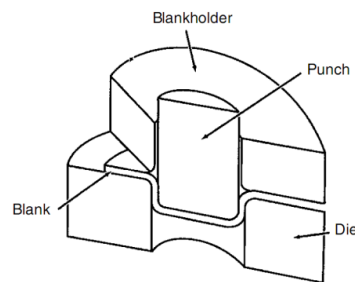


Figure 1.5: Principle elements of deep drawing [1].

Deep drawing process involves many types of forces and deformation modes, such as tension in the wall and the bottom, compression and friction in the flange, bending at the die radius, and straightening in the die wall [1]. These regions are shown in Figure 1.6.

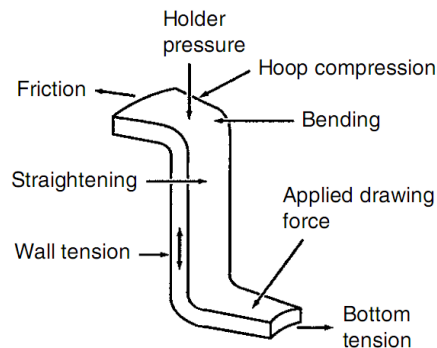


Figure 1.6: Stress zones during deep drawing [1].

Products that are produced by deep drawing can be seen within many fields, from automobile bodies to household applications. Deep drawing is the most suitable sheet metal forming technique that is used for the mass production of simple shaped parts [11]. Some of these products are shown in Figure 1.7.



Figure 1.7: Some examples of conventional deep drawing products [12].

During deep drawing operations some major failure modes occur, such as wrinkling, earing and tearing which are shown in Figure 1.8.

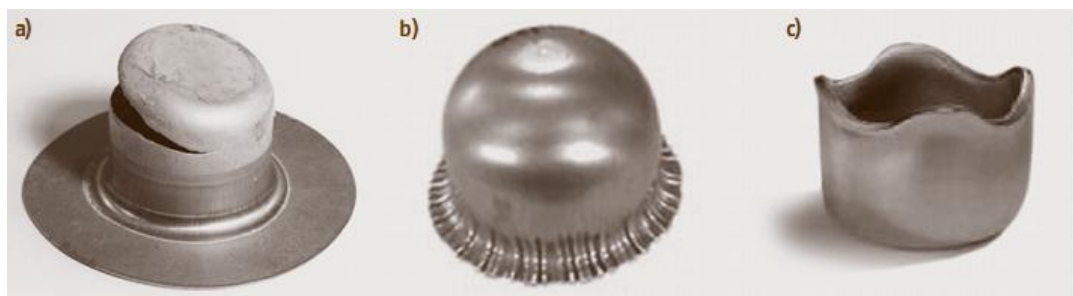


Figure 1.8: Typical failure modes in deep drawing: a) tearing, b) wrinkling, c) earing [13].

These phenomenon limit the type of parts and geometries that can be formed using conventional forming. During sheet forming, wrinkles are caused due to internal compressive stresses. If the clearance between the die and the punch is high, wrinkling may occur in the flange or in the side wall of the cup. In order to control the metal flow during deformation, restraining forces are applied to the sheet metal which helps to prevent wrinkling. If the metal is thick this restraining would be

enough to form the part without defects, but in most cases a blank holder force is required to obtain extra restraining forces [11].

In sheet forming, the final shape of a product is strongly linked to the plastic material flow. The state of deformation in a plastically deformed metal is fully described by the displacements, velocities, strains and strain-rates. Metal flow is influenced mainly by; tool geometry, friction conditions, characteristic of the material used and thermal conditions existing in the deformation zone etc. [14]. Major factors that influence metal flow during drawing operations have been summarized by Siegert [10].

*a) Shape and size of the blank;*

Using larger blanks increases forming and friction forces. Therefore, higher punch loads are needed for drawing and stretch forming for larger blanks [10].

*b) Draw beads;*

Draw beads are used to prevent wrinkles and control the metal flow in drawing operation. Increasing number of draw beads, result in the increase draw forces where local friction and bending that requires more energy and force. Moreover, using draw beads increases the cost of tools, product development, and tool maintenance [1].

*c) Lubrication and Friction;*

The amount and selective distribution of the lubricant over the blank surface influences the value of the local friction between the sheet metal and the blank holder as well as friction between the sheet metal and the dies. Consequently, material flow is locally influenced [10].

*d) Blank Holder Force*

Blank holder force should be high enough to prevent wrinkling. In case the blank holder force is too large, fracture may occur in the unsupported region between the die and punch corner profiles. So that blank holder force is an important parameter during drawing operations, and mostly its optimal value is found by trial and error

method. Generally, blank holder force depends on draw reduction, sheet thickness, material properties, type of lubrication used etc. For thickness consideration, the thinner the work metal, the more blank holder force that is required [1].

*e) Punch Velocity*

The draw velocity influences mainly the friction conditions. As the draw velocity increased, the friction in the flange is reduced. As a result, drawability improves with the increase of the draw punch speed [10].

*f) Springback*

Obtaining an accurate and repeatable bend profile is difficult due to elastic springback. When a workpiece is removed from tools, the residual stresses after forming are released, and cause an additional unwanted deformation which is called springback as shown in Figure 1.9. Springback phenomenon, connection with sheet metal forming is mainly a stress driven problem. The magnitude of the springback is approximately proportional to the ratio between the residual stress and Young's modulus [15].

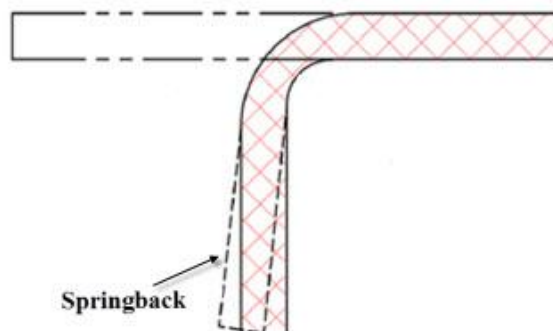


Figure 1.9: Springback phenomenon [16].

The springback phenomenon is particularly troublesome for high strength steels (high residual stress) and aluminum (low Young's modulus). Unfortunately, these materials have found an increasing use in the automotive industry recently, in order to improve crash performance and reduce weight [15]. Therefore, springback has

crucial importance in automobile industry and it must be accurately predicted. Many factors affect springback, such as material variation in mechanical properties, sheet thickness, bend radius, constitutive relation, bending arc, tooling geometry, friction etc. [17].

## **1.2 Constitutive Modeling**

In this study the evolution of the yield surface, hardening laws and the constitutive models will also be investigated. The proper measurements and descriptions of the initial yield surface and its evolution are essential for the constitutive law in plasticity. Since the yield surface and its evolution are difficult to measure, the isotropic and kinematic hardening of the initial yield surface is commonly assumed in the theoretical plasticity. As, the strain-path effect on the constitutive behavior can be better represented by combining the isotropic and kinematic hardening behaviors; the finite element method based on the combination type constitutive law is also used [18].

Numerical analysis is critically important to understand the complex deformation mechanics that occur during sheet forming processes. Nowadays, finite element analysis and simulations are used in automotive design and formability processes to predict deformation behavior accurately during forming operations. Confidence in the numerical analysis of formability depends on the accuracy of the constitutive model describing the behavior of the material [14]. This is especially important when the material exhibits anisotropic characteristics, as do most cold rolled sheet metals. Previous research demonstrate the importance of using appropriate material models with respect to wrinkling and ironing during sheet forming operation [19].

Commercial finite element codes offer a library of constitutive models applicable to a variety of applications. It is also necessary to understand which constitutive models are capable of handling complex forming simulations that incorporate the different forming operations. The process becomes increasingly complicated when materials exhibit anisotropic behavior, because material hardening behavior and material response to loading conditions change during deformation [14].

In this study, material characterization of the anisotropy coefficients of two accurate constitutive models: Barlat and Hill models are carried out. In addition the modified power law isotropic plasticity, piecewise linear isotropic plasticity and isotropic kinematic and combine hardening constitutive models are evaluated [14].

### **1.3 Scope of Thesis**

This research primarily focuses on the sheet metal bending and deep drawing processes. Especially, cylindrical deep drawing, square cup deep drawing and V-bending operations will be investigated for the effects of different constitutive model and hardening laws in sheet metal forming. In order to investigate these characteristics, three different sheet metals are used; Erdemir-6112 (St12) steel, stainless steel 409 Ni and Al-5182 aluminum. Mentioned constitutive models, used as a material model in a commercial explicit/implicit finite element code. Simulations are run for the square deep drawing, cylindrical deep drawing and V-bending operations. Moreover, effective stress and thickness strain distributions, edge contours and springback amounts are compared against experimental results.

This dissertation consists of six chapters. Chapter I is the introduction. The development of sheet forming mechanics is reviewed as individual topics: bending, stretching and deep drawing. Chapter II provides a literature review of sheet forming operations especially effect of different constitutive models and yield locus for V-bending and square cup drawing, due to springback, wrinkling, earing and tearing phenomena has been discussed. In Chapter III, some theoretical information about the finite element method is given. In Chapter IV, constitutive models will be reviewed. In Chapter V, comparison of simulations with experiments will be given. Finally, in Chapter VI conclusion and discussion will be presented.

## CHAPTER 2

### LITERATURE SURVEY

The purpose of this thesis is to investigate the effect of different constitutive models and different hardening models in sheet metal forming operations, thus the survey of the past research has been concentrated on two main sheet metal forming operations; square cup deep drawing and V-bending. Also, the effect of different constitutive models and different hardening laws in sheet metal forming and undesired situation in forming operations, such as wrinkling, springback, earing, tearing and bending unbending have been mentioned.

In this section some of the past studies related with the above mentioned processes, which have been considered to be important, will be presented in a chronological order. Some of the first basic researches will be given at first, which gain acceleration with the expanding technology and changing forming operations.

Cao and Boyce [20] studied wrinkling of rectangular plate subjected to edge compression and a lateral constraint (i.e., subjected to a lateral binder force). They used the energy method in conjunction with finite element code ABAQUS, with using 4-noded reduced integration shell elements S4RF. Cao and Wang [21] also used the energy method, but in conjunction with the analytical method of plastic bending theory. The purpose was to obtain the expressions of the critical compressive stress and the wavelength as functions of the binder pressure in a rectangular plate subjected to edge compression and a lateral binder force. They called these conditions as Cao and Boyce (C-B) wrinkling criterion. Hill's 1948 [22]

quadratic anisotropic yield function was used to model the anisotropy of the material. They also performed a parametric study with respect to the transverse tension and the strain-hardening exponent. They state that these results can be used to predict wrinkling in deep drawing process.

Li et al. [23] studied the springback of V free bending by using self-developed 2D elastoplastic finite element code. Regarding the effect of material's hardening mode on springback accuracy, two hardening models were adopted in this study, a linear hardening model and an elastoplastic power exponential hardening model. They applied the formulation for three different materials and the variation of material's Young's modulus with plastic deformation was also considered. As a result of the study, the springback calculated with the elastoplastic power exponential hardening model well agrees with experimental results than that calculated with the linear hardening model. It was also shown that, Young's modulus has a great effect on springback simulation accuracy; variation of Young's modulus with plastic deformation can improve the accuracy of the springback simulations.

Papeleux and Ponthot [24] studied the prediction of springback in Numisheet'1993 benchmark U-bending; they carried out experiments and compared the theoretical and experimental results. The influence on springback of several parameters such as blank holder force, friction, spatial integration, time integration scheme and constitutive laws describing the material used were studied in details. Simulations were made by the commercial finite element code OPTRIS with 2D linear shell elements. They applied Chung-Hulbert dynamic implicit time integration scheme [25] in the analyses. Three different materials were used in the experiments such as mild steel, high strength steel and aluminum. As a result of this study, numerical results fall in the range of experimental data.

Kim et al. [26] carried out finite element analysis with continuum-based resultant (CBR) shell elements, to study wrinkling in a circular cup. Both Hill's 1948 [22] anisotropic yield function and Barlat's 1991 [27] anisotropic yield function based on one linear transformation were used to model the anisotropy of the sheet. They obtained the critical (average) circumferential stress, wrinkling wavelength and critical punch stroke as functions of the blank holder force and the results were

compared with experimental results. It was shown that the critical punch stroke was over estimated by the finite element bifurcation analysis while the wrinkling wavelength was under-predicted. They also studied the effect of material properties (like the anisotropy coefficient and the strain-hardening coefficient) and the friction coefficient on the wrinkling pattern. They found that wrinkling occurs more easily for sheet materials having a lower normal anisotropy.

Choi [28] developed a new hardening model Rotational-Isotropic-Kinematic (RIK) model, which account for the rotation as well as the expansion (isotropic hardening) and translation (kinematic hardening) of the yield loci in terms of plastic spin theory and anisotropic hardening model. The capability of the RIK model was demonstrated by simulation of cylindrical and square cup drawings and compared with the experimental data of Numisheet'1993 benchmark. Choi used deep drawing quality steel and high strength steel in the experiments. Isotropic hardening and nonlinear kinematic hardening were used to compare results with RIK and averaged experimental results. The RIK model shows more accurate results in the prediction of earing as well as stress and strain distribution. It was shown that the proposed RIK model improve the representation of anisotropic behavior of sheet metals in forming simulation and springback prediction.

Chen et al. [29] studied the deep drawing of square cups with magnesium alloy AZ31 sheets by both the experimental approach and the finite element analysis. Effects of process parameters such as punch and die corner radii, and forming temperature were investigated on the formability of square cup drawing. The maximum depth of the drawn square cup without fracture was used as the index of formability. In finite element analysis, the Forming Limit Diagram was adopted as the fracture criterion to determine the maximum drawn depth of the square cup. Simulation results and the experimental results indicate an optimum forming temperature of 200 °C for square cup drawing. They also obtained that, a smaller punch radius reduces the formability of square cup drawing. The agreement between the finite element analyses and experimental results were obtained for an optimum die corner and punch radius.

Chan et al. [11] studied the springback in the V-die bending forming process, while one end was clamped and the other free. The purpose was to obtain the effect of different die punch parameters, such as punch radius, punch angle and die-lip radius on springback. In the simulations commercial finite element code ABAQUS was used with plane strain shell elements CPE4. As a result of the analyses, springback decreases as punch angle and punch radius increases and springback increases as die-lip radius increases.

Chung et al. [30] implemented a user defined constitutive model for isotropic-kinematic hardening behavior based on the non-quadratic yield function Yld2000-2d [31] into the commercial code ABAQUS. Incremental deformation theory was applied to the elastoplastic formulation based on materially embedded coordinate system. Combined isotropic-kinematic hardening rules based on the Chaboche model was applied for the non-quadratic anisotropic yield potential in which kinematic hardening parameters were dependent on the effective strain. In this study springback prediction capability of the combined isotropic-kinematic hardening constitutive law developed.

Chung et al. [32] later applied experimental procedure to obtain the material parameters for the modified Chaboche type combine isotropic-kinematic hardening law and non-quadratic anisotropic yield function, Yld2000-2d [30]. The anisotropy and the hardening behavior were characterized for three automotive sheets: AA5457-O, AA6111-T4 and DP-Steel. Anisotropic properties were obtained considering the directional difference in the yield stress and the plastic strain ratio measured from the uniaxial tension test as well as hydraulic bulge test. From the tension compression curves, parameters of the isotropic and kinematic hardening behavior were obtained.

Chung et al. [33] applied the proposed constitutive law in [30] for springback simulating of S-rail drawing and unconstrained bending, Springback results were compared with experimental results for three cases: the unconstrained cylindrical bending, the 2D draw bending and the modified industrial part S-rail drawing. The material parameters obtained in [32] for AA6111-T4, AA5754-O and DP-Steel were used for simulations. In addition to the combined hardening law, pure kinematic hardening and isotropic hardening were also considered to understand the hardening

law effect on springback. Using the calculated moment curvature curves, the effects of several parameters such as thickness, elastic properties and tension force on springback were compared for the experiments and simulations. For all three cases, simulations were well agreed with experiments. Springback of bending and twist was largest for AA6111-T4 and least for AA5754-O, while DP-Steel was similar with AA6111-T4 for bending, but with AA5754-O for twisting. In the parametric study performed for the 2D draw bending the large blank holder force suppressed springback and the pure kinematic hardening law was not suitable to simulate the side wall curl, which were also well confirmed by the simple analysis. The springback of bending for S-rail drawing was insensitive to the process parameters. It was obtained that, for all three verification cases, the material direction effect was negligible because of the weak anisotropy of the three materials.

Yoon and Hong [34] implemented Yld2000-2d [31] and Yld2004-18p [35] into the commercial finite element code Ls-Dyna as a user defined constitutive model. The purpose of this study was to validate the implemented yield functions regarding earing prediction and automotive stamping analysis. The cup drawing test simulation with circular punch and blank was used for prediction of earing profile. This test was simulated for an imaginary alloy sheet called FM8 based on Yld2004-18p yield function. As a practical application, they analyzed Numisheet'2005 benchmark with Al5182-O sheet material, which was characterized by both Yld200-2d and Yld2004-18p for the comparison purpose. The results obtained from the two yield functions coincide exactly. It was also shown that for springback results, simulations have a good agreement with experimental data. Furthermore, Yld200-2d presented an excellent computational efficiency.

Kim et al. [36] studied the effect of hardening laws and yield function types in order to simulate the springback of DP-Steel sheets. Simulations performed for 2D draw bending and S-rail drawing tests by using commercial finite element code ABAQUS. Performance of the combined isotropic-kinematic hardening based on the modified Chaboche model was compared with those of the pure isotropic hardening and kinematic hardening laws along with von Mises and non-quadratic anisotropic Yld200-2d [31] yield functions. For 2D draw bending test, numerical results were

compared with experimental results for verification purposes, but for S-rail drawing test experimental results were not available for the particular DP-Steel so they couldn't be verified. They applied the incremental deformation theory to the elastoplastic formulation for large deformations. According to this research, for the 2D draw bending test, the springback prediction considering the combined isotropic-kinematic hardening law with Yld200-2d was most accurate. When the kinematic hardening was used, the springback amount was considerably underestimated, suggesting that the kinematic hardening was not adequate to predict the springback. Also, the yield function difference did not affect results that much, either Yld200-2d or von Mises yield functions were used.

Oliveira et al. [37] studied on the Numisheet'2005 benchmark U-shape channel draw concerning the influence of work hardening modeling in springback prediction. Several work hardening models were used, such as Swift law (Power law) or a Voce type saturation law to describe classical isotropic work-hardening, Lemaitre and Chaboche [38] type law to model the nonlinear kinematic hardening, which can be combined with previous two and Teodosiu's micro structural work-hardening model. They carried out the simulations with finite element code DD31MP by using two steel materials: DC06 and DP600. Several hardening models tested and it was shown that the difference in springback predictions were not significantly high. Small differences were caused by the through-thickness stress gradients.

Eggertsen and Mattiasson [15] implemented user defined constitutive models for five different hardening laws: isotropic hardening, mixed isotropic-kinematic hardening, Armstrong-Fredrick, Geng-Wagoner [39] and Yoshida-Uemori [40] models into commercial finite element code Ls-Dyna. These models have been applied to four different steels; two DP-600 steels from two different suppliers and with different thicknesses, a mild DX56D steel and 220IF steel. In addition, three different yield conditions have been evaluated: Hill48 [22], Barlat-Lian [41] and Banabic/Aretz [42]. The purpose was to study the effect of different hardening models and different yield locus on springback. In the formulations the incremental update of stress is based on an elastic predictor plastic corrector procedure was used. The springback of a simple Numisheet'1993 benchmark, U-bending has been calculated for one of the

materials. As a result, it was shown that hardening law has a significant influence on the results, while the choice of yield condition had only a minor influence. Regarding the effect of hardening laws, they showed that springback deflections substantially under predicted when compared with the experiments.

Bayraktar et al. [43] made parametric studies that predict accurately the final geometry of the sheet blank and the distributions of stresses and strains. They also tried to control various forming defects, such as thinning as well as parameters affecting final form of the sheet after forming process with their study. Deep drawing of square cup was simulated by using commercial finite element code ABAQUS to validate with experiments. Deep drawing processes were achieved by using aluminum, mild steel and HFS steel sheets. Parameters of deep drawing process were; aspect ratio, blank initial thickness, die radii, coefficient of friction, etc. Blank was modeled of linear finite strain shell elements SC8R with 8-nodes. The blank displacements predicted by the numerical models were generally in fair agreement with experimental results. The influence of the numerical parameters was relatively small. For coefficient of friction parameter, prediction of earing profile was in agreement with experimental results for both mild steel and HFS sheet materials. The weak anisotropy of the aluminum was assumed to be the reason of poor accuracy results obtained during the research.

Wang et al. [44] developed an equivalent plastic strain (EP) dependent anisotropic constitutive model for Al5754-O aluminum, which considers the changes of anisotropy. In the developed model, the anisotropy coefficient for Barlat's Yld2000-2d [31] anisotropic yield function was used. EP-dependent and EP-independent Yld200-2d yield functions were implemented into commercial program ABAQUS as a user defined constitutive model. In order to evaluate the accuracy of the developed constitutive model, biaxial tensile test were carried out under proportional loading with different yield functions (von Mises, Hill48 [22] and Yld200-2D) [31]. They carried out experiments and the validity of the developed model was confirmed by comparing the simulated and experimental results which were in good agreement particularly for the EP-dependent yield function than the other yield functions.

Tang et al. [45] implemented user defined mixed hardening model based on nonlinear kinematic hardening models, Lemaitre and Chaboche [40], to the commercial finite element code ABAQUS. In the comparison with experimental results, effectiveness of mixed hardening model has verified for the bending and reverse bending case studies. They applied backward Euler return mapping algorithm to calculate stress and strain increments of AL6022-T4 material. Plane stress conditions were considered due to, with of the blank, 35 mm is much greater than its thickness, 0.81 mm in the process. Analyses were made with shell element S4R, which had seven gauss integral points along thickness direction to simulate sheet forming and springback process. Influence of different yield criteria, von Mises, Hill 1948 [22] and Barlat'89 [41] on springback was also illustrated with mixed hardening model that is implemented by using shell elements. As a result of the comparisons with linear kinematic hardening model and isotropic hardening model with Numisheet'1993 benchmark show that, the mixed hardening model coupled with Barlat'89 yield criterion can well reflect stress and strain distributions and give a more favorable springback angle prediction.

Ravindra and Dixit [46] used the Hill's bifurcation criterion to predict onset of flange wrinkling in circular and square cup drawing. Finite element formulation based on updated Lagrangian approach was employed for the analysis. The anisotropic plastic behavior of the sheet was modeled by recently proposed yield function Barlat's Yld2004-18p [35]. They applied Modified Newton-Raphson iterative technique to solve the nonlinear incremental equations and three dimensional, 8-noded brick elements were used to incorporate both the shear and bending effects. Developed finite element code was first used to validate the simulation of square and circular cup drawing of AA6111-T4 and AA2090-T3 aluminum alloys. The simulation results were compared with previous study of Yoon et al. [47] for square and circular cup drawings respectively, and reasonably good agreements were obtained. A parametric study of the maximum cup height due to wrinkling was also carried out with respect to various parameters, such as; effects of blank holder pressure, sheet thickness, die profile radius, punch profile radius, sheet anisotropy and other material properties (Initial yield stress in the rolling direction, hardening coefficient,  $K$  and the hardening exponent,  $n$ ). The specific conclusions of this study were as follows;

(i) increase in the blank holder pressure or the sheet thickness delays the onset of wrinkling, (ii) maximum cup height at the onset of wrinkling increases with an increase in the die profile radius or punch profile radius, (iii) sheet anisotropy generally delays the onset of wrinkling, (iv) material properties affect the maximum cup height at the onset of wrinkling differently according to drawing process used.

Aboozar et al. [48] developed constitutive model based on non-associated flow rule and mixed isotropic-kinematic hardening. These constitutive models were also implemented into commercial finite element code ABAQUS. They applied Return mapping algorithm to integrate the stress over each time increment. Both yield and plastic potential functions were defined in the form of Hill48 [22] quadratic anisotropic function. Isotropic hardening followed a nonlinear behavior, either a power law or an exponential law. The evolution of the back stress tensor was modeled based on the nonlinear kinematic hardening theory Armstrong-Frederick formulations. Two different sheet metal forming processes were simulated using the implemented user defined constitutive model to evaluate the different aspects of this non-associated model. A cylindrical cup drawing was simulated with AA2090-T3 material to predict the earing profile and the effects of sheet metal anisotropy. Also, springback prediction of a channel draw process (with drawbead) was simulated with two sheet materials; DP600 and AA6022-T43 to assess the effect of the hardening model. A shell element formulation with reduced integration mode was used to model the blank. Predicted equibiaxial, shear stress strain curves and r-values at different angles were compared with experimental values. It was also shown that, earing and springback prediction were improved by using this non-associated mixed hardening constitutive model.

Vladimirov et al. [49] derived and implemented constitutive model for plastic anisotropy and nonlinear kinematic and isotropic hardening into the commercial finite element code ABAQUS. In addition to Hill type plastic anisotropy [22], the model incorporates nonlinear Armstrong-Frederick kinematic hardening and nonlinear Voce type isotropic hardening. They applied exponential map algorithm with C3D8R reduced integration solid elements in the simulations. Applicability of the model was demonstrated by means of simulations of several deep drawing

processes such as drawing of thin circular plate, cylindrical cup drawing, square cup drawing and S-rail forming. They carried out experiments and compared the theoretical and experimental results of DP600 steel used for drawing of thin circular plate and aluminum sheets were used for cylindrical cup drawing, square cup drawing and S-rail forming as a blank material. Formation of earing was investigated in the simulations and comparisons with test data for aluminum alloy sheets display a good agreement with experimental results.

## CHAPTER 3

### FINITE ELEMENT METHOD

#### 3.1 Introduction to Finite Element Method

The finite element method is a numerical procedure for analyzing structures and continua. Engineering problems are generally too complicated to be solved satisfactorily by classical analytical methods. Therefore, in the analysis of engineering problems numerical methods; finite difference method (FDM), the finite element method (FEM) and their variants are mostly used [50].

FEM is on the basis of the idea of every system is physically consist of different parts. Therefore, the solution of this system can be used for the solution of the parts. The finite element method is considered as the method of stress analysis. FEM produces many simultaneous algebraic equations, which are generated and solved on a digital computer. The result that has been obtained from the FEM are not exact, however errors can be decreased by processing more equations and could be used for the engineering problems [51].

FEM is efficient numerical method ever devised for the analysis of engineering problems. It is capable of handling geometrically complicated domains, a variety of boundary conditions, nonlinearities, and coupled phenomena that are common in practical problems. Today, finite element method is also used to analyze problems of heat transfer, fluid flow, lubrication, and many other areas [52].

In finite element analysis of physical problems, particular steps in formulations are common for all analyses types, such as structural, heat transfer, fluid flow or other

analyses. These steps are embodied in commercial finite element software packages which are called as preprocessing, processing and post-processing steps.

The preprocessing step is quite generally described as, defining the model and includes defining element types, material properties, element connectivity, physical constraints and loadings [53].

During processing phase, finite element software assembles the governing algebraic equations in matrix form and computes the unknown values of the primary field variables. The computed values are then used by back substitution to compute additional derived variables, such as reaction forces, element stresses, and heat flow [53].

Analysis and evaluation of the solution results is referred to as post-processing. Post processor software is used for sorting, printing and plotting selected results from a finite element solution [53].

Depending on the problem type different solution approaches are suitable. If the problem can be treated as linear elastic and the loading is static, these classes of problems are solved with just one loading step. Another problem class is the quasi-static problems which can be characterized by a so slow loading rate, therefore, the inertial effects have no influence on the results. These kinds of analyses are path dependent. This approach has previously been the traditional way to treat sheet forming [54].

The last group is the quasi-dynamic problems. These classes of problems always include a time dependency and often show a path dependency. Sheet metal forming processes can be characterized as either quasi-static or quasi-dynamic, but it may be found reasonable to treat a quasi-static process as a quasi-dynamic problem. In fact this is what is done when using explicit time integration scheme [54].

FEM analyses are divided into two categories as linear and nonlinear analysis. Linear analyses are based on linear stress-strain relationship (Hooke's law) and they are usually allowed when stress at any point in the component is below the elastic limit or yield stress. In this analysis, in order to obtain stresses for any combination of

loads acting simultaneously, linear superposition of results that are obtained for individual loads on a component is used [55].

Using nonlinear analysis is a necessity for; designing high performance and efficient components of certain industries (e.g., aerospace, defense and nuclear), assessing functionality (e.g., residual strength and stiffness of structural elements) of existing systems that exhibit some types of damage and failure, establishing causes of system failure, simulating true material behavior of processes, and research to gain a realistic understanding of physical phenomena [56]. Nonlinear analysis has following features [54]:

- The principle of superposition is not hold.
- Analysis can be carried out for one "load" case at a time.
- The response of the system is influenced by the history of "loading".
- The initial state of the system (e.g. pre-stress) may be considered important.

Nonlinearity in structural mechanisms is caused by two common sources. These are geometric and material nonlinearities. The geometric nonlinearity arises purely from geometric consideration (e.g. nonlinear strain-displacement relations), and the material nonlinearity is caused by the nonlinear constitutive behavior of the material of the system. A third type of nonlinearity may arise due to changing initial conditions or boundary conditions [56].

### **3.1.1 Geometrical Nonlinearity**

In many problems strain-displacement relations are not linear. Such problems need consideration of actual strain displacement relations rather than the linear strain displacement which require a nonlinear theory. Large deflection problems like the analysis of tension structures, post buckling studies of beams, plates and shells also fall under this category [57].

### **3.1.2 Material Nonlinearity**

The stress-strain relation for the material (e.g. the constitutive law) may not be linear and can be time-dependent too. If actual behavior of the structure is studied beyond

the yielding, the stress strain relation is nonlinear. Apart from these basic nonlinear relations, there are time dependent complex constitutive relations like plasticity and creep which make the problem nonlinear [57]. Many materials which show elastoplastic responses depict nonlinear behavior, such as viscoelastic polymers or steels, concrete and soil [58].

### **3.1.3 Nonlinear Boundary Conditions**

Another source for nonlinearities is related to special boundary constraints. Nonlinearities that are caused by boundaries are related to contact between two bodies or deformation dependent loading. Boundary constraints that are changed with the deformation state of system are the primary reason of such nonlinearities. These can be seen during a deformation process, when body comes into contact with another body [58].

### **3.2 Large Displacement and Large Strain Behavior**

When large strains are considered, neglecting the volume and shape changes of a structure is inadmissible. Therefore, in the integration of virtual work and virtual force equations, principle of virtual displacements has to be taken over the control volume.

Since, the current volume is unknown which depends on displacements that are also unknown too, cause problems which must be calculated at first. In order to solve this problem, it is necessary to introduce a transformation so that integrals are taken over known volume.

Eularian and Lagrangian Formulations are the two possible ways of solutions that are performed [59]. The Lagrangian approach can be classified in two categories, the Total Lagrangian (T.L.) method and the Updated Lagrangian (U.L.) method [59].

Both the T.L. and U.L formulations include all kinematic nonlinear effects due to large displacements, large rotations and large strains. In the T.L. formulation all static and kinematic variables are referred to the initial configuration at time zero, whereas in U.L. formulation, it is also based on the same procedures that are used in

the T.L. formulation, however in the solution all static and kinematic variables are referred to the configuration at time 't'. When the U.L and T.L. formulations are compared it is seen that, only theoretical difference is the choice of different reference configuration for the kinematic and static variable [60].

In this study, Lagrangian formulation has been applied where the finite element mesh is attached to the material and moves through space along with material.

### **3.3 Explicit and Implicit Time Integration**

For solving the ordinary differential equations, explicit and implicit time integration schemes are the two different types which are commonly used. The implicit methods lead to a system of nonlinear equations which have to be solved. The implicit integration scheme can be made unconditionally stable, and the time step is only chosen on the basis of the desired accuracy [55]. When implicit solution scheme is used for highly nonlinear problems, convergence problems occur. By using explicit time integration, geometrical, material and contact nonlinearities are treated without causing any problem and combined with the ability to handle the process instabilities. Explicit codes are suitable and often experienced in sheet forming operations due to their fast development [54].

Explicit finite element methods have been extensively used for problems involving high velocity and short duration of loading. Some aspects make the explicit formulation superior in comparison with an implicit formulation, especially for problems where the stiffness variations are dominated by contact condition [54].

Some of the advantages of the explicit formulation are listed below:

- Few computations are required per time step,
- Complex nonlinearities are easily handled, since the algorithm is simple in logic and structure,
- It requires little data storage compared to direct elimination methods (Newton-Raphson),
- Since, less coding are required, it is ideal for testing new ideas,
- It is reliable in accuracy and completion of computation.

The explicit method has an obvious disadvantage; it is conditionally stable which requires very small time steps. Therefore, accuracy problems due to round-off errors are occurred [54]. In this study explicit integration is applied for the general solution and implicit integration for springback.

### 3.4 Finite Element Formulation

In this thesis, finite element analyses of the square and cylindrical cup drawings and V-bending operations had been carried out by using a commercial finite element code, Ls-Dyna (version 971). Ls-Dyna is a general purpose finite element program which is used to analyze the nonlinear dynamic response of three dimensional structures. It is one of the explicit/implicit solvers commonly used for the simulation of metal forming operations, crash and pedestrian safety in automotive, general static and dynamic analyses, airbag folding and roller hemming etc.

In Ls-Dyna, solution of the momentum equation is used in the dynamic explicit simulations [61].

$$\sigma_{ij,j} + \rho f_i = \rho \ddot{x}_i \quad (3.1)$$

where  $\sigma_{ij}$  is stress tensor,  $\rho$  is density,  $f_i$  is body force and  $\ddot{x}_i$  is acceleration. If Equation 3.1 is multiplied by the virtual displacement  $\delta x_i$  and integrated over control volume, momentum equation can be expressed in variational form as;

$$\int_V \delta x_i (\sigma_{ij,j} + \rho f_i - \rho \ddot{x}_i) dV = 0 \quad (3.2)$$

With the help of principal of virtual work, equilibrium equation can be defined as,

$$\int_V \sigma_{ij} \delta x_{i,j} dV + \int_V \rho \ddot{x}_i \delta x_i dV - \int_V \rho f_i \delta x_i dV - \int_S t_i \delta x_i dS = 0 \quad (3.3)$$

Above work terms are originated from the inertia force, internal forces, body force and work occur by stress boundary conditions. Moreover, work done by contact conditions and friction can also be added to the Equation 3.3.

If the equilibrium equation is written in matrix form for an element;

$$\int_V \rho N^t N a dV + \int_V B^t \sigma dV - \int_V \rho N^t b dV - \int_S N^t t dS = 0 \quad (3.4)$$

where,  $N$  is interpolation matrix,  $\sigma$  is the stress vector,

$$\sigma^t = (\sigma_{xx}, \sigma_{yy}, \sigma_{zz}, \sigma_{xy}, \sigma_{yz}, \sigma_{zx})$$

$b$  is the body force load vector and  $t$  are applied traction loads.

$$b = \begin{bmatrix} f_x \\ f_y \\ f_z \end{bmatrix} \quad t = \begin{bmatrix} t_x \\ t_y \\ t_z \end{bmatrix}$$

$B$  is strain-displacement matrix,  $a$  is nodal acceleration vector in Equation 3.4. Acceleration is determined by the following equation,

$$\begin{bmatrix} \ddot{x}_1 \\ \ddot{x}_2 \\ \ddot{x}_3 \end{bmatrix} = N \begin{bmatrix} a_{x1} \\ a_{y1} \\ \cdot \\ \cdot \\ a_{yk} \\ a_{zk} \end{bmatrix} = N a \quad (3.5)$$

By integrating the acceleration matrix, velocities and displacements can also be calculated. From the displacements by using the appropriate equations the element stresses are determined.

## CHAPTER 4

### CONSTITUTIVE MODELS

#### 4.1 Introduction to Constitutive Models

In the matter of accuracy of sheet metal forming simulation, choosing the type of material constitutive model and its implementation to the finite element program are considered as important as forming conditions (friction, tool and binder geometry). In order to get proper strain and stress distribution and accurate springback prediction in a formed part, it has been observed that material constitutive models play a key role in describing the deformation behavior of the sheet metal [62].

In sheet metal forming simulations, crystal plasticity and phenomenological models are two different approaches that have been used for plastic deformation case. Sheet sample is treated as single crystals with preferred distribution in the polycrystalline plasticity model (i.e., crystallographic texture). Plastic deformation has been described by the discrete dislocation slips that take place on specific lattice planes along particular crystallography directions. This method can be depicted powerful method, since texture evolution during plastic deformation can be taken in to account. However, simulating any sheet metal forming processes with this method requires a huge amount of computation time [63].

In this study, phenomenological model as part of continuum plasticity theory is used, where plastic flow occurs when a yield criterion is satisfied. The initial yielding can be defined by continuous surface in stress space by  $f(\sigma_{ij}) = 0$ , which defines the boundary between the elastic and plastic domains. Since phenomenological model

has simpler mathematical form than crystal plasticity, it is more convenient to use for finite element programming. Additionally, it needs little number of parameters which can be found from simple experiments, such as uniaxial tensile tests [62].

Plasticity laws are on the basis of several observations of plastic deformation. First of all, since plasticity is assumed to be volume conserving and independent of hydrostatic pressure, deviatoric stresses are used for the plasticity equations. Secondly, since plasticity is irreversible texture, energy is dissipated while plastic deformation proceeds. This dissipation has two important results. First result of plastic dissipation is, the elastic strains are recovered while the plastic strains persist in the body upon unloading. This allows total strain being written as the summation of elastic and plastic strains ( $\varepsilon_{ij} = \varepsilon_{ij}^e + \varepsilon_{ij}^p$ ). Second result is path dependency, which means that, on the contrary of elasticity, when current values of stress and strains given it is needed some functional relationships between the current loading state and history of the body to find the other quantities [64].

The yield surface can be stated as the main part of classical plasticity theory. Stress state is considered necessary for plastic deformation when it is formulated in stress space. Moreover, Drucker's postulate states that a yield surface must be convex to ensure the uniqueness of plastic strain rate for a given stress state. The general form of the yield surface,  $f$  can be expressed as [68],

$$f = \bar{\sigma}(\sigma_{ij}) - k \leq 0 \quad (4.1)$$

where  $\sigma_{ij}$  is tensor stress state. When  $k$  is equal to effective stress,  $f=0$ , and material plastically deforms. Otherwise, the stress state is elastic and elastic deformation takes place. An associated flow rule was also implied from Drucker's postulate for stable (non-softening) materials, thus the direction of the plastic strain rate is normal to the yield surface [64].

$$d\varepsilon_{ij} = d\lambda \frac{\partial f}{\partial \sigma_{ij}} \quad (4.2)$$

where  $d\lambda$  is a plastic multiplier.

## 4.2 Introduction to Plastic Anisotropy

There are different sources of material anisotropy. One of them is considered as slip plane anisotropy. The distributions of the active slip systems also cause anisotropy, in materials which has non-random grain orientations [64]. Sheet metals naturally present mechanical anisotropy due to their grain orientation. Typically, sheet metals are orthotropic, with mirror symmetry axes aligned with the sheet rolling (RD), transverse (TD) and normal (ND) directions, as shown in Figure 4.1 [62].

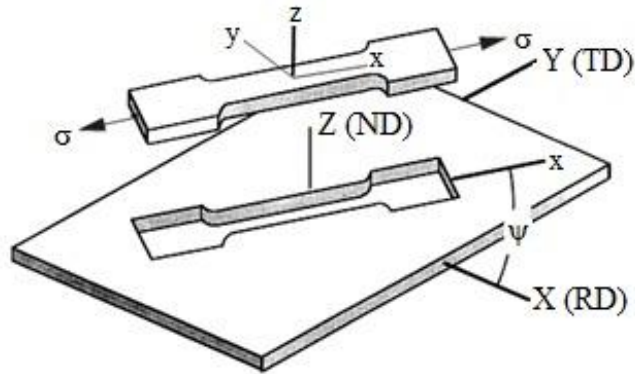


Figure 4.1: Schematics of coordinate systems of a sheet (X-Y-Z) and a sheet rolling directions [62].

The variation of the plastic behavior of the rolled sheet metal with direction is defined by a quantity called Lankford parameter or anisotropy coefficient. The anisotropy coefficient, r-value, is defined as follows [65]:

$$r_{\psi} = \frac{\varepsilon_2^p}{\varepsilon_3^p} \quad (4.3)$$

where  $\varepsilon_2^p$  and  $\varepsilon_3^p$  are true plastic strains in width and thickness directions respectively. As shown in Figure 4.1 for different angles to the sheet rolling directions, different r-values can be determined by simple tensile test [62].

In practice, it is hard to measure accurately small changes of the sheet thickness. Using the volume consistency (i.e.,  $\varepsilon_1^p + \varepsilon_2^p + \varepsilon_3^p = 0$ ), r-values can be calculated properly as shown below [62],

$$r_\psi = -\frac{\varepsilon_2^p}{\varepsilon_1^p + \varepsilon_2^p} \quad (4.4)$$

while  $\varepsilon_1^p$  is the plastic strain in the longitudinal direction.

The anisotropy coefficient has a big influence on sheet formability. It is a measure of the resistance to thinning or localized deformation, which usually come before failure in sheet metal forming. Therefore, to have a good formability it is wanted to have high r-values. An averaged r-values which is also called as normal anisotropy, can be defined as [62],

$$\bar{r} = \frac{r_0 + 2r_{45} + r_{90}}{4} \quad (4.5)$$

r-values are correlated with the drawability of the sheet metals. In above equation  $r_0$ ,  $r_{45}$  and  $r_{90}$  are the r-values measured at  $0^\circ$ ,  $45^\circ$  and  $90^\circ$  respectively, from the sheet rolling direction. A measure of the variation of normal anisotropy with the angle to the rolling direction is given by quantity [65],

$$\Delta r = \frac{r_0 - 2r_{45} + r_{90}}{2} \quad (4.6)$$

which is also known as a planar anisotropy. Planar anisotropy is related to the earing profile in deep drawn cups [65].

### 4.3 Hardening Rules

Plastic deformations are seen in the material when the elastic limit stress is exceeded. This starting and continuation of plastic flow is governed by a yield function. The change and evolution of the yield surface due to strain is also thought as important as initial shape of the yield surface.

In case of increase the flow stress, yield surface must change its shape or position to accommodate this new stress state due to the definition of all stress states are laid on or within the yield surface. During deformation, gradual rotation of crystal orientation is seen, which causes material texture change [64].

#### 4.3.1 Perfect Plasticity

A material model is said to be perfectly plastic if no hardening is allowed, that is, the yield stress level does not depend on the degree of plastification. In this case, the yield surface remains fixed regardless of any deformation process. Figure 4.2 shows the stress-strain curve of typical uniaxial cyclic test with perfectly plastic model [66].

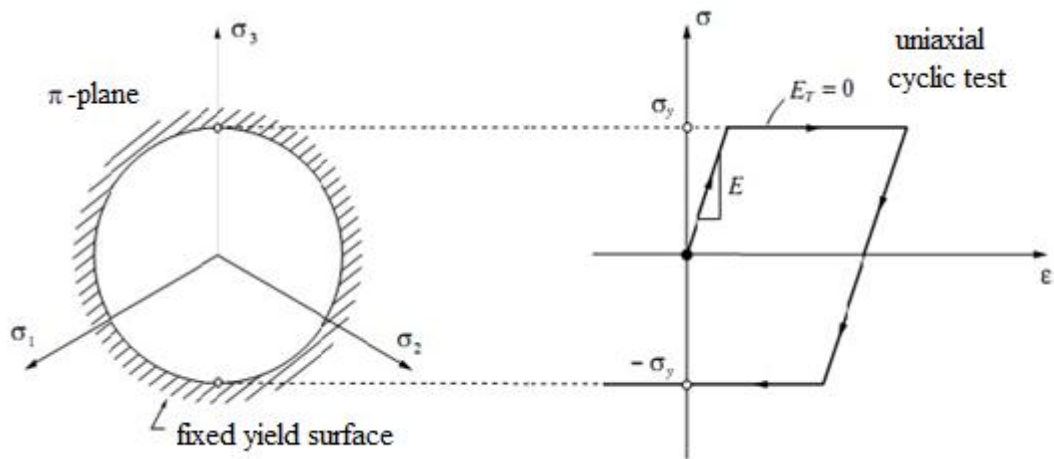


Figure 4.2: Uniaxial test and  $\pi$ - plane representation of perfect plasticity [66].

Perfectly plastic models are particularly suitable for the analysis of the stability of structures and soils, also used for the determination of limit loads and safety factors [66].

#### 4.3.2 Isotropic Hardening

In the plastic region, metals are typically work-hardened where the flow stress monotonically increases with accumulated plastic strain. After material is plastically deformed, the stress stays on the yield surface. This surface acts as a plastic potential,

from which the plastic strains are derived when associated flow rule is adopted. For isotropic hardening yield surface can be defined mathematically as follows [62].

$$f(\sigma_{ij}, R) = \bar{\sigma}(\sigma_{ij}) - |\sigma_{y0} + R(\bar{\epsilon}^p)| = 0 \quad (4.7)$$

$R$  represents the isotropic expansion of the yield surface. The change of the yield surface size (isotropic hardening) is indicated by the change of the yield strength,  $\sigma_y$  ( $\sigma_y = |\sigma_{y0} + R(\bar{\epsilon}^p)|$ ), When  $\bar{\epsilon}^p = 0$  in the above equation the initial yield strength is  $\sigma_{y0}$ .

A plasticity model is said to be isotropic hardening if the evolution of the yield surface is such that, at any state of hardening, it corresponds to a uniform (isotropic) expansion of the initial yield surface, without translation as shown in Figure 4.3 [66].

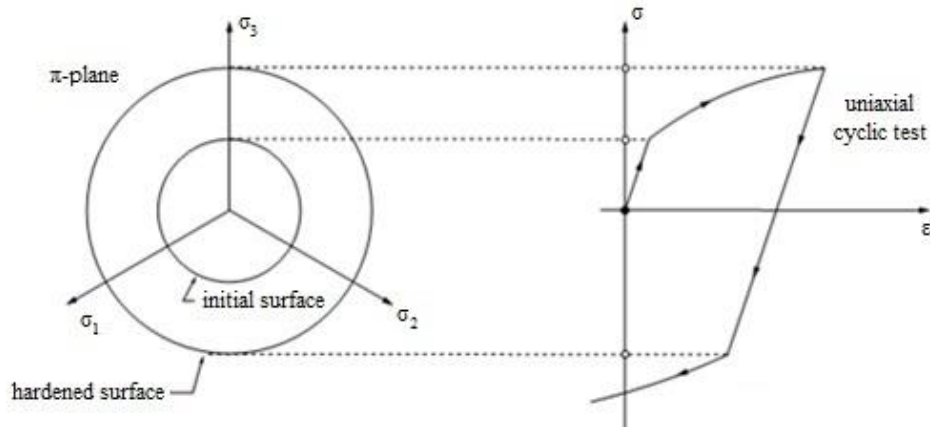


Figure 4.3: Uniaxial test and  $\pi$ - plane representation of isotropic hardening [66].

In the literature, there are three isotropic hardening laws which are widely used:

$$R(\bar{\epsilon}^p) = \begin{cases} H\bar{\epsilon}^p & \text{Linear hardening} \\ K(\bar{\epsilon}^p)^n & \text{Power law hardening} \\ R_0\bar{\epsilon}^p + R_\infty(1 - e^{-b\bar{\epsilon}^p}) & \text{Voce's law hardening} \end{cases} \quad (4.8)$$

where  $H$  is called the linear hardening modulus,  $\bar{\epsilon}^p$  is the accumulated equivalent plastic strain, and it is defined as,

$$\bar{\epsilon}^p(t) = \int_0^t \sqrt{\frac{2}{3} d\epsilon_{ij}^p d\epsilon_{ij}^p} dt = \int_0^t \sqrt{\frac{2}{3}} \|d\epsilon_{ij}^p\| dt \quad (4.9)$$

### 4.3.3 Kinematic Hardening

Principal drawback of isotropic hardening is considered as the excluding the Bauschinger effect. It is frequently observed in experiments that, after being loaded (and hardened) in one direction, many materials show a decreased resistance to plastic yielding in the opposite direction [66]. This phenomenon is known as the Bauschinger effect and can be modeled with the introduction of kinematic hardening.

When the yield surfaces preserve their shape and size but translate in the stress space as a rigid body, kinematic hardening is said to take place. Motion of the yield surface (kinematic hardening) is described by the translation of its center, represented by the back stress tensor  $\alpha_{ij}$  which is graphically shown in Figure 4.4 [62]

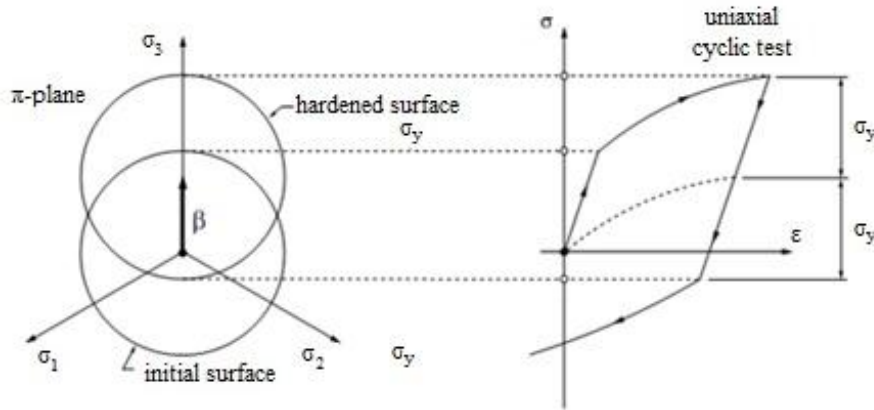


Figure 4.4: Uniaxial test and  $\pi$ - plane representation of kinematic hardening and bauschinger effect [66].

Simple linear kinematic hardening proposed by Prager [64] and Ziegler [64] can be expressed as,

$$f = \bar{\sigma}(\sigma_{ij} - \alpha_{ij}) - k \leq 0 \quad (4.10)$$

Residual stresses of the Bauschinger effect is considered as the origins of back stress. Even if these above hardening models are useful for the basis to predict the real material behavior, they fail for highly nonlinear materials. It has been seen that some of the hardening models that describe highly nonlinear materials better. These are the multi-surface hardening models, such as that proposed by Mronz [64] or the family of nonlinear kinematic hardening models, which was first introduced by Armstrong and Frederick [64] and then has been expanded by many researchers including Chaboche [64], Geng [64] and Teodoisu [64].

#### 4.3.4 Combined Hardening

Rather than purely isotropic or purely kinematic hardening, real life materials show in general a combination of both which is represented in Figure 4.5. Under plastic straining, the yield surface expands/shrinks and translates simultaneously in stress space. The combination type hardening laws are considered suitable in predicting the springback as well as failure in forming operations, since it can account for the Bauschinger effect and the transient behavior during unloading. Yield function can be defined for combined hardening as follows,

$$f(\sigma_{ij}, \alpha_{ij}, R) = \bar{\sigma}(\sigma_{ij} - \alpha_{ij}) - |\sigma_{y0} + R(\bar{\epsilon}^p)| = 0 \quad (4.11)$$

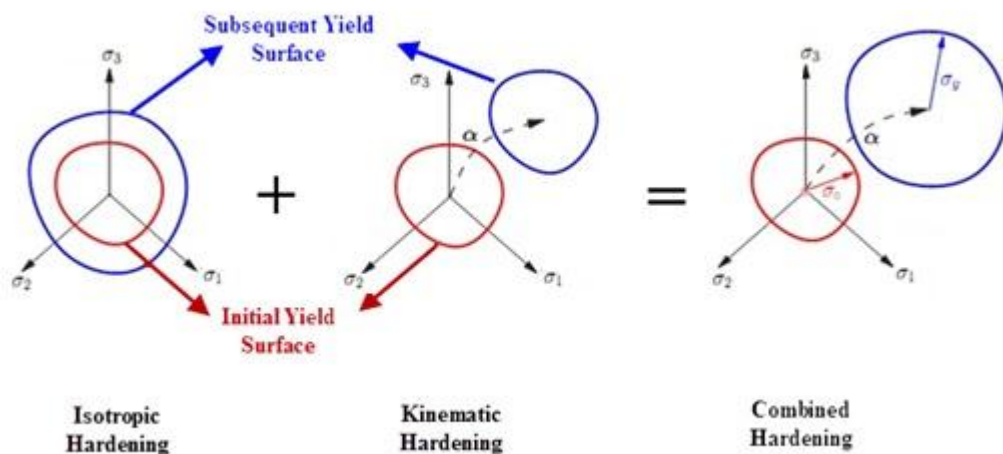


Figure 4.5: Schematic view of combined hardening [62].

## 4.4 Yield Functions

For sufficiently small values of stress and strain, a metal will preserve its original shape upon unloading. When the material has been subjected to stress exceeding yield stress, the current stress becomes the new yield limit after the material is unloaded. For a multi-axial state of stress, a material's yield limit is mathematically described by a yield criterion [67].

### 4.4.1 von Mises Yield Function

The von Mises yield criterion [64] is an isotropic yield surface, based on the assumption that, plastic deformation occurs when the distortional energy reaches a certain critical value. In Cartesian coordinates, the von Mises yield surface takes the following form [64].

$$(\sigma_y - \sigma_z)^2 + (\sigma_z - \sigma_x)^2 + (\sigma_x - \sigma_y)^2 + 6(\tau_{yz}^2 + \tau_{xz}^2 + \tau_{xy}^2) = 2\bar{\sigma}^2 \quad (4.12)$$

in terms of principal stresses it can be expressed as,

$$(\sigma_1 - \sigma_2)^2 + (\sigma_2 - \sigma_3)^2 + (\sigma_3 - \sigma_1)^2 = 2\bar{\sigma}^2 \quad (4.13)$$

The von Mises yield function is regularly used for basic analysis because it can be analytically differentiated, which makes it very easy to implement [64]. The von Mises yield function is also represented in principal strains, which implies isotropic behavior however, most engineering materials are strongly anisotropic.

### 4.4.2 Hill'48 Yield Criterion

In order to describe orthotropic plasticity of sheet metals, Hill first proposed a quadratic yield function [64]. It has been widely used for sheet forming simulations, since it can be applied to general stress states, and can be easily implemented into finite element codes. In fact, it is readily available from most commercial finite element codes, such as Ls-Dyna [62].

Due to thermo-mechanical processing, metal sheets exhibit orthotropic symmetry with the axes of orthotropy being aligned with the rolling direction, the transverse

direction, and the normal direction to the plane of the sheet ( $x$ ,  $y$  and  $z$  respectively). In 1948, Hill proposed a generalization of the von Mises isotropic yield criterion to orthotropy. Thus, this yield criterion is expressed by a quadratic function as [67],

$$f = F(\sigma_y - \sigma_z)^2 + G(\sigma_z - \sigma_x)^2 + H(\sigma_x - \sigma_y)^2 + 2L\tau_{yz}^2 + 2M\tau_{zx}^2 + 2N\tau_{xy}^2 - \bar{\sigma}^2 = 0 \quad (4.14)$$

where  $F$ ,  $G$ ,  $H$ ,  $L$ ,  $M$  and  $N$  are anisotropy constants, and  $x$ ,  $y$  and  $z$  are the orthotropy axes. When,

$$F = G = H = \frac{1}{6k^2}$$

$$L = M = N = \frac{1}{2k^2}$$

Equation 4.14 reduces to the von Mises criterion (Equation 4.12).

The coefficients involved in the expression of Hill's yield criterion can be determined from simple mechanical tests.  $X$ ,  $Y$  and  $Z$  are the tensile yield strength in  $x$ ,  $y$  and  $z$  directions respectively, according to Hill's theory they can be defined as [67].

$$X = \sqrt{\frac{1}{G + H}} \quad Y = \sqrt{\frac{1}{F + H}} \quad Z = \sqrt{\frac{1}{G + F}} \quad (4.15)$$

Thus,

$$2F = \frac{1}{Y^2} + \frac{1}{Z^2} - \frac{1}{X^2} \quad 2G = -\frac{1}{Y^2} + \frac{1}{Z^2} + \frac{1}{X^2} \quad 2H = \frac{1}{Y^2} - \frac{1}{Z^2} + \frac{1}{X^2} \quad (4.16)$$

Assume  $R$ ,  $S$  and  $T$  is the shear yield strengths corresponding to the  $yz$ ,  $zx$  and  $xy$  directions respectively,

$$2L = \frac{1}{R^2} \quad 2M = \frac{1}{S^2} \quad 2N = \frac{1}{T^2} \quad (4.17)$$

Assuming plastic incompressibility, the Lankford coefficient for uniaxial tensile loading in the x-direction can be written as [67].

$$r_{xx} = \frac{d\varepsilon_{yy}}{d\varepsilon_{zz}} = -\frac{d\varepsilon_{yy}}{d\varepsilon_{xx} + d\varepsilon_{yy}} = -\frac{\frac{\partial f}{\partial \sigma_{yy}}}{\frac{\partial f}{\partial \sigma_{xx}} + \frac{\partial f}{\partial \sigma_{yy}}} \quad (4.18)$$

Likewise,  $r_\alpha$ , the strain ratio corresponding to a uniaxial tensile loading at an arbitrary angle,  $\alpha$ , to the x-direction which is shown in Figure 4.6 is given by [67],

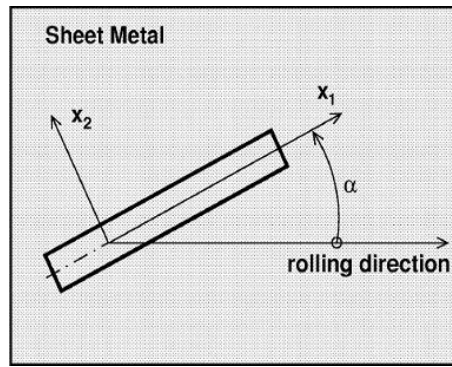


Figure 4.6: Orientation of test specimen with the rolling direction of the sheet [67].

$$r_\alpha = -\frac{\sin^2 \alpha \frac{\partial f}{\partial \sigma_{xx}} - \sin 2\alpha \frac{\partial f}{\partial \sigma_{xy}} + \cos^2 \alpha \frac{\partial f}{\partial \sigma_{yy}}}{\frac{\partial f}{\partial \sigma_{xx}} + \frac{\partial f}{\partial \sigma_{yy}}} \quad (4.19)$$

In case of plane stress, where  $\sigma_{13} = \sigma_{23} = \sigma_{33} = 0$ , Equation 4.14 can be written as,

$$(G + H)\sigma_x^2 - 2H\sigma_x\sigma_y + (H + F)\sigma_y^2 + 2N\tau_{xy}^2 = 1 \quad (4.20)$$

The coefficients  $G$ ,  $H$  and  $F$  can be determined from the r-values of the sheet metals measured at different angles to the sheet rolling direction

$$r_0 = \frac{H}{G} \quad r_{45} = \frac{N}{F + G} - \frac{1}{2} \quad r_{90} = \frac{H}{F} \quad (4.21)$$

while the determination of  $N$  in Equation 4.20 requires shear test.

When the principal directions of the stress tensor are coincident with the anisotropic axes, i.e.,  $\sigma_{ij} = 0$  where  $i \neq j$ , then the Equation 4.20 becomes

$$\sigma_1^2 - \frac{2r_0}{1+r_0}\sigma_1\sigma_2 + \frac{r_0(1+r_{45})}{r_{90}(1+r_0)}\sigma_2^2 = \sigma_{RD}^2 \quad (4.22)$$

where  $\sigma_1$  and  $\sigma_2$  are the principal stresses and  $\sigma_{RD}$  is the yield stress in uniaxial tension (i.e., parallel to sheet rolling direction). Now only three material properties,  $r_0$ ,  $r_{90}$  and the uniaxial tensile stress  $\sigma_{RD}$  are needed to determine for the yield surface. This makes Hill'48 yield criterion easy and user friendly [62].

#### 4.4.3 Hill's 1979 Yield Criterion

It has been seen that Hill's 1948 criterion fails to provide an accurate analysis for materials with r-values less than 1. In order to overcome this limitation, Hill's 1979 yield criterion was proposed which incorporates a material characteristic 'm' as shown in the equation below [68],

$$\begin{aligned} \bar{\sigma}^m = & f|\sigma_y - \sigma_z|^m + g|\sigma_z - \sigma_x|^m + h|\sigma_x - \sigma_y|^m + a|2\sigma_x - \sigma_y - \sigma_z|^m \\ & + b|2\sigma_y - \sigma_x - \sigma_z|^m + d|2\sigma_z - \sigma_x - \sigma_y|^m \end{aligned} \quad (4.23)$$

The exponent 'm' is related to the crystallographic texture,  $m = 6$  and  $m = 8$  are found to be suitable for BCC (body centered cubic) and FCC (face centered cubic) materials respectively. It has been observed that for planar anisotropy, convexity of the yield surface only assured with  $a = b = g = f = 0$  [62]. Then the above equation takes the following form,

$$\bar{\sigma}^m = d|\sigma_x + \sigma_y|^m + h|\sigma_x - \sigma_y|^m \quad (4.24)$$

Parameters  $d$  and  $h$  can be determined from the uniaxial tensile test along the sheet rolling direction:

$$\frac{h}{d} = 2r + 1$$

and

$$d + h = 1$$

Then Equation 4.23 can be rewritten for planar anisotropy as,

$$2(1+r)\sigma_{RD}^m = |\sigma_x + \sigma_y|^m + (1+2r)|\sigma_x - \sigma_y|^m \quad (4.25)$$

#### 4.4.4 Hill's 1990 Yield Criterion

Since, Hill's 1979 yield criterion can only be used when the directions of the principal stresses are coincident with the orthotropic axes. This causes severe limitations of application. Therefore, new yield criterion Hill's 1990 was proposed. According to Hill's 1990 criterion, yield function can be written as [65],

$$\begin{aligned} f = \frac{1}{2} & \left[ |\sigma_x + \sigma_y|^m + \left( \frac{\sigma_{bi}^m}{t^m} \right) \left| (\sigma_x + \sigma_y)^2 + 4\tau_{xy}^2 \right|^m \right. \\ & + \left| \sigma_x^2 + \sigma_y^2 + 2\tau_{xy}^2 \right|^{\frac{m}{2}-1} \left\{ -2a(\sigma_x^2 - \sigma_y^2) \right. \\ & \left. \left. + b(\sigma_x - \sigma_y)^2 \right\} \right]^{\frac{1}{m}} - \sigma_{bi} = 0 \end{aligned} \quad (4.26)$$

where  $\sigma_{bi}$  is the biaxial stress. Components of the above equation are defined from the following equations,

$$\frac{\sigma_{bi}^m}{t^m} = \left( \frac{2\sigma_{bi}}{\sigma_{45}} \right)^m - 1 \quad (4.27)$$

$$a = \frac{1}{4} \left\{ \left( \frac{2\sigma_{bi}}{\sigma_{90}} \right)^m - \left( \frac{2\sigma_{bi}}{\sigma_0} \right)^m \right\} \quad (4.28)$$

$$b = \frac{1}{2} \left\{ \left( \frac{2\sigma_{bi}}{\sigma_0} \right)^m + \left( \frac{2\sigma_{bi}}{\sigma_{90}} \right)^m \right\} - \left( \frac{2\sigma_{bi}}{\sigma_{45}} \right)^m \quad (4.29)$$

where  $m > 1$ .

#### 4.4.5 Hill's 1993 Quadratic Anisotropy Yield Criterion

The yield criteria, Hill's 1948, Hill's 1979 and Hill's 1990 mentioned above causes some difficulties when used in the mathematical models of FLD's. Normally, they are expressed by non-quadratic or trigonometric functions; they cannot model the

entire variety of peculiar situations that may appear in practice; it is difficult to identify the material parameters by simple tests [69].

In order to overcome these drawbacks, Hill has proposed in 1993 a new yield criterion [65] for orthotropic sheets, valid in planar anisotropy. Hill's 1993 criterion is a new quadratic form yield criterion which can be expressed as [68],

$$\frac{\sigma_x^2}{\sigma_y^2} - \frac{e\sigma_x\sigma_y}{\sigma_0\sigma_{90}} + \frac{\sigma_y^2}{\sigma_{90}^2} + \left\{ (p+q) - \frac{p\sigma_x+q\sigma_y}{\sigma_0} \right\} \frac{\sigma_x\sigma_y}{\sigma_0\sigma_{90}} = 1 \quad (4.30)$$

Parameters 'p' and 'q' are in the following form,

$$\left( \frac{1}{\sigma_0} + \frac{1}{\sigma_{90}} - \frac{1}{\sigma_{bi}} \right) p = \frac{2r_0(\sigma_{bi} - \sigma_{90})}{(1+r_0)\sigma_0^2} - \frac{2r_{90}\sigma_{bi}}{(1+r_{90})\sigma_{90}^2} + \frac{e}{\sigma_0} \quad (4.31)$$

$$\left( \frac{1}{\sigma_0} + \frac{1}{\sigma_{90}} - \frac{1}{\sigma_{bi}} \right) q = \frac{2r_{90}(\sigma_{bi} - \sigma_0)}{(1+r_{90})\sigma_{90}^2} - \frac{2r_0\sigma_{bi}}{(1+r_0)\sigma_0^2} + \frac{e}{\sigma_0} \quad (4.32)$$

where 'e' can be expressed as,

$$\frac{e}{\sigma_0\sigma_{90}} = \frac{1}{\sigma_0^2} + \frac{1}{\sigma_{90}^2} - \frac{1}{\sigma_{bi}^2} \quad (4.33)$$

Hill's 1993 yield criterion may be written as,

$$\sigma_x^2 - \left( 2 - \frac{\sigma_u^2}{\sigma_{bi}^2} \right) \sigma_x\sigma_y + \sigma_y^2 + \left\{ (p+q) - \frac{p\sigma_x+q\sigma_y}{\sigma_{bi}} \right\} \sigma_x\sigma_y = Y^2 \quad (4.34)$$

where  $\sigma_u$  is ultimate stress. If it is assumed  $\sigma_0 = \sigma_{90} = Y$ , where Y is the yield stress for uniaxial tension and under the condition of the normal anisotropy  $r_0 = r_{90} = r$ , parameters 'p' and 'q' are expressed as [68],

$$p = q \frac{\left( \frac{2}{1+r} - \frac{\sigma_u^2}{\sigma_{bi}^2} \right)}{\left( 2 - \frac{\sigma_u^2}{\sigma_{bi}^2} \right)} \quad (4.35)$$

Plastic potential (yield function) can be written in the following form,

$$f = \frac{1}{2\bar{\sigma}^2} \left[ \sigma_x^2 - \left( 2 - \frac{\sigma_u^2}{\sigma_{bi}^2} \right) \sigma_x \sigma_y + \left\{ (p+q) - \frac{p\sigma_x + q\sigma_y}{\sigma_{bi}} \right\} \sigma_x \sigma_y \right] - \frac{1}{2} \quad (4.36)$$

Under the action of associated flow rule its components can be shown in the following form,

$$\frac{\partial f}{\partial \sigma_x} = 2\sigma_x - \left( 2 - p - q - \frac{\sigma_u^2}{\sigma_{bi}^2} \right) \sigma_y - \frac{q}{\sigma_{bi}} \sigma_y^2 - \frac{2p}{\sigma_{bi}} \sigma_x \sigma_y \quad (4.37)$$

$$\frac{\partial f}{\partial \sigma_y} = 2\sigma_y - \left( 2 + p + q - \frac{\sigma_u^2}{\sigma_{bi}^2} \right) \sigma_x - \frac{p}{\sigma_{bi}} \sigma_x^2 - \frac{2q}{\sigma_{bi}} \sigma_x \sigma_y \quad (4.38)$$

#### 4.4.6 Hosford's Yield Criterion

Hosford's non-quadratic yield function can also be made anisotropic through the addition of material anisotropy coefficients F, G and H [64],

$$F|\sigma_y - \sigma_z|^m + G|\sigma_z - \sigma_x|^m + H|\sigma_x - \sigma_y|^m = 2\bar{\sigma}^2 \quad (4.39)$$

This yield function is also of limited use since it also requires that, the principal stress directions and the anisotropy axis should be coincided. Barlat's 1991 yield criterion overcomes this deficiency by introducing the anisotropy to the stress vector rather than the yield function itself [64].

#### 4.4.7 Barlat's 1991 Yield Criterion

Barlat's 1991 criterion can be written by using the Hosford's non-quadratic yield function as below [64],

$$|S_y - S_z|^m + |S_z - S_x|^m + |S_x - S_y|^m = 2\bar{\sigma}^m \quad (4.40)$$

where 'm' is a material constant. Generally,  $m = 6$  and  $m = 8$  are used for BCC and FCC metals, respectively.  $S_{ii}$  ( $i = 1, 2, 3$ ) is the eigenvalues tensor of the transformed deviatoric stress [64],

$$[S_{ij}] = \begin{bmatrix} S_x & S_{xy} & S_{xz} \\ S_{xy} & S_y & S_{yz} \\ S_{xz} & S_{yz} & S_z \end{bmatrix} \quad (4.41)$$

whose components are defined as follows,

$$S_x = \frac{c_3(\sigma_x - \sigma_y) - c_2(\sigma_z - \sigma_x)}{3} \quad (4.42)$$

$$S_y = \frac{c_1(\sigma_y - \sigma_z) - c_3(\sigma_x - \sigma_y)}{3} \quad (4.43)$$

$$S_z = \frac{c_2(\sigma_z - \sigma_x) - c_1(\sigma_y - \sigma_z)}{3} \quad (4.44)$$

$$S_{xy} = c_6\tau_{xy} \quad (4.45)$$

$$S_{xz} = c_4\tau_{xz} \quad (4.46)$$

$$S_{yz} = c_5\tau_{yz} \quad (4.47)$$

where  $c_1, c_2, c_3, c_4, c_5$  and  $c_6$  are anisotropy coefficients. Parameters  $c_1, c_2$  and  $c_3$  can be determined from the uniaxial tension tests along rolling, transverse and normal directions, to determine the parameters  $c_4, c_5$  and  $c_6$  shear tests along these directions are also needed. In case of plane stress where  $\sigma_3 = 0$ , parameters  $c_1, c_2$  and  $c_3$  can be found from the uniaxial tensile test. Moreover, parameter  $c_6$  can be determined by uniaxial tensile stress in the directions of  $45^\circ$  from the rolling direction, instead of in plane shear test. For aluminum sheets, Barlat's 1991 yield criterion works better than Hill's 1948 criterion [62].

#### 4.4.8 Barlat's 1994 Yield Criteria

It has been observed that Barlat's 1991 yield criterion have some limitations, especially in fitting the behavior in shear stress states. Therefore, two improved iterations of the Barlat's 1991 yield function were proposed which are Barlat's 1994 and Barlat's 1996 criteria. These yield criteria added additional terms to the yield equation to account for this discrepancy in shear [64].

In order to represent the behavior of the *Al-Mg* binary materials mathematically, in 1994, Barlat proposed a new yield criterion called YLD94, in which all the shear stress are zero [70]:

$$\phi_{YLD94} = \alpha_x |S_y - S_z|^m + \alpha_y |S_z - S_x|^m + \alpha_z |S_x - S_y|^m - 2\bar{\sigma}^m = 0 \quad (4.48)$$

$S_x$ ,  $S_y$  and  $S_z$  are the normal components of the stress tensor,  $S_{ij}$ . To obtain orthotropic properties the components of the  $S_{ij}$  are given with respect to the components of Cauchy stress tensor,  $\sigma_{ij}$ , and they are modified by the linear operator  $C_{ijkl}$  in the following manner [70]:

$$S_{ij} = C_{ijkl}\sigma_{kl} \quad (4.49)$$

Where

$$S_x = \frac{c_2 + c_3}{3}\sigma_x + \frac{-c_3}{3}\sigma_y + \frac{-c_2}{3}\sigma_z \quad (4.50a)$$

$$S_y = \frac{-c_3}{3}\sigma_x + \frac{c_3 + c_1}{3}\sigma_y + \frac{-c_1}{3}\sigma_z \quad (4.50b)$$

$$S_z = \frac{-c_2}{3}\sigma_x + \frac{-c_1}{3}\sigma_y + \frac{c_1 + c_2}{3}\sigma_z \quad (4.50c)$$

$c_1, c_2, c_3, \alpha_x, \alpha_y$  and  $\alpha_z$  are material coefficients that describe anisotropy

#### 4.4.9 Barlat's 1996 Yield Criteria

To define an improved yield function for plane stress case the yield criterion YLD94 was extended to the Barlat yield criterion YLD96 [71] which includes the most general stress tensor with six components as shown,.

$$\phi_{YLD96} = \alpha_1 |S_2 - S_3|^m + \alpha_2 |S_3 - S_1|^m + \alpha_3 |S_1 - S_2|^m - 2\bar{\sigma}^m = 0 \quad (4.51)$$

with  $m = 6$  and  $m = 8$  for BCC and FCC materials, respectively. In the criterion represented by Equation 4.51,  $S_1, S_2$  and  $S_3$  are the principal values of the isotropic equivalent stress tensor  $S_{ij}$ , that for orthotropic symmetry is given by [72],

$$S_{ij} = C_{ijkl}\sigma_{kl} \quad (4.52)$$

$$C_{ijkl} = \begin{bmatrix} \frac{c_2 + c_3}{3} & \frac{-c_3}{3} & \frac{-c_2}{3} & 0 & 0 & 0 \\ \frac{-c_3}{3} & \frac{c_3 + c_1}{3} & \frac{-c_1}{3} & 0 & 0 & 0 \\ \frac{-c_2}{3} & \frac{-c_1}{3} & \frac{c_1 + c_2}{3} & 0 & 0 & 0 \\ 0 & 0 & 0 & c_4 & 0 & 0 \\ 0 & 0 & 0 & 0 & c_5 & 0 \\ 0 & 0 & 0 & 0 & 0 & c_6 \end{bmatrix} \quad (4.53)$$

For the plane stress case, when  $\sigma_z = \sigma_{zy} = \sigma_{zx} = 0$ , Equation 4.52 reduces to

$$S_{ij} = \begin{Bmatrix} S_x \\ S_y \\ S_z \\ S_{xy} \end{Bmatrix} = \begin{bmatrix} \frac{c_2 + c_3}{3} & \frac{-c_3}{3} & \frac{-c_2}{3} & 0 \\ \frac{-c_3}{3} & \frac{c_3 + c_1}{3} & \frac{-c_1}{3} & 0 \\ \frac{-c_2}{3} & \frac{-c_1}{3} & \frac{c_1 + c_2}{3} & 0 \\ 0 & 0 & 0 & c_6 \end{bmatrix} \begin{Bmatrix} \sigma_x \\ \sigma_y \\ 0 \\ \tau_{xy} \end{Bmatrix} \quad (4.54)$$

the principal values of  $S_{ij}$  are found as follows:

$$S_{1,2} = \frac{S_x + S_y}{2} \pm \sqrt{\left(\frac{S_x - S_y}{2}\right)^2 + S_{xy}^2} \quad (4.55)$$

$$S_3 = -(S_1 + S_2) \quad (4.56)$$

the anisotropy coefficients,  $\alpha_1$ ,  $\alpha_2$  and  $\alpha_3$  in Equation 4.51 are defined as,

$$\alpha_1 = \alpha_x \cos^2 \theta + \alpha_y \sin^2 \theta \quad (4.57)$$

$$\alpha_2 = \alpha_x \sin^2 \theta + \alpha_y \cos^2 \theta \quad (4.58)$$

$$\alpha_3 = \alpha_{z0} \cos^2 2\theta + \alpha_{z1} \sin^2 2\theta \quad (4.59)$$

In the above equations,  $c_1$ ,  $c_2$ ,  $c_3$ ,  $c_6$ ,  $\alpha_x$ ,  $\alpha_y$  and  $\alpha_{z0}$  and  $\alpha_{z1}$  are the coefficients that describe the anisotropy of the material. The parameter  $2\theta$  represents the angle between the line OA and the axis of principal stresses  $S_1$  and  $S_2$  as shown in Figure 4.7 below and is equal to [72]:

$$2\theta = \arctan\left(\frac{2S_{xy}}{S_x - S_y}\right) \quad (4.60)$$

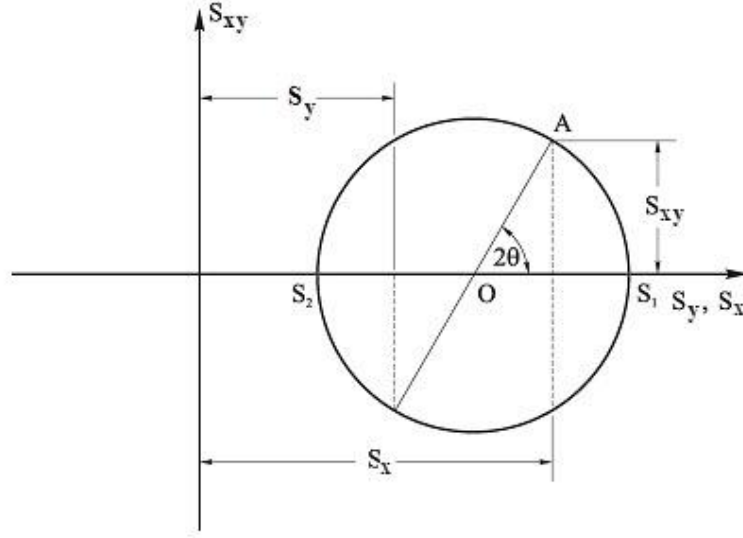


Figure 4.7: Determination of the anisotropy parameter  $2\theta$  from Mohr Circle [72].

With this yield function it is possible to increase the yield stress at pure shear without increasing the other plane strain yield stresses. It should be noted that by setting the anisotropy coefficients  $c_1 = c_2 = c_3 = c_6 = \alpha_1 = \alpha_2 = \alpha_3 = 1$  and  $m = 2$  (quadratic) in the criterion given by Equation 4.51, the von Mises isotropic yield function is recovered [72].

#### 4.4.10 Barlat's Yld2000-2D Yield Criterion

The yield function Yld2000-2D was created to assure convexity and to simplify the determination of the material parameters for plane stress case. This yield surface is a linear combination of two convex yield functions, which assures the convexity of the resultant yield surface [64].

$$2\sigma^a = \phi' + \phi'' \quad (4.61)$$

where  $a \geq 1$  is a material parameter and generally, 'a' is recommended to be 8 for FCC materials, like 'm' value is used in Hosford's criterion [64],

$$\phi' = |X_1' - X_2'|^a \quad (4.62)$$

$$\phi'' = |2X_2'' + X_1''|^a + |2X_1'' - X_2''|^a \quad (4.63)$$

The values  $X_i'$  and  $X_i''$  are the principal directions of the following linear transformations of the stress deviators which are defined as [64],

$$\begin{bmatrix} X_{xx}' \\ X_{yy}' \\ X_{xy}' \end{bmatrix} = \begin{bmatrix} C_{11}' & C_{12}' & 0 \\ C_{12}' & C_{22}' & 0 \\ 0 & 0 & C_{33}' \end{bmatrix} \begin{bmatrix} S_{xx} \\ S_{yy} \\ S_{xy} \end{bmatrix} \quad (4.64)$$

$$\begin{bmatrix} X_{xx}'' \\ X_{yy}'' \\ X_{xy}'' \end{bmatrix} = \begin{bmatrix} C_{11}'' & C_{12}'' & 0 \\ C_{12}'' & C_{22}'' & 0 \\ 0 & 0 & C_{33}'' \end{bmatrix} \begin{bmatrix} S_{xx} \\ S_{yy} \\ S_{xy} \end{bmatrix} \quad (4.65)$$

These eight parameters can be calculated from the yield stresses and r-values of tensile tests in the directions of  $0^\circ$ ,  $45^\circ$  and  $90^\circ$  from the rolling direction and from the balanced biaxial test. In addition to material parameter calculations are simplified and the criterion assuring the convexity, Yld2000-2D criterion is also improved the yield surface prediction over the previous Barlat's yield criteria which are, Barlat's 1991, Barlat's 1994 and Barlat's 1996 [64].

#### 4.5 Stress Strain Relations in Plastic Range

In the analyses of deep drawing and V-bending, following constitutive models are utilized; elastic plastic model with isotropic hardening, elastic plastic material model with kinematic hardening, elastic plastic material model with combined hardening, power law isotropic plasticity, piecewise linear isotropic plasticity, Barlat three-parameter, cyclic elastoplastic and Hill'48 by using commercial finite element code.

##### 4.5.1 Elastic Plastic Model with Isotropic, Kinematic and Combined Hardening

For this constitutive model, von Mises yield function can be written as

$$f = \frac{1}{2} \xi_{ij} \xi_{ij} - \frac{(\sigma_{y0} + \beta E_p \bar{\epsilon}^p)^2}{3} = 0 \quad (4.66)$$

where  $E_p$  is the plastic hardening modulus and  $\bar{\varepsilon}^p$  is effective plastic strain.

$$E_p = \frac{E_t E}{E - E_t} \quad (4.67)$$

$$\bar{\varepsilon}^p = \int_0^t \left( \frac{2}{3} d\varepsilon_{ij}^p d\varepsilon_{ij}^p \right)^{1/2} dt \quad (4.68)$$

and  $d\varepsilon_{ij}^p$  is the plastic strain rate expressed as,

$$d\varepsilon_{ij}^p = d\varepsilon_{ij} - d\varepsilon_{ij}^e \quad (4.69)$$

$$\xi_{ij} = s_{ij} - \alpha_{ij} \quad (4.70)$$

the co-rotational rate of back stress,  $\alpha_{ij}$  can be defined as [61],

$$\alpha_{ij}^{\nabla} = (1 - \beta) \frac{2}{3} E_p d\varepsilon_{ij}^p \quad (4.71)$$

hence,

$$\alpha_{ij}^{n+1} = \alpha_{ij}^n + (\alpha_{ij}^{\nabla n+\frac{1}{2}} + \alpha_{ik}^n \Omega_{kj}^{n+\frac{1}{2}} + \alpha_{jk}^n \Omega_{ki}^{n+\frac{1}{2}}) \Delta t^{n+\frac{1}{2}} \quad (4.72)$$

The superscript ( $\nabla$ ) represents any co-rotational rate. Using the Jaumann's co-rotational rate of  $\alpha$ , associated with the body spin,  $\Omega$ , yields a monotonically increasing solution for stress [73].

Isotropic, kinematic or a combination of isotropic and kinematic hardening defined by the parameter  $\beta$  in Equation 4.66. For isotropic hardening,  $\beta$  is taken as 1 and the growth of the current radius of the yield surface,  $\sigma_y$ , is  $\beta E_p \bar{\varepsilon}^p$  [61], For kinematic hardening, the parameter  $\beta$  is taken as 0, and for combined hardening the parameter  $\beta$  is taken between 0 and 1 ( $0 < \beta < 1$ )

In the implementation of the constitutive model, the deviatoric stresses are updated elastically,

$$\sigma_{ij}^* = \sigma_{ij}^n + C_{ijkl}\Delta\varepsilon_{kl} \quad (4.73)$$

where  $\sigma_{ij}^*$  is the trial stress tensor,  $\sigma_{ij}^n$  is the stress tensor at previous time step,  $C_{ijkl}$  is the elastic tangent modulus matrix and  $\Delta\varepsilon_{kl}$  is incremental strain tensor. If the yield function is not satisfied, an increment in plastic strain is computed and the stresses are updated [61].

Let  $s_{ij}^*$  represent the trial elastic deviatoric stress state at time 'n+1'

$$s_{ij}^* = \sigma_{ij}^* - \frac{1}{3}\sigma_{kk}^* \quad (4.74)$$

Yield function can be defined as,

$$\phi = \frac{3}{2}\xi_{ij}^*\xi_{ij}^* - \sigma_y^2 = \Lambda^2 - \sigma_y^2 \begin{cases} \leq 0 & \text{for elastic or neutral loading} \\ > 0 & \text{for plastic hardening} \end{cases} \quad (4.75)$$

For plastic hardening, effective strain becomes;

$$\bar{\varepsilon}^{p(n+1)} = \bar{\varepsilon}^{p(n)} + \frac{\Lambda - \sigma_y}{3G + E_p} = \bar{\varepsilon}^{p(n)} + \Delta\bar{\varepsilon}^p \quad (4.76)$$

And the stress can be written as,

$$\sigma_{ij}^{n+1} = \sigma_{ij}^* - \frac{3G\Delta\bar{\varepsilon}^p}{\Lambda}\xi_{ij}^* \quad (4.77)$$

Back stress  $\alpha_{ij}$  can be defined as,

$$\alpha_{ij}^{n+1} = \alpha_{ij}^n - \frac{(1 - \beta)E_p\Delta\bar{\varepsilon}^p}{\Lambda}\xi_{ij}^* \quad (4.78)$$

#### 4.5.2 Power Law Isotropic Plasticity

Elastoplastic behavior with isotropic hardening is provided by this model. The yield stress,  $\sigma_y$ , is a function of plastic strain and obeys the power law hardening given as,

$$\sigma_y = K\bar{\varepsilon}^n = K(\bar{\varepsilon}^e + \bar{\varepsilon}^p)^n \quad (4.79)$$

The strain to yield is found by solving for the linearly elastic loading equation

$$\sigma = E\varepsilon \quad (4.80)$$

with the strain hardening equation:

$$\sigma = K\varepsilon^n \quad (4.81)$$

If initial yield stress,  $\sigma_{y0}$ , is zero the elastic strain at yield is [61]:

$$\bar{\varepsilon}^e = \left(\frac{E}{K}\right)^{\frac{1}{n-1}} \quad (4.82)$$

If  $\sigma_{y0}$  is nonzero then elastic strain becomes,

$$\bar{\varepsilon}^e = \left(\frac{\sigma_y}{K}\right)^{\frac{1}{n}} \quad (4.83)$$

Strain rate is accounted for using the Cowper-Symonds model which scales the yield stress by a strain rate factor

$$\sigma_y = \left[1 + \left(\frac{d\varepsilon}{c}\right)^{1/l}\right] K(\bar{\varepsilon}^e + \bar{\varepsilon}^p)^n \quad (4.84)$$

Where  $l$  and  $c$  are the Cowper-Symonds strain rate parameters and  $d\varepsilon$  is the strain rate defined as:

$$d\varepsilon = \sqrt{d\varepsilon_{ij}d\varepsilon_{ij}} \quad (4.85)$$

A fully viscoplastic formulation is optional with this model which incorporates the Cowper-Symonds formulation within the yield surface [61].

### 4.5.3 Piecewise Linear Isotropic Plasticity

In this model, deviatoric stresses are determined to satisfy the von Mises yield function with hardening,

$$\sigma_y = \gamma [\sigma_{y0} + f_h(\bar{\varepsilon}^p)] \quad (4.86)$$

where the hardening function  $f_h(\bar{\varepsilon}^p)$  can be specified in tabular form as an option. Otherwise linear hardening of the form is assumed as follows [61],

$$f_h(\bar{\varepsilon}^p) = E_p(\bar{\varepsilon}^p) \quad (4.87)$$

where  $E_p$  and  $\bar{\varepsilon}^p$  are given in Equations 4.67 and 4.68 respectively. The parameter  $\gamma$  in Equation 4.86 accounts for strain rate effects. For complete generality a table defining the yield stress versus plastic strain may be defined for various levels of effective strain rate.

In the implementation of this constitutive model, the deviatoric stresses are updated elastically, the yield function is checked, and if it is satisfied the deviatoric stresses are accepted. If it is not, an increment in plastic strain is computed as [61]:

$$\Delta\bar{\varepsilon}^p = \frac{\left(\frac{3}{2} s_{ij}^* s_{ij}^*\right)^{1/2} - \sigma_y}{3G + E_p} \quad (4.88)$$

$G$  is the shear modulus. The trial deviatoric stress state  $s_{ij}^*$  is scaled back:

$$s_{ij}^{n+1} = \frac{\sigma_y}{\left(\frac{3}{2} s_{ij}^* s_{ij}^*\right)^{1/2}} s_{ij}^* \quad (4.89)$$

#### 4.5.4 Barlat Three-Parameter

This constitutive model is used at modeling of sheet metals with anisotropy under plane stress condition. It allows the use of the Lankford parameters for the definition of the anisotropic yield surface. The yield condition can be written as [61],

$$f(\sigma_{ij}, \bar{\varepsilon}^p) = \bar{\sigma}(\sigma_{11}, \sigma_{22}, \sigma_{12}) - \sigma_y(\bar{\varepsilon}^p) \leq 0 \quad (4.90)$$

where

$$\bar{\sigma}(\sigma_{11}, \sigma_{22}, \sigma_{12}) = \left(\frac{a}{2} |K_1 + K_2|^n + \frac{a}{2} |K_1 - K_2|^n + \frac{c}{2} |2K_2|^n\right)^{1/m} \quad (4.91)$$

$$K_1 = K_1(\sigma_{11}, \sigma_{22}, \sigma_{12}) = \frac{\sigma_{11} + h\sigma_{22}}{2} \quad (4.92)$$

$$K_2 = K_2(\sigma_{11}, \sigma_{22}, \sigma_{12}) = \sqrt{\left(\frac{\sigma_{11} - h\sigma_{22}}{2}\right)^2 + p^2\sigma_{12}^2} \quad (4.93)$$

and the hardening of the yield surface is either linear, exponential or determined by a load curve. In the above, the stress components  $\sigma_{11}$ ,  $\sigma_{22}$  and  $\sigma_{12}$  are with respect to the material coordinate system. The material parameters  $a$ ,  $c$ ,  $h$  and  $p$  are Lankford parameters and can be determined from the Equations 4.16-4.21 [61].

The gradient of the yield surface is denoted as,

$$\frac{\partial f}{\partial \sigma_{ij}}(\sigma_{ij}) = \begin{pmatrix} \frac{\partial f}{\partial \sigma_{11}}(\sigma_{ij}) \\ \frac{\partial f}{\partial \sigma_{22}}(\sigma_{ij}) \\ \frac{\partial f}{\partial \sigma_{12}}(\sigma_{ij}) \\ 0 \\ 0 \end{pmatrix} = \begin{pmatrix} \frac{\partial f}{\partial \sigma_{11}}(\sigma_{11}, \sigma_{22}, \sigma_{12}) \\ \frac{\partial f}{\partial \sigma_{22}}(\sigma_{11}, \sigma_{22}, \sigma_{12}) \\ \frac{\partial f}{\partial \sigma_{12}}(\sigma_{11}, \sigma_{22}, \sigma_{12}) \\ 0 \\ 0 \end{pmatrix} \quad (4.94)$$

where

$$\begin{aligned} \frac{\partial f}{\partial \sigma_{11}}(\sigma_{11}, \sigma_{22}, \sigma_{12}) &= \frac{\partial \bar{\sigma}}{\partial \sigma_{11}}(\sigma_{11}, \sigma_{22}, \sigma_{12}) \\ &= \frac{\bar{\sigma}(\sigma_{11}, \sigma_{22}, \sigma_{12})^{1-m}}{2} \left\{ a(K_1 - K_2)|K_1 - K_2|^{m-2} \left( \frac{1}{2} \right. \right. \\ &\quad \left. \left. - \frac{\sigma_{11} - h\sigma_{22}}{4K_2} \right) + a(K_1 + K_2)|K_1 + K_2|^{m-2} \left( \frac{1}{2} + \frac{\sigma_{11} - h\sigma_{22}}{4K_2} \right) \right. \\ &\quad \left. + c2^m K_2^{m-1} \frac{\sigma_{11} - h\sigma_{22}}{4K_2} \right\} \end{aligned} \quad (4.95)$$

$$\begin{aligned} \frac{\partial f}{\partial \sigma_{12}}(\sigma_{11}, \sigma_{22}, \sigma_{12}) &= \frac{\partial \bar{\sigma}}{\partial \sigma_{12}}(\sigma_{11}, \sigma_{22}, \sigma_{12}) \\ &= \frac{\bar{\sigma}(\sigma_{11}, \sigma_{22}, \sigma_{12})^{1-m}}{2} \frac{p^2\sigma_{12}}{K_2} \left\{ -a(K_1 - K_2)|K_1 - K_2|^{m-2} \right. \\ &\quad \left. + a(K_1 + K_2)|K_1 + K_2|^{m-2} + c2^m K_2^{m-1} \right\} \end{aligned} \quad (4.96)$$

$$\begin{aligned}
\frac{\partial f}{\partial \sigma_{22}}(\sigma_{11}, \sigma_{22}, \sigma_{12}) &= \frac{\partial \bar{\sigma}}{\partial \sigma_{22}}(\sigma_{11}, \sigma_{22}, \sigma_{12}) \\
&= \frac{\bar{\sigma}(\sigma_{11}, \sigma_{22}, \sigma_{12})^{1-m}}{2} h \left\{ a(K_1 - K_2) |K_1 - K_2|^{m-2} \left( \frac{1}{2} \right. \right. \\
&\quad \left. \left. + \frac{\sigma_{11} - h\sigma_{22}}{4K_2} \right) + a(K_1 + K_2) |K_1 + K_2|^{m-2} \left( \frac{1}{2} - \frac{\sigma_{11} - h\sigma_{22}}{4K_2} \right) \right. \\
&\quad \left. + c2^m K_2^{m-1} \frac{\sigma_{11} - h\sigma_{22}}{4K_2} \right\}
\end{aligned} \tag{4.97}$$

For the implementation of three-dimensional formulation, the yield condition is generalized to include the normal stress as follows.

$$\bar{f}(\sigma_{ij}, \bar{\epsilon}^p) = \bar{\sigma}(\sigma_{11} - \sigma_{33}, \sigma_{22} - \sigma_{33}, \sigma_{12}) - \sigma_y(\bar{\epsilon}^p) \leq 0 \tag{4.98}$$

This generalization keeps the convexity of the yield surface and Equation 4.98 reduces to Equation 4.90 for a plane stress. The gradient of the yield surface is for this effective stress determined from [61],

$$\begin{aligned}
\frac{\partial f}{\partial \sigma_{ij}}(\sigma_{ij}) &= \begin{pmatrix} \frac{\partial \bar{f}}{\partial \sigma_{11}}(\sigma_{ij}) \\ \frac{\partial \bar{f}}{\partial \sigma_{22}}(\sigma_{ij}) \\ \frac{\partial \bar{f}}{\partial \sigma_{12}}(\sigma_{ij}) \\ 0 \\ 0 \end{pmatrix} \\
&= \begin{pmatrix} \frac{\partial f}{\partial \sigma_{11}}(\sigma_{11} - \sigma_{33}, \sigma_{22} - \sigma_{33}, \sigma_{12}) \\ -\frac{\partial f}{\partial \sigma_{11}}(\sigma_{11} - \sigma_{33}, \sigma_{22} - \sigma_{33}, \sigma_{12}) - \frac{\partial f}{\partial \sigma_{22}}(\sigma_{11} - \sigma_{33}, \sigma_{22} - \sigma_{33}, \sigma_{12}) \\ \frac{\partial f}{\partial \sigma_{12}}(\sigma_{11} - \sigma_{33}, \sigma_{22} - \sigma_{33}, \sigma_{12}) \\ 0 \\ 0 \end{pmatrix}
\end{aligned} \tag{4.99}$$

The elastic stress-strain relation can be written,

$$\begin{aligned}
d\sigma_{ij} &= \begin{pmatrix} d\sigma_{11} \\ d\sigma_{22} \\ d\sigma_{12} \\ d\sigma_{23} \\ d\sigma_{13} \end{pmatrix} \\
&= \frac{E}{1-\nu^2} \begin{bmatrix} 1 & \nu & 0 & 0 & 0 \\ \nu & 1 & 0 & 0 & 0 \\ 0 & 0 & \frac{1-\nu}{2} & 0 & 0 \\ 0 & 0 & 0 & \frac{1-\nu}{2} & 0 \\ 0 & 0 & 0 & 0 & \frac{1-\nu}{2} \end{bmatrix} \begin{pmatrix} d\varepsilon_{11} - d\varepsilon_{11}^p \\ d\varepsilon_{22} - d\varepsilon_{22}^p \\ 2(d\varepsilon_{12} - d\varepsilon_{12}^p) \\ 2(d\varepsilon_{23} - d\varepsilon_{23}^p) \\ 2(d\varepsilon_{13} - d\varepsilon_{13}^p) \end{pmatrix} \\
&= C_{ijkl}^{ps} (d\varepsilon_{ij} - d\varepsilon_{ij}^p)
\end{aligned} \tag{4.100}$$

Where  $E$  is the Young's modulus,  $\nu$  is the Poisson's ratio and  $C_{ijkl}^{ps}$  denotes the plane stress elastic tangential stiffness matrix. The associative flow rule for the plastic strain rate can be written

$$d\varepsilon_{ij}^p = d\lambda \frac{\partial f}{\partial \sigma_{ij}} \tag{4.101}$$

where  $d\lambda$  is a scalar factor of proportionality. The consistency condition results in

$$\frac{\partial f}{\partial \sigma_{ij}} d\sigma_{ij} + \frac{\partial f}{\partial \bar{\varepsilon}^p} d\bar{\varepsilon}^p = 0 \tag{4.102}$$

For algorithmic consistency, the effective plastic strain rate is defined as  $d\bar{\varepsilon}^p = d\lambda$ . Multiplying Equation 4.100 with  $\partial f / \partial \sigma_{ij}$  and using Equation 4.101 and 4.102 gives

$$d\lambda = \frac{\frac{\partial f}{\partial \sigma_{ij}} C_{ijkl}^{ps} d\varepsilon_{ij}}{\frac{\partial f}{\partial \sigma_{ij}} C_{ijkl}^{ps} - \frac{\partial f}{\partial \bar{\varepsilon}^p}} \tag{4.103}$$

$$d\varepsilon_{ij}^p = \frac{\frac{\partial f}{\partial \sigma_{ij}} C_{ijkl}^{ps} d\varepsilon_{ij}}{\frac{\partial f}{\partial \sigma_{ij}} C_{ijkl}^{ps} \frac{\partial f}{\partial \sigma_{ij}} - \frac{\partial f}{\partial \bar{\varepsilon}^p} \frac{\partial f}{\partial \sigma_{ij}}} \frac{\partial f}{\partial \sigma_{ij}} \quad (4.104)$$

Inserting Equation 4.104 into the Equation 4.100, it is obtained,

$$d\sigma_{ij} = \left( C_{ijkl}^{ps} - \frac{\left\{ C_{ijkl}^{ps} \frac{\partial f}{\partial \sigma_{ij}} \right\} \left\{ C_{ijkl}^{ps} \frac{\partial f}{\partial \sigma_{ij}} \right\}}{\frac{\partial f}{\partial \sigma_{ij}} C_{ijkl}^{ps} \frac{\partial f}{\partial \sigma_{ij}} - \frac{\partial f}{\partial \bar{\varepsilon}^p}} \right) d\varepsilon_{ij} \quad (4.105)$$

#### 4.5.5 Cyclic Elastoplastic Model

The uniaxial stress-strain curve is given in the following form [61];

$$\sigma(\bar{\varepsilon}^p) = \sigma_{y0} + Q_{r1}(1 - e^{(-C_{r1}\bar{\varepsilon}^p)}) + Q_{r2}(1 - e^{(-C_{r2}\bar{\varepsilon}^p)}) \quad (4.106)$$

where the material parameters  $C_{r1}$  and  $C_{r2}$  governs the rate of change of the corresponding kinematic and isotropic hardening variables, whereas  $Q_{r1}$  and  $Q_{r2}$  represents its asymptotic value. The material constants are determined by curve fitting of the experimental curves giving the increase of the peak stress vs. accumulated plastic strain

The quadratic yield function that has been adapted to the cyclic plasticity model is given as:

$$f(\sigma_{ij}, \alpha_{ij}, R) = \frac{1}{2} \bar{\sigma}_k^T P_{kl} \bar{\sigma}_l - \frac{1}{3} K^2 \quad (4.107)$$

where  $P_{kl}$  is a constant and positive semidefinite matrix. The effective stress vector,  $\bar{\sigma}_l$ , is defined by

$$\bar{\sigma}_{kl} = \sigma_{kl} - \alpha_{kl}$$

Where  $\alpha_{kl}$  is the kinematic hardening vector and the radius of the yield surface is represented by  $K = \sigma_{y0} + R$ . Here  $\sigma_{y0}$  is the cyclic yield stress and  $R$  is the isotropic hardening variable. The quadratic yield function contains the von Mises yield

criterion for initially isotropic materials as well as Hill's yield criterion for anisotropic materials. A quadratic yield function is adopted as combined hardening Equation 4.11. With nonlinear evolutionary rules kinematic hardening variable given as,

$$d\alpha_{ij} = \frac{2}{3} C_{\alpha_{ij}} (Q_{\alpha_{ij}} \bar{\sigma}_{kl} - K \alpha_{ij}) d\lambda \quad (4.108)$$

and the evolutionary equation of isotropic hardening variable,

$$dR = \frac{2}{3} C_R (Q_R \bar{\sigma}_{kl} - R) K d\lambda \quad (4.109)$$

Finally the loading-unloading conditions are expressed in terms of the yield function and the plastic parameter as follows

$$f(\sigma_{ij}, \alpha_{ij}, R) \leq 0 \quad d\lambda \geq 0 \quad d\lambda f(\sigma_{ij}, \alpha_{ij}, R) = 0 \quad (4.110)$$

Integration of Equations 4.106 and 4.107 leads to

$$R = Q_R (1 - e^{(-C_R \bar{\epsilon}^p)}) \quad (4.111)$$

$$\alpha_{ij} = Q_{\alpha_{ij}} \left( 1 - e^{(-C_{\alpha_{ij}} \bar{\epsilon}^p)} \right) \quad (4.112)$$

#### 4.5.6 Hill'48

These constitutive models based on the Hill 1948 anisotropic yield function. Based on the associated flow rule, the plastic strain rates  $d\epsilon_x^p$ ,  $d\epsilon_y^p$ ,  $d\epsilon_z^p$ ,  $d\epsilon_{xy}^p$ ,  $d\epsilon_{yz}^p$  and  $d\epsilon_{xz}^p$  can be obtained as

$$d\epsilon_x^p = d\lambda \frac{\partial f}{\partial \sigma_x} = d\lambda [2H(\sigma_x - \sigma_y) - 2G(\sigma_z - \sigma_x)] \quad (4.113)$$

$$d\epsilon_y^p = d\lambda \frac{\partial f}{\partial \sigma_y} = d\lambda [-2H(\sigma_x - \sigma_y) + 2F(\sigma_y - \sigma_z)] \quad (4.114)$$

$$d\epsilon_z^p = d\lambda \frac{\partial f}{\partial \sigma_z} = d\lambda [-2F(\sigma_y - \sigma_z) + 2G(\sigma_z - \sigma_x)] \quad (4.115)$$

$$d\varepsilon_{xy}^p = d\lambda \frac{\partial f}{\partial \sigma_x} = d\lambda [2N\tau_{xy}] \quad (4.116)$$

$$d\varepsilon_{yz}^p = d\lambda \frac{\partial f}{\partial \sigma_x} = d\lambda [2L\tau_{yz}] \quad (4.117)$$

$$d\varepsilon_{xz}^p = d\lambda \frac{\partial f}{\partial \sigma_x} = d\lambda [2M\tau_{xz}] \quad (4.118)$$

In terms of the r-values anisotropy parameters can be found as,

$$r_0 = \frac{d\varepsilon_y^p}{d\varepsilon_z^p} = \frac{H}{G} \quad r_{90} = \frac{d\varepsilon_x^p}{d\varepsilon_z^p} = \frac{H}{F} \quad (4.119a)$$

$$r_{45} = \frac{d\varepsilon_y^p}{d\varepsilon_z^p} = \frac{2N - (F + G)}{2(F + G)} \quad G + H = 1 \quad (4.119b)$$

Yield function becomes,

$$f = \frac{1}{1 + r_0} \left[ \frac{r_0}{r_{90}} (\sigma_y - \sigma_z)^2 + r_0 (\sigma_z - \sigma_x)^2 + \frac{(2r_{45} + 1)(r_0 + r_{90})}{r_{90}} (\tau_{xy} + \tau_{zx} + \tau_{yz}) \right] - \bar{\sigma}^2 = 0 \quad (4.120)$$

## CHAPTER 5

### RESULTS

#### 5.1 Introduction

In this chapter, the results of the numerical simulations that have been performed for cylindrical cup drawing, square cup drawing and V-bending are presented to compare the effects of constitutive models on forming operations. In all of the simulations; elastic plastic constitutive model with isotropic hardening, elastic plastic constitutive model with kinematic hardening, elastic plastic constitutive model with combined hardening, power law isotropic plasticity, piecewise linear isotropic plasticity, three-parameter Barlat, cyclic elastoplastic and Hill'48. [61] models are applied by using the finite element code LS-DYNA.

The thickness strain and effective stress distributions, and the deformed geometry have been obtained for cylindrical and square cup drawing by numerical analysis. The strain distributions are compared with the analytical results in cylindrical cup drawing, whereas the deformed shapes are compared with the experiments in square cup drawing. For V-bending the numerical and experimental results are compared for using the springback amounts.

Three different materials are used in the studies, St12 steel, stainless steel 409 Ni and Al-5182 aluminum. The mechanical properties of the materials are given in Table 5.1 and the stress strain curves obtained from simple tension test are shown in Figure 5.1 [74].

Table 5.1 Mechanical Properties of Used Materials

	Density [kg/m <sup>3</sup> ]	Elastic Modulus [MPa]	Poisson Ratio ( $\nu$ )	Hardening Parameter (n)	Hardening Coefficient (K)	Coefficients of Anisotropy (r-values)		
						$r_0$	$r_{45}$	$r_{90}$
<b>St12 Steel</b>	7850	207000	0.28	0.22	648	1.13	0.95	1.35
<b>Stainless Steel 409 Ni</b>	7850	207000	0.28	0.17	749	1.1	1.1	1.1
<b>Al-5182 Aluminum</b>	2700	69000	0.33	0.279	558.4	0.85	0.77	0.9

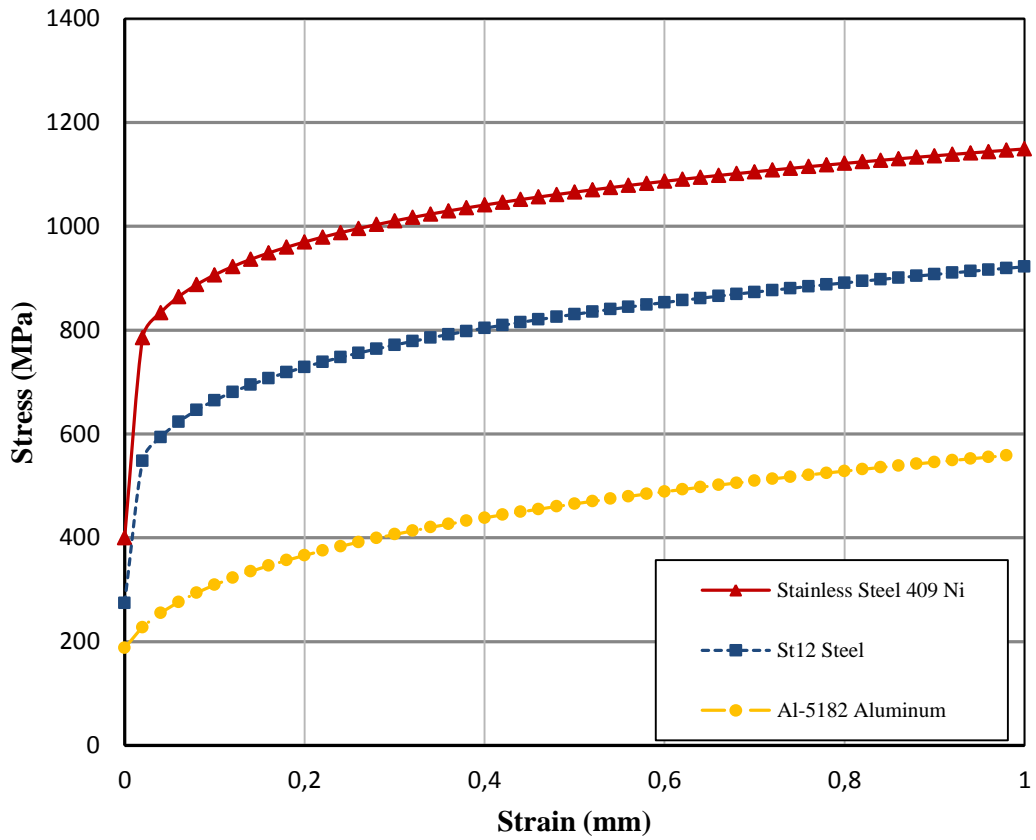


Figure 5.1: True stress vs. true strain curve for the used materials.

## 5.2 Cylindrical Cup Drawing

In this section, the numerical simulation results of cylindrical cup drawing are presented for St12 steel. The process variables used in the cylindrical cup drawing simulations and analytical calculations are as follows;

Diameter of a Blank	<i>81 mm</i>
Punch diameter	<i>50 mm</i>
Die diameter	<i>100 mm</i>
Die opening diameter	<i>54 mm</i>
Die shoulder diameter	<i>4.5 mm</i>
Coulomb coefficient of friction	$\mu = 0.125$
Blank holding force	<i>5000 N</i>
Tangent modulus ( $E_t$ )	<i>1000 MPa</i>

In the present analysis, the blank holder force is applied to the nodes located at the outer rim of the flange. The dimensions of the die, the punch and the blank holder used in cylindrical cup drawing process are shown in Figure 5.2. The model that is used in the simulations is shown in Figure 5.3.

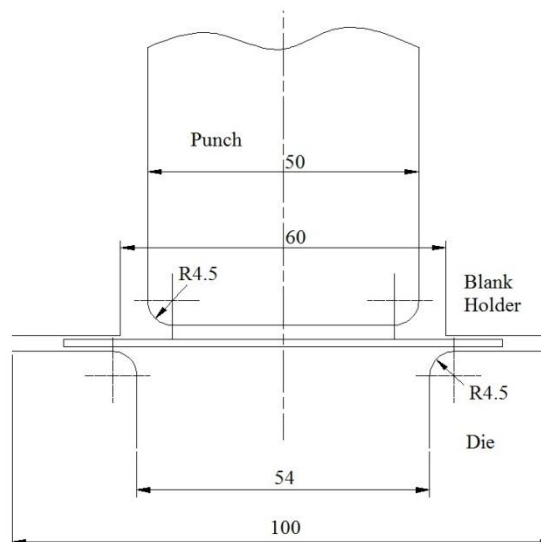


Figure 5.2: Dimensions of the die, blank holder and punch used in cylindrical cup drawing.

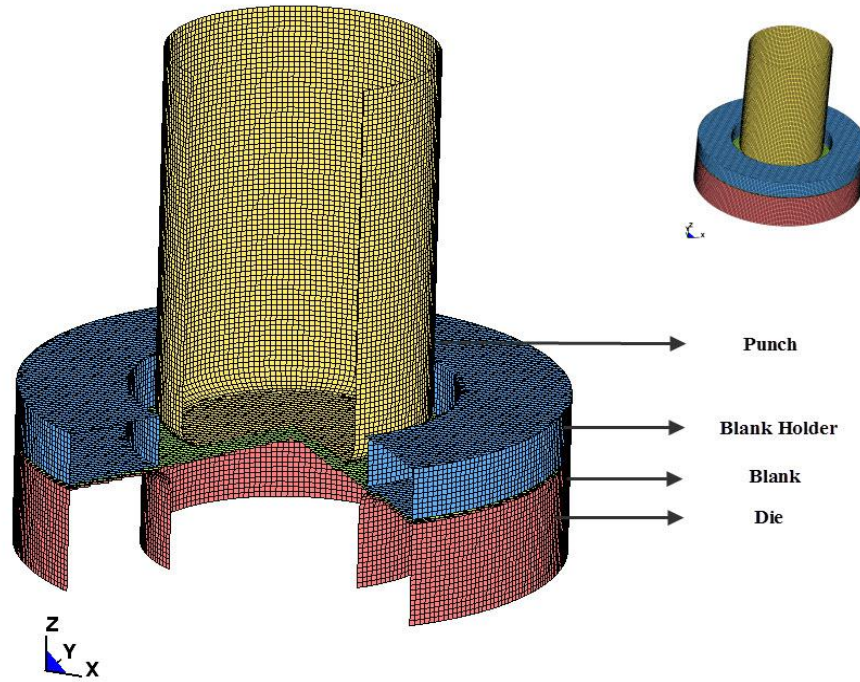


Figure 5.3: FEM model used in cylindrical cup drawing.

The blank is modeled by using 4 node shell elements. Fully integrated shell element formulation [64] is used for the blank. The punch, the die and the blank holder are defined as rigid parts in the simulations. There are 52014 elements in the above model.

In order to compare the thickness strain and effective stress distributions obtained by the numerical simulations and analytical solutions, an infinitesimal element is taken and the equilibrium equations are obtained as follows [74];

$$\frac{d}{dr}(t\sigma_r') = \frac{t}{r}(\sigma_\theta - \sigma_r') \quad (5.1)$$

where  $t$  is thickness,  $r$  is current radius,  $\sigma_r'$  is frictionless radial drawing stress and  $\sigma_\theta$  is tangential stress. The yield criterion can be written as,

$$\sigma_\theta - \sigma_r' = m\bar{\sigma} \quad (5.2)$$

where  $m$  taken as 1.1 which can be defined as the optimum agreement between Tresca and von Mises yield functions. Neglecting the thickness difference across the flange equilibrium equation becomes,

$$d\sigma_r' = -m\bar{\sigma} \frac{dr}{r} \quad (5.3)$$

Introducing power law hardening

$$\bar{\sigma} = \bar{\sigma}_{y0} + K(\varepsilon)^n \quad (5.4)$$

Equation 5.4 can be expressed [74],

$$\bar{\sigma} = \bar{\sigma}_{y0} + K \left( \ln \frac{R}{r} \right)^n \quad (5.5)$$

$\ln R/r$  is the hoop strain. From Figure 5.4, if  $t_m$  is the current mean thickness between the rim and element under consideration,  $R$  is the initial and  $r$  the current radius of a particle, the incompressibility condition gives

$$\pi(R_0^2 - R^2)t_0 = \pi(r_0^2 - r^2)t_m \quad (5.6)$$

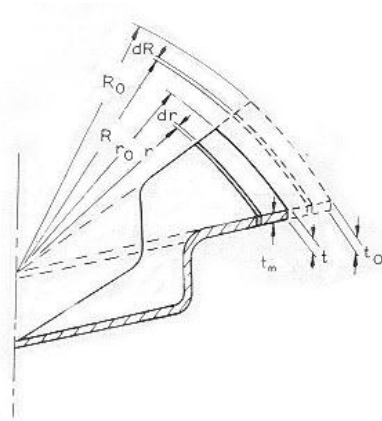


Figure 5.4: Section of partially drawn cup in cylindrical cup drawing [74].

The hoop strain can be written as,

$$\ln \frac{R}{r} = \frac{1}{2} \ln \left\{ \frac{t_m}{t_0} \left( 1 + \frac{y}{r^2} \right) \right\} \quad (5.7)$$

where  $y = \left( R_0^2 \frac{t_m}{t_0} - r_0^2 \right)$ . Substituting into Equation 5.5 we get [74],

$$\bar{\sigma} = \bar{\sigma}_{y0} + K \left[ \frac{1}{2} \ln \left\{ \frac{t_m}{t_0} \left( 1 + \frac{y}{r^2} \right) \right\} \right]^n \quad (5.8)$$

If this equation substituted into equilibrium equation and integrated over current radius  $r$ , radial drawing stress becomes,

$$\sigma_r' = -m\bar{\sigma}_0 \ln \frac{r}{r_0} - mK \int_{r_0}^r \left[ \frac{1}{2} \ln \left\{ \frac{t_m}{t_0} \left( 1 + \frac{y}{r^2} \right) \right\} \right]^n \frac{dr}{r} \quad (5.9)$$

where  $r_0$  is the current radius of the rim. Taking  $H$  as the total blank holding force, the portion of drawing stress due to blank holding friction can be calculated as,

$$\sigma_r'' = \frac{\mu H}{\pi r_0 t} \quad (5.10)$$

then the total radial drawing force becomes,

$$\sigma_r = \sigma_r' + \sigma_r'' \quad (5.11)$$

After finding the radial stress, the tangential stress can be found by using the Equations 5.2 and 5.8. Once the stresses are known, the strains can be obtained from Levy-Misses relations taking  $\sigma_z$  as zero. Thus [74],

$$\varepsilon_z = \frac{dt}{t} = - \left( 2 + \frac{3m\bar{\sigma}}{\sigma_r - 2m\bar{\sigma}} \right) \frac{dr}{r} \quad (5.12)$$

$$r = \left( r_0^2 - y \frac{t_0}{t_m} \right)^{1/2} \quad (5.13)$$

If values of  $\sigma_r'$  and  $\bar{\sigma}$  are substituted into Equation 5.12 it is possible to trace the thickness change of any particular element by numerical integration. The values of the stresses and strains can be approximated by the method of successive improvement.

In Figures 5.5 and 5.6 the effective stress and thickness strain distributions that are obtained by the solution of Equations 5.1-5.13 are compared with numerical simulation results for eight constitutive models.

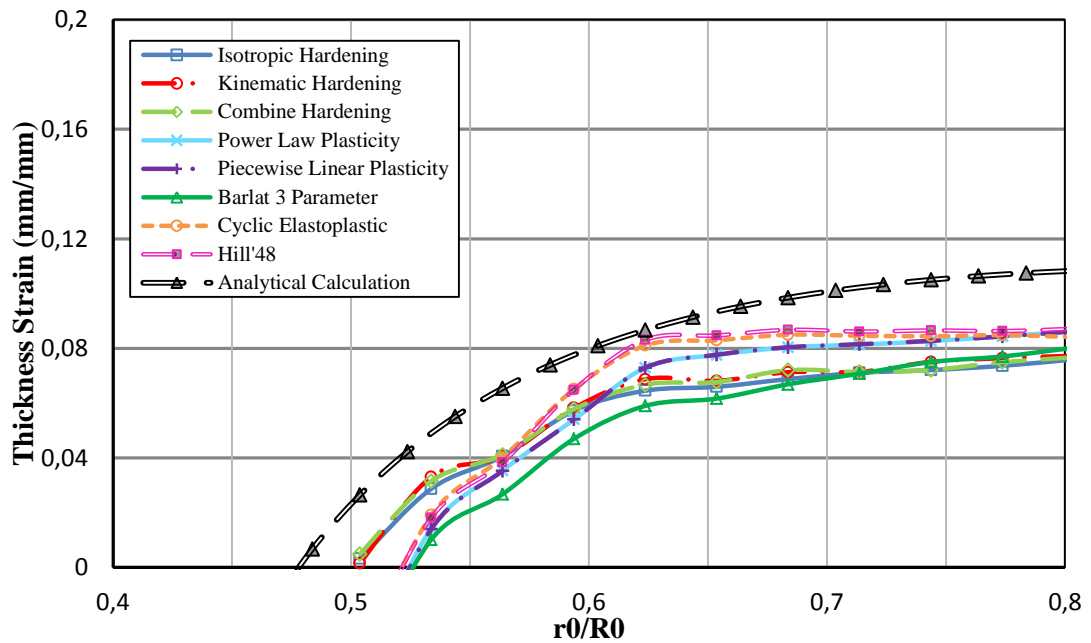


Figure 5.5: Thickness strain distributions in cylindrical cup drawing.

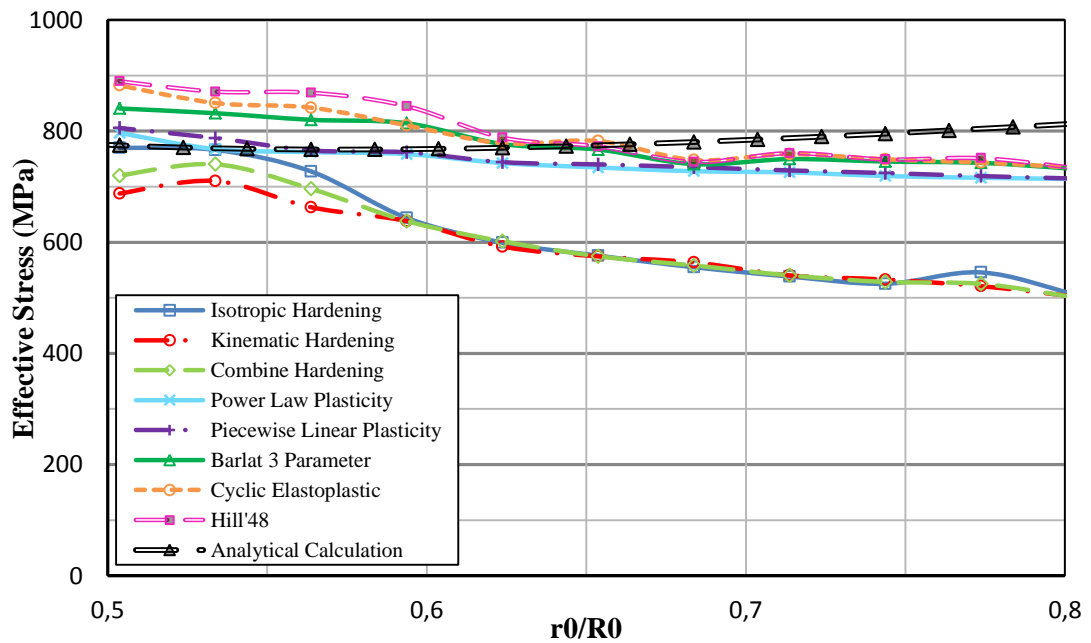


Figure 5.6: Effective stress distributions in cylindrical cup drawing.

### 5.3 Square Cup Drawing

In this section, deep drawing of a square cup from a square blank is analyzed and the corresponding experiments are carried out. The process variables used in the square cup drawing experiments and simulations are as follows;

Dimension of a Blank	<i>80 mm x 80 mm</i>
Dimension of the Punch	<i>40 mm x 40 mm</i>
Punch radius	<i>10 mm</i>
Punch corner radius	<i>4.50 mm</i>
Die opening	<i>42 mm x 42 mm</i>
Die shoulder radius	<i>4.50 mm</i>
Coulomb coefficient of friction	$\mu = 0.125$

Figure 5.7 shows the dimensions of the die, punch and blank holder used in square cup deep drawing process.

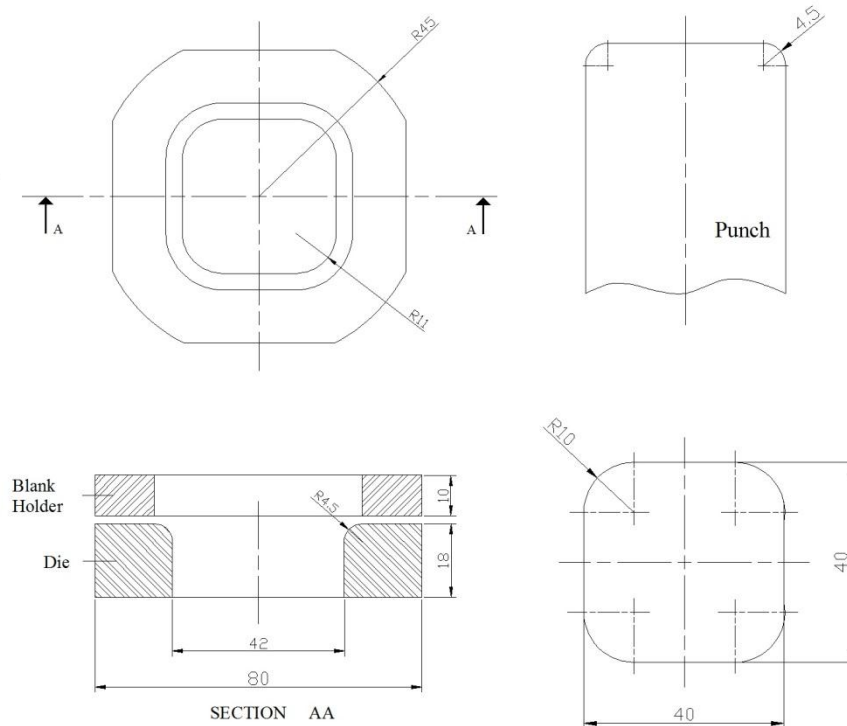


Figure 5.7: Dimensions of the die, blank holder and punch used in square cup deep drawing.

In the deep drawing analyses of the square cup, the tools and the blank are modeled as shown in Figure 5.8.

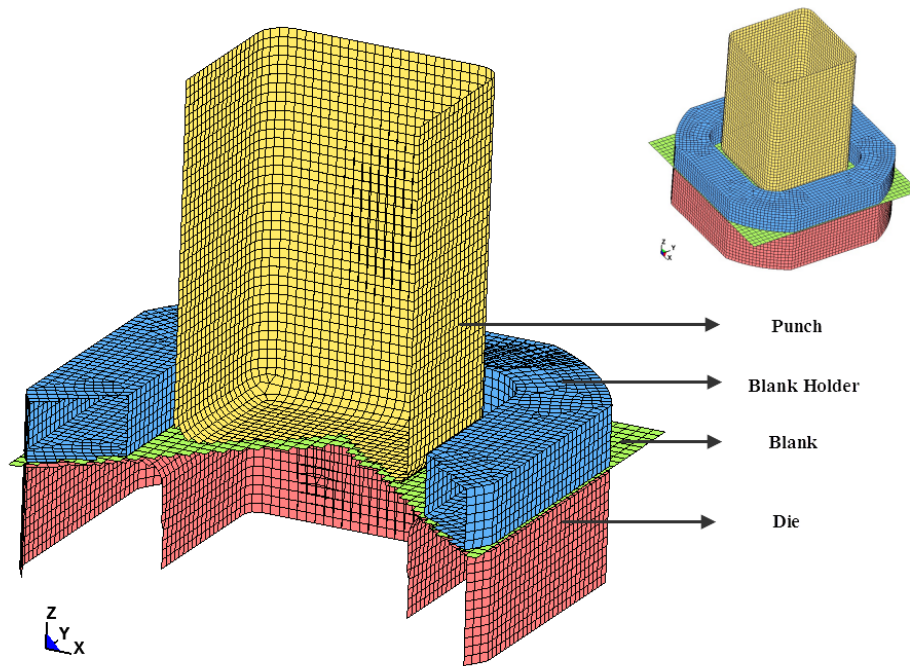


Figure 5.8: FEM model of square cup drawing.

In order to model the blank, 4 node shell elements are used. Fully integrated shell element formulation [64], which enhances in-plane bending behavior, is used for the blank. The punch, the die and the blank holder are defined as rigid parts in the simulations. There are 16569 elements in the above model, however number of elements increase due to adaptive remeshing as deformation increase to get accurate results.

The deep drawing process is modeled in two stages. First, the blank holder has been displaced and the blank compressed between the blank holder and lower die. After the blank holding force is applied, the punch is drawn against the blank and deep drawing operation takes place.

The analyses are performed by using three different materials, St12 steel, stainless steel 409 Ni and Al-5182 aluminum by considering 2 kN, 4 kN and 5 kN blank holder forces. The numerical simulations are carried out for all these three sheet

metal specimens, for 10 mm, 15 mm, 20 mm and 25 mm punch travels. However, experimental results are only performed by using St12 sheet metal specimen, for the same punch travels. During experiment, the blank holding force was held constant and grease was used as the lubricant between the die and sheet metal.

In Figures 5.9-5.16, the simulation results of square cup drawing for two constitutive models; elastic plastic constitutive model with combined hardening and power law isotropic plasticity by using St12 steel are given as an illustration for 20 mm and 25 mm punch travels under 5 kN blank holder force. In Figures 5.9 and 5.10, the thickness strain and effective stress distributions for elastic plastic constitutive model with combined hardening model are shown for 20 mm punch travel. In Figures 5.11 and 5.12, the thickness strain and effective stress distributions for the same constitutive model are shown for 25 mm punch travel.

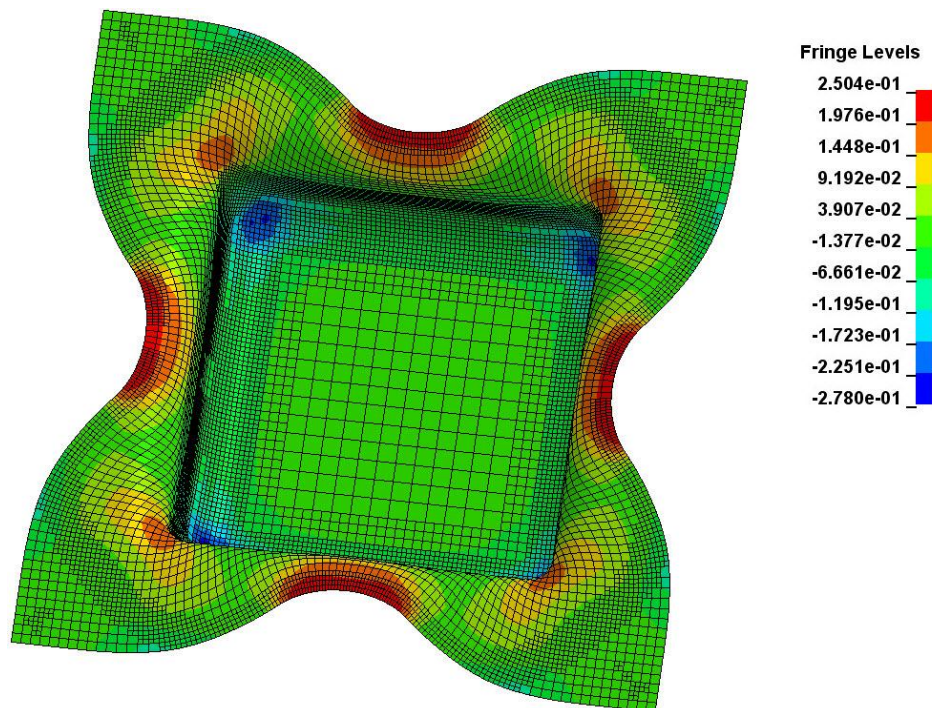


Figure 5.9: Thickness strain distribution of elastic plastic constitutive model with combined hardening for punch travel of 20 mm.

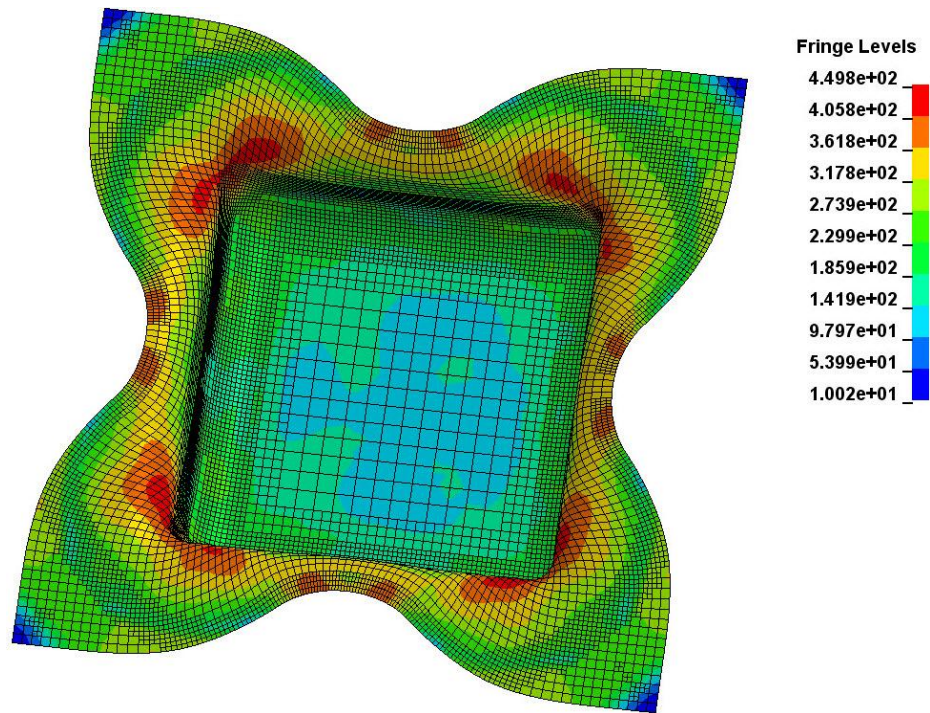


Figure 5.10: Effective stress distribution of elastic plastic constitutive model with combined hardening for punch travel of 20 mm.

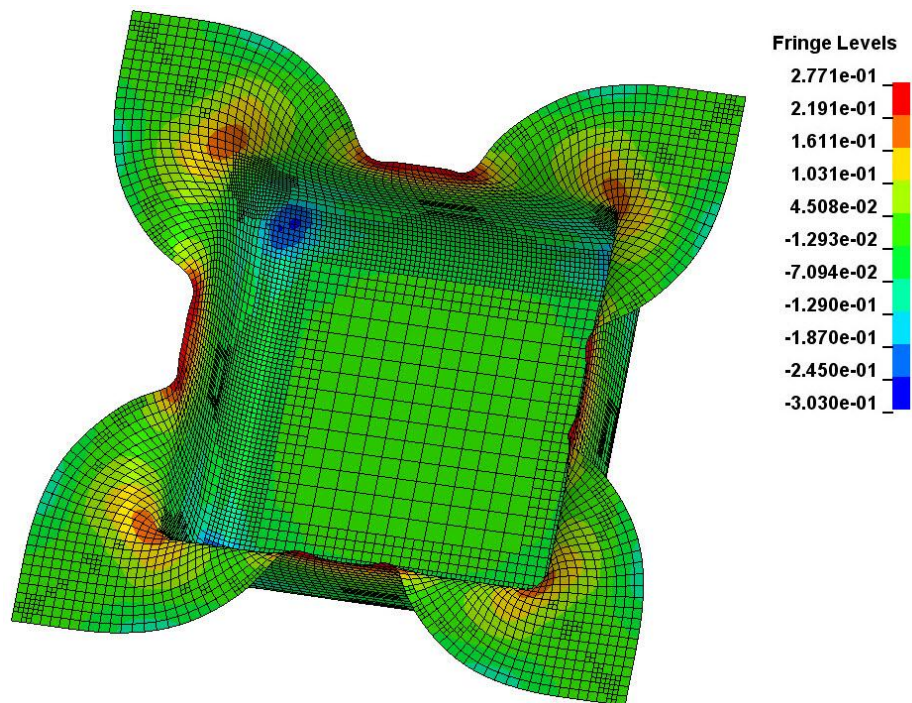


Figure 5.11: Thickness strain distribution of elastic plastic constitutive model with combined hardening for punch travel of 25 mm.

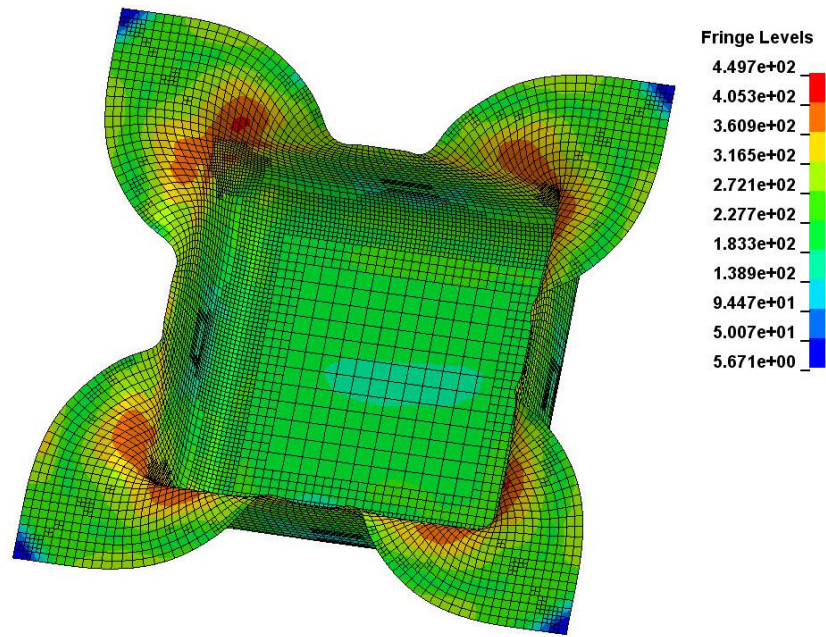


Figure 5.12: Effective stress distribution of elastic plastic constitutive model with combined hardening for punch travel of 25 mm.

In Figures 5.13 and 5.14, the thickness strain and effective stress distributions for power law isotropic plasticity model are shown for 20 mm punch travel.

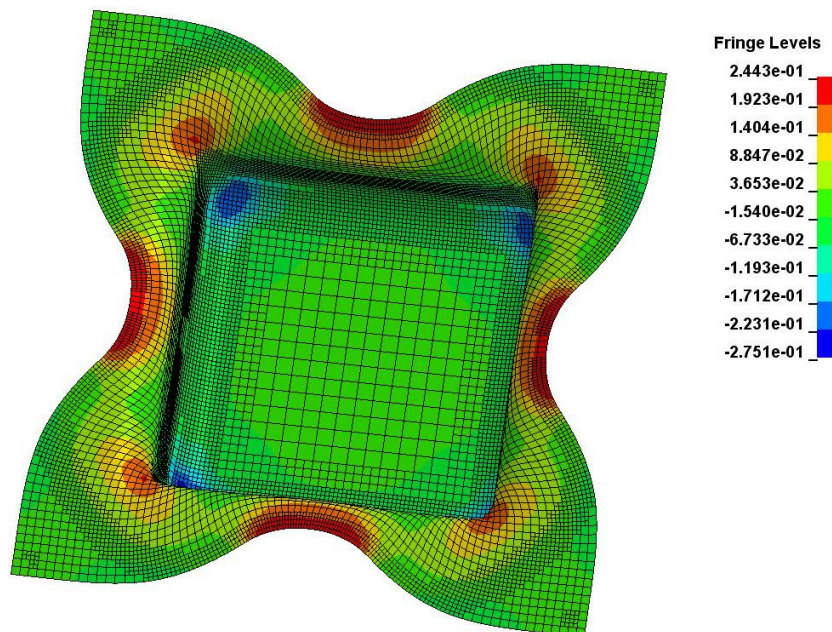


Figure 5.13: Thickness strain distribution of power law isotropic plasticity for punch travel of 20 mm.

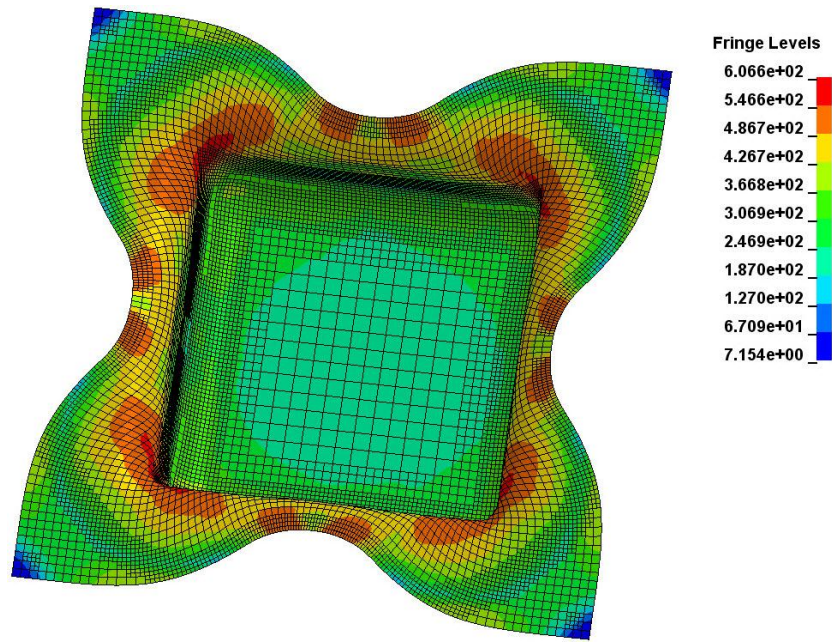


Figure 5.14: Effective stress distribution of power law plasticity for punch travel of 20 mm.

In Figures 5.15 and 5.16, the thickness strain and effective stress distributions for the same constitutive model are shown for 25 mm punch travel.

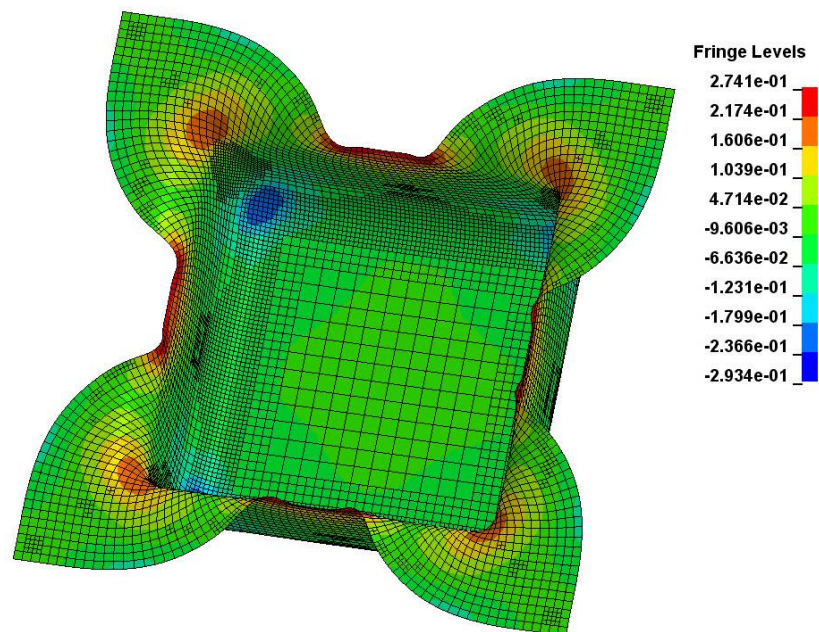


Figure 5.15: Thickness strain distribution of power law isotropic plasticity for punch travel of 25 mm.

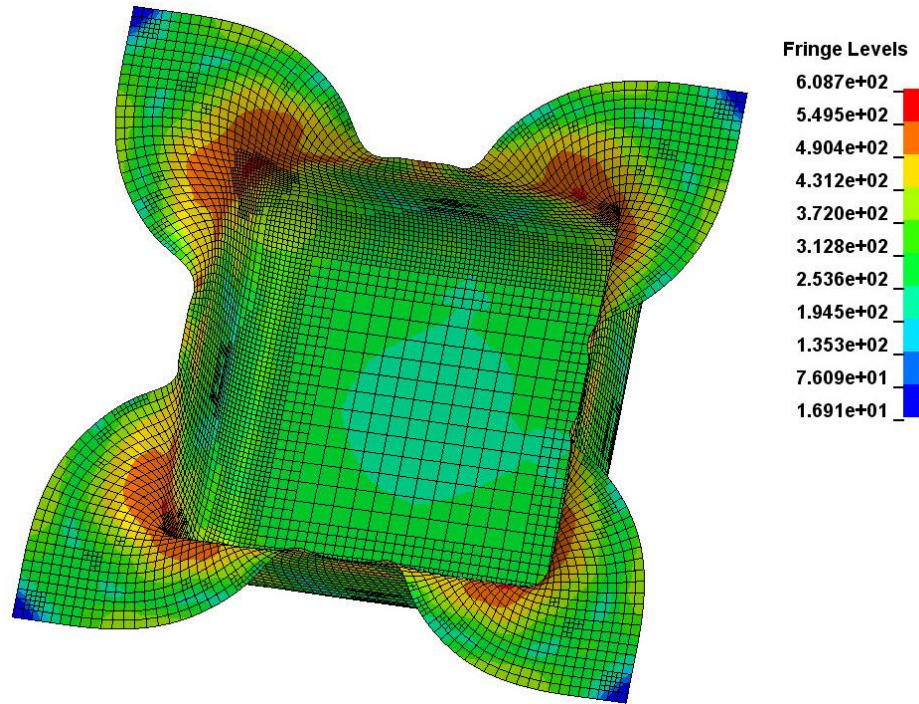


Figure 5.16: Effective stress distribution of power law isotropic plasticity for punch travel of 25 mm.

In this section, the comparison of thickness strain and effective stress distributions are given by using three materials; stainless steel 409 Ni, Al-5182 aluminum and St12 steel. Also, the comparison of edge contour is given by using St12 steel for three different blank holder forces.

### 5.3.1 Stainless Steel 409 Ni

In this section, the simulations are performed by using stainless steel 409 Ni. Figures 5.17-5.32 show the thickness strain and effective stress distributions of square cup drawing, in the diagonal and transverse directions for four different punch displacements; 10 mm, 15 mm, 20 mm and 25 mm respectively by considering 5 kN blank holder force.

Figures 5.17 and 5.18 show the thickness strain and effective stress distributions of square cup drawing, respectively, in diagonal direction for 10 mm punch displacement.

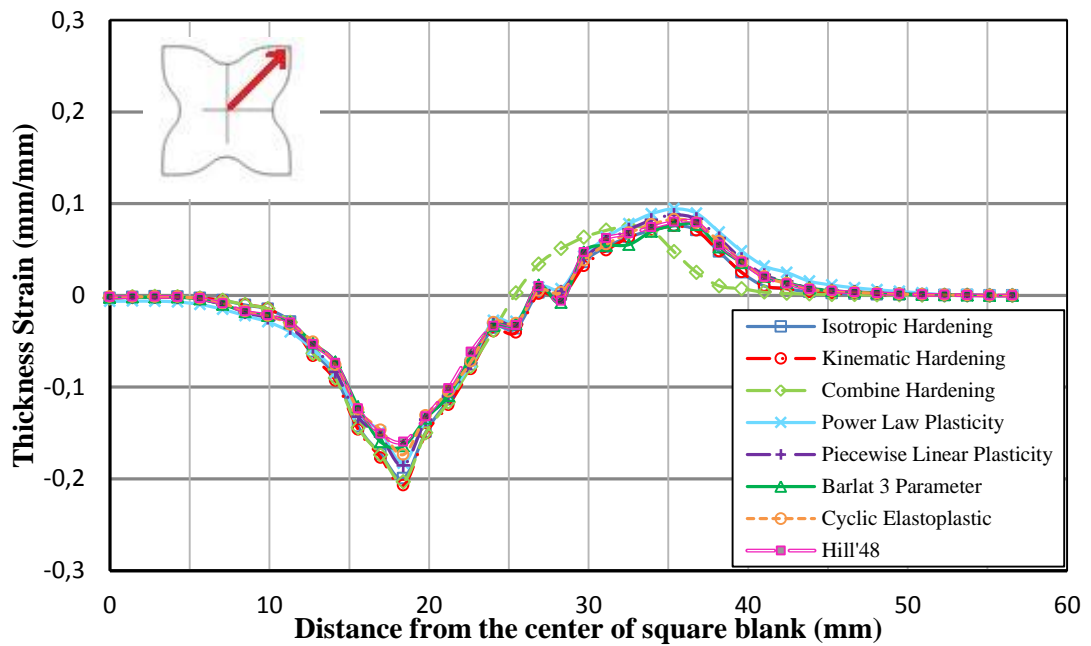


Figure 5.17: Comparison of the thickness strain distributions obtained for different models for 10 mm punch travel (Stainless steel 409 Ni, diagonal direction).

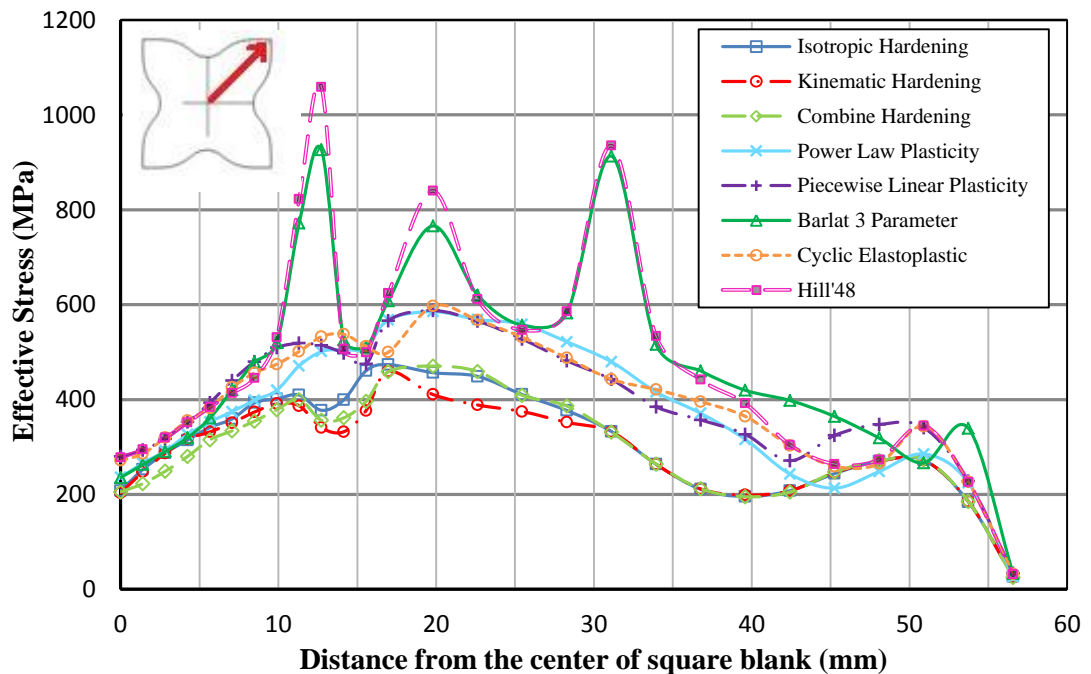


Figure 5.18: Comparison of the effective stress distributions obtained for different models for 10 mm punch travel (Stainless steel 409 Ni, diagonal direction).

In Figures 5.19 and 5.20, the thickness strain and the effective stress distributions of square cup drawing are given, respectively, in transverse direction for 10 mm punch displacement.

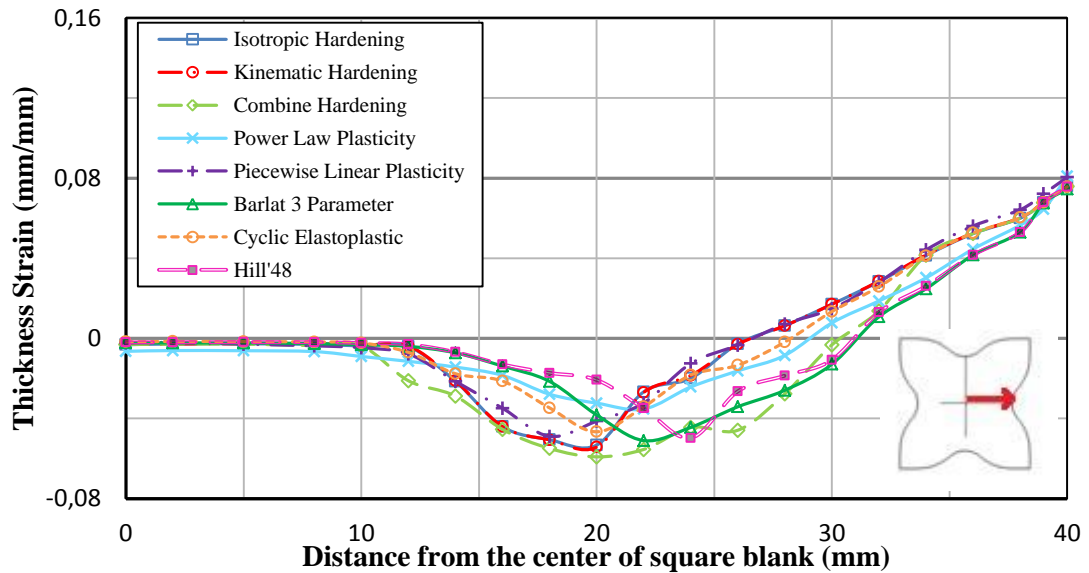


Figure 5.19: Comparison of the thickness strain distributions obtained for different models for 10 mm punch travel (Stainless steel 409 Ni, transverse direction).

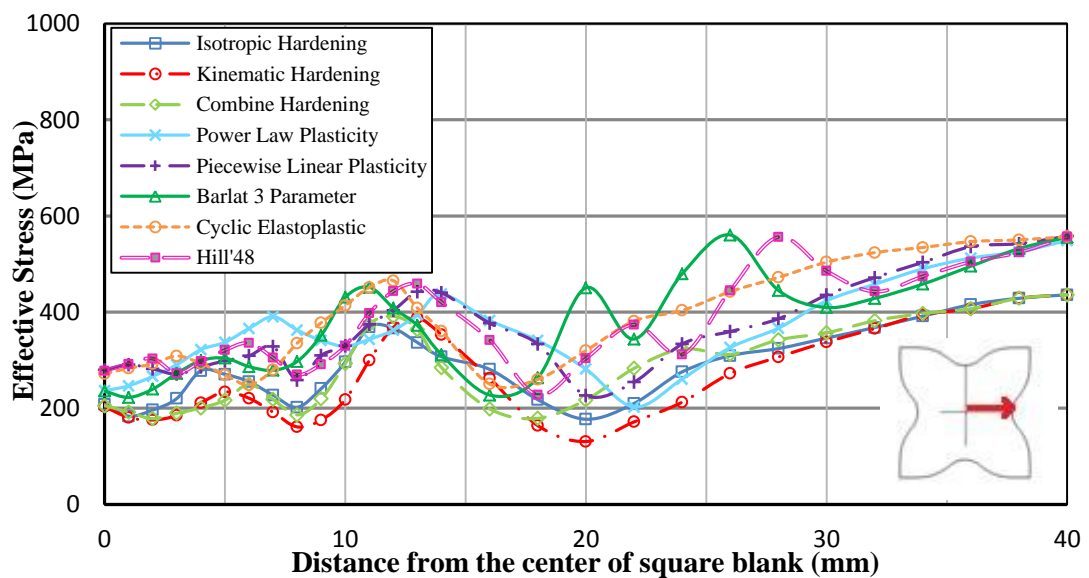


Figure 5.20: Comparison of the effective stress distributions obtained for different models for 10 mm punch travel (Stainless steel 409 Ni, transverse direction).

Figures 5.21 and 5.22 show the thickness strain and the effective stress distributions of square cup drawing, respectively, in diagonal direction for 15 mm punch displacement.

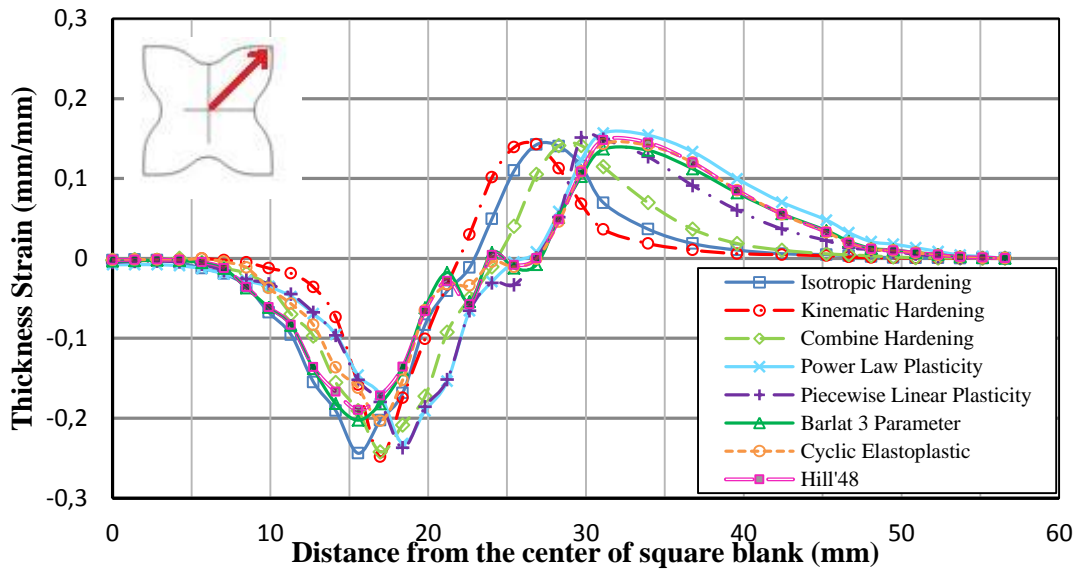


Figure 5.21: Comparison of the thickness strain distributions obtained for different models for 15 mm punch travel (Stainless steel 409 Ni, diagonal direction).

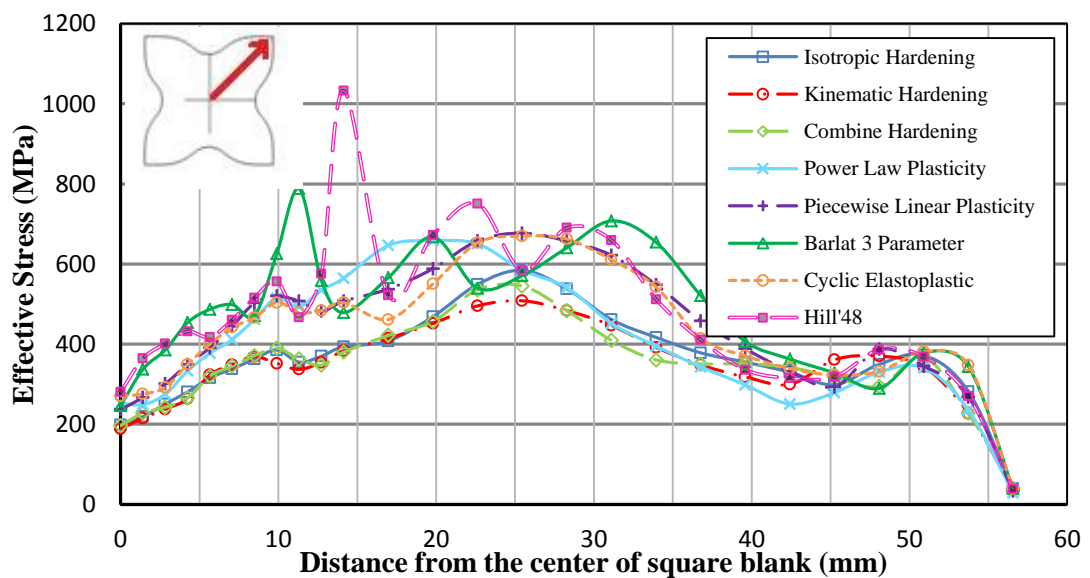


Figure 5.22: Comparison of the effective stress distributions obtained for different models for 15 mm punch travel (Stainless steel 409 Ni, diagonal direction).

In Figures 5.23 and 5.24, the thickness strain and the effective stress distributions of square cup drawing are given, respectively, in transverse direction for 15 mm punch displacement.

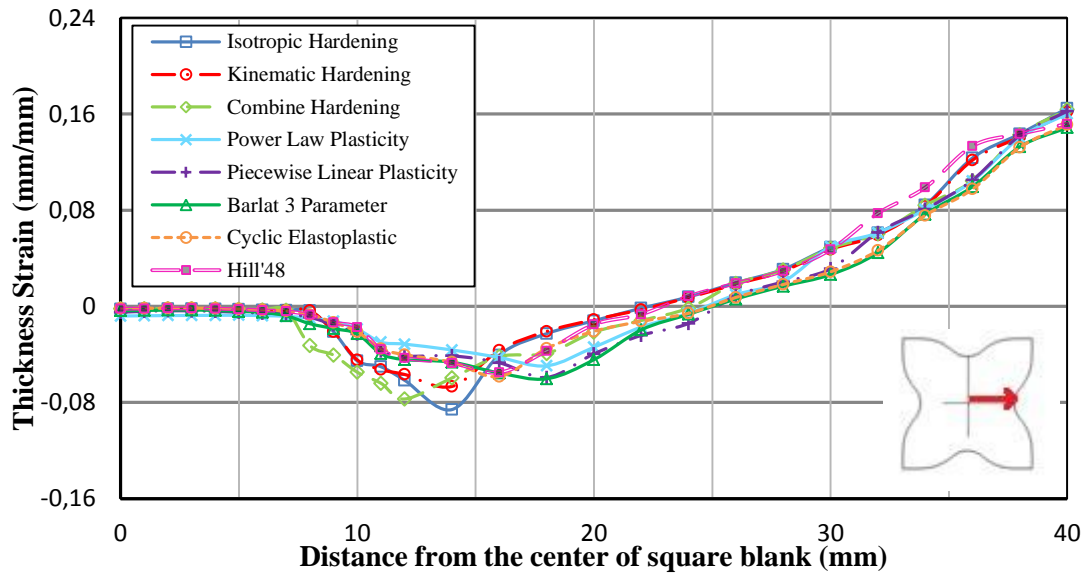


Figure 5.23: Comparison of the thickness strain distributions obtained for different models for 15 mm punch travel (Stainless steel 409 Ni, transverse direction).

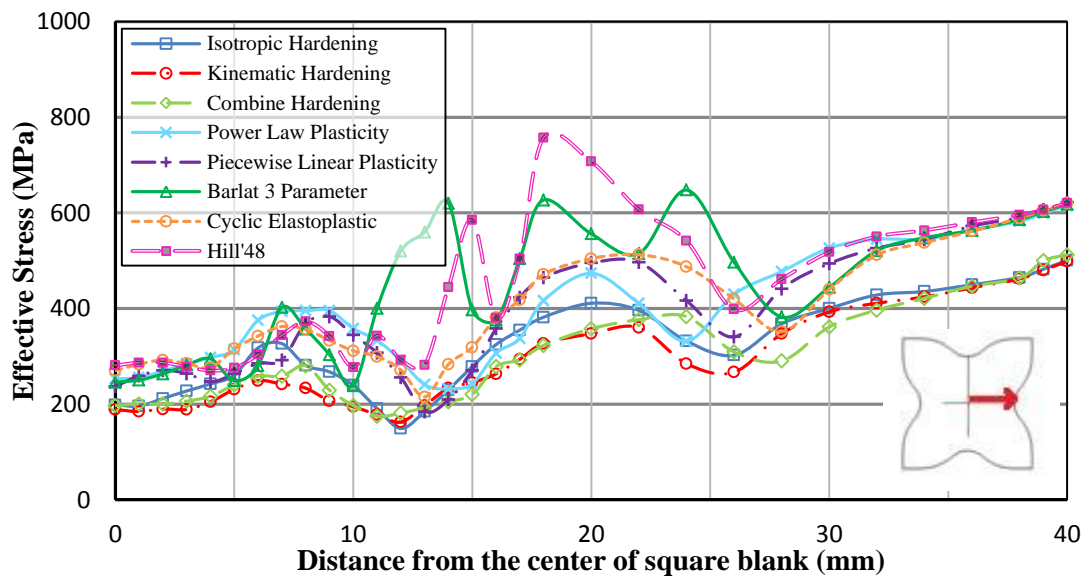


Figure 5.24: Comparison of the effective stress distributions obtained for different models for 15 mm punch travel (Stainless steel 409 Ni, transverse direction).

Figures 5.25 and 5.26 show the thickness strain and the effective stress distributions of square cup drawing, respectively, in diagonal direction for 20 mm punch displacement.

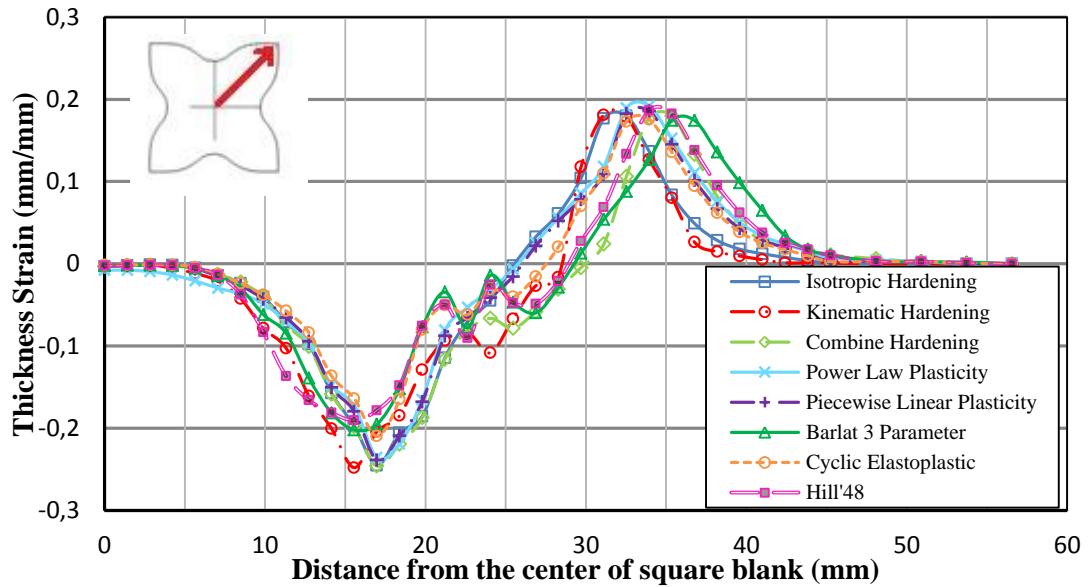


Figure 5.25: Comparison of the thickness strain distributions obtained for different models for 20 mm punch travel (Stainless steel 409 Ni, diagonal direction).

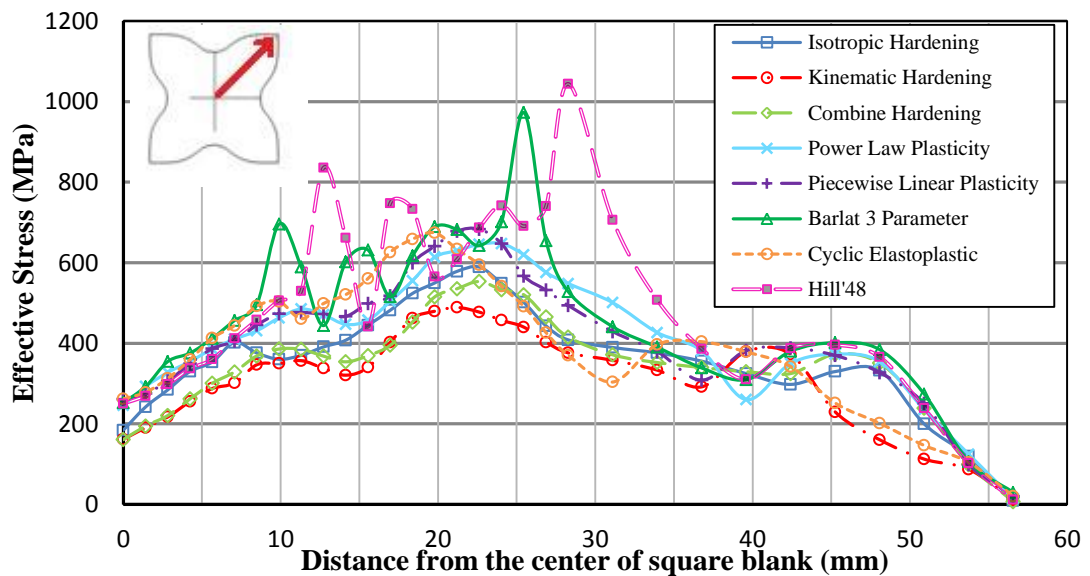


Figure 5.26: Comparison of the effective stress distributions obtained for different models for 20 mm punch travel (Stainless steel 409 Ni, diagonal direction).

In Figures 5.27 and 5.28, the thickness strain and the effective stress distributions of square cup drawing are given, respectively, in transverse direction for 20 mm punch displacement.

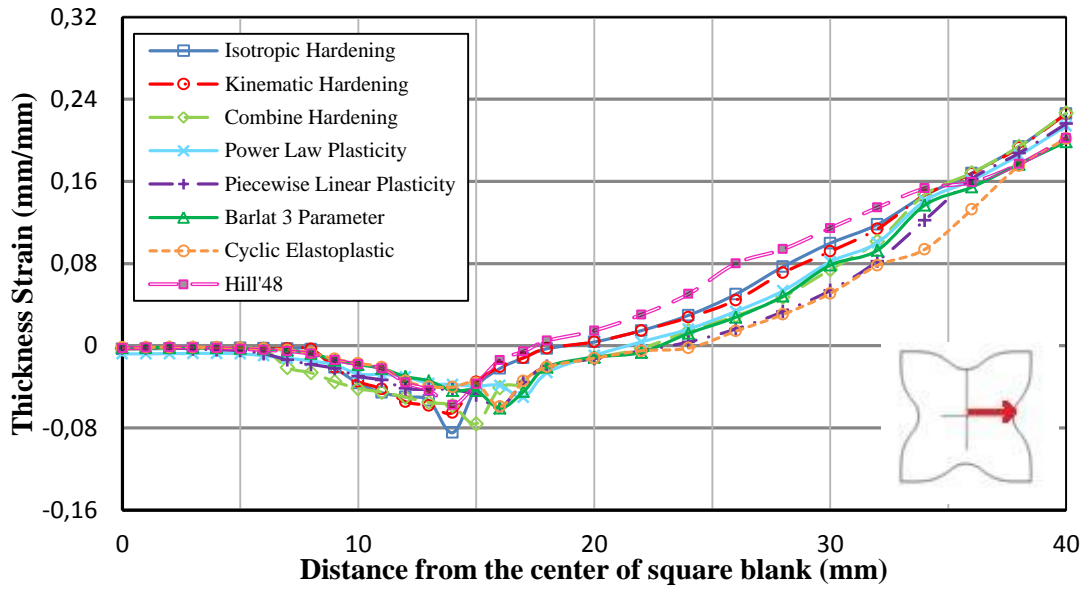


Figure 5.27: Comparison of the thickness strain distributions obtained for different models for 20 mm punch travel (Stainless steel 409 Ni, transverse direction).

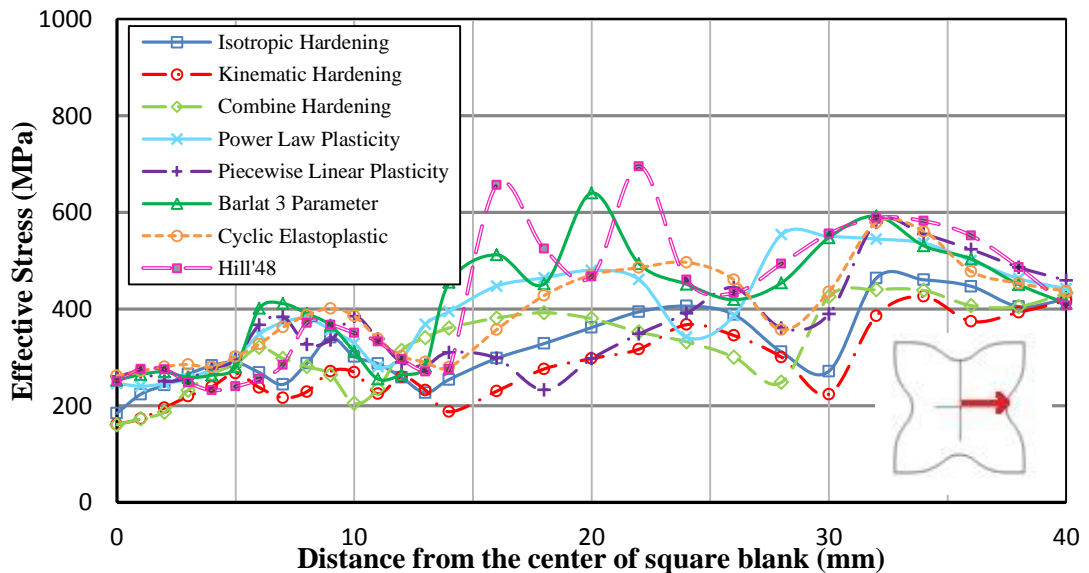


Figure 5.28: Comparison of the effective stress distributions obtained for different models for 20 mm punch travel (Stainless steel 409 Ni, transverse direction).

Figures 5.29 and 5.30 show the thickness strain and the effective stress distributions of square cup drawing, respectively, in diagonal direction for 25 mm punch displacement.

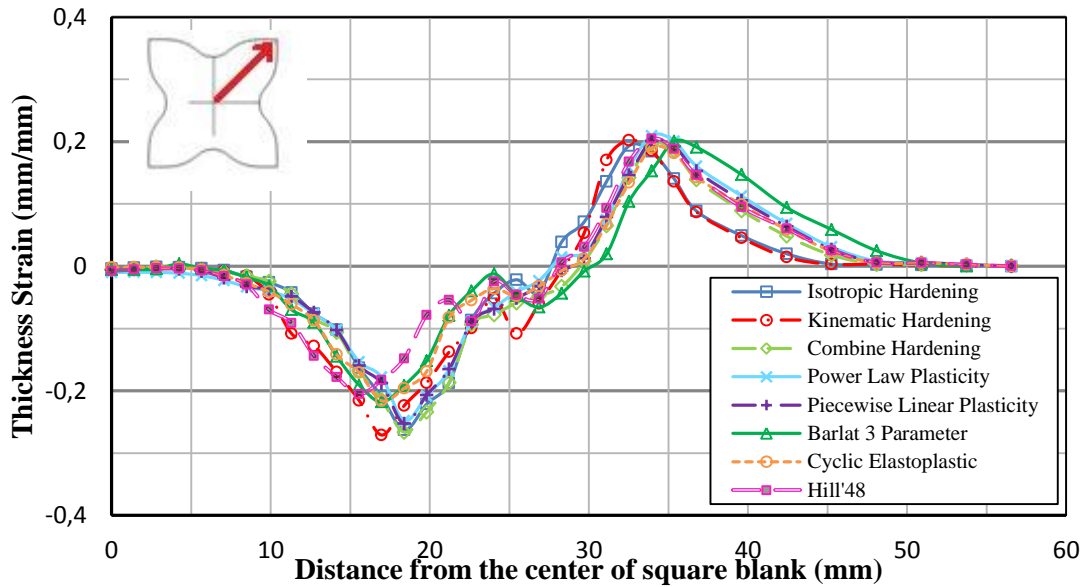


Figure 5.29: Comparison of the thickness strain distributions obtained for different models for 25 mm punch travel (Stainless steel 409 Ni, diagonal direction).

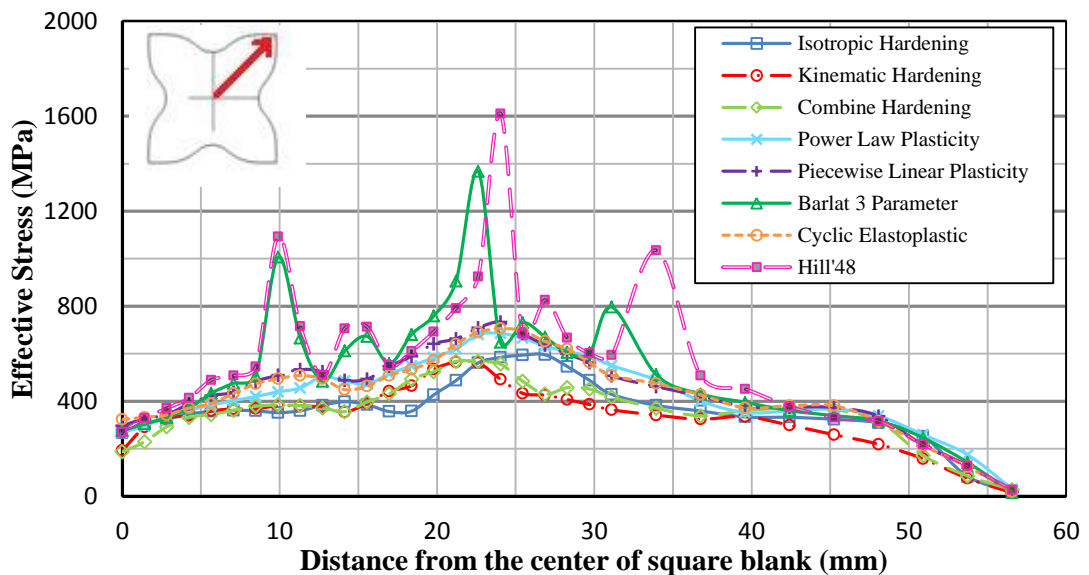


Figure 5.30: Comparison of the effective stress distributions obtained for different models for 25 mm punch travel (Stainless steel 409 Ni, diagonal direction).

In Figures 5.31 and 5.32, the thickness strain and the effective stress distributions of square cup drawing are given, respectively, in transverse direction for 25 mm punch displacement.

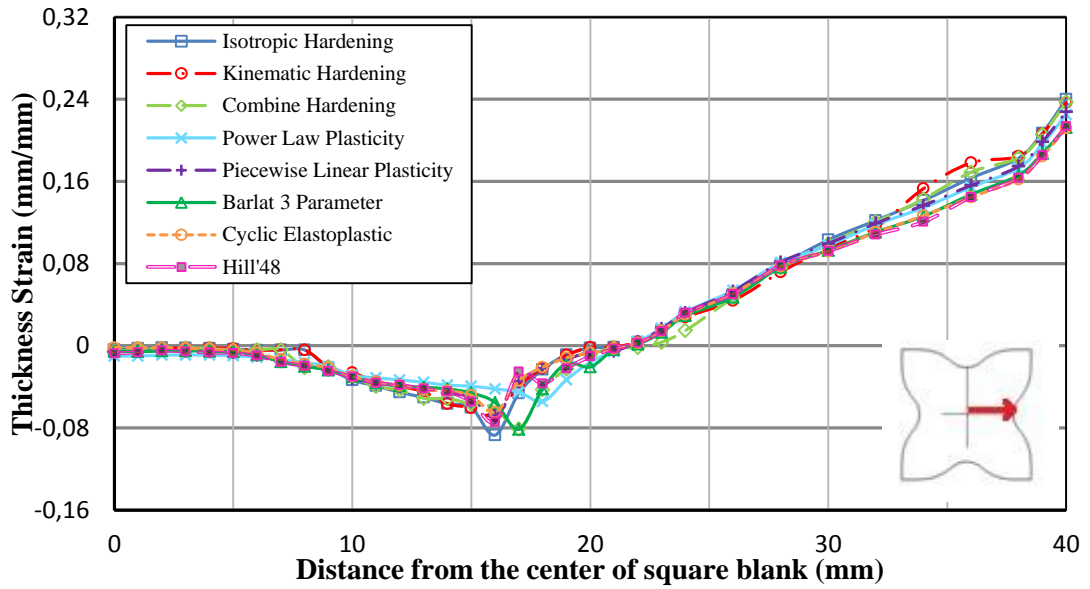


Figure 5.31: Comparison of the thickness strain distributions obtained for different models for 25 mm punch travel (Stainless steel 409 Ni, transverse direction).

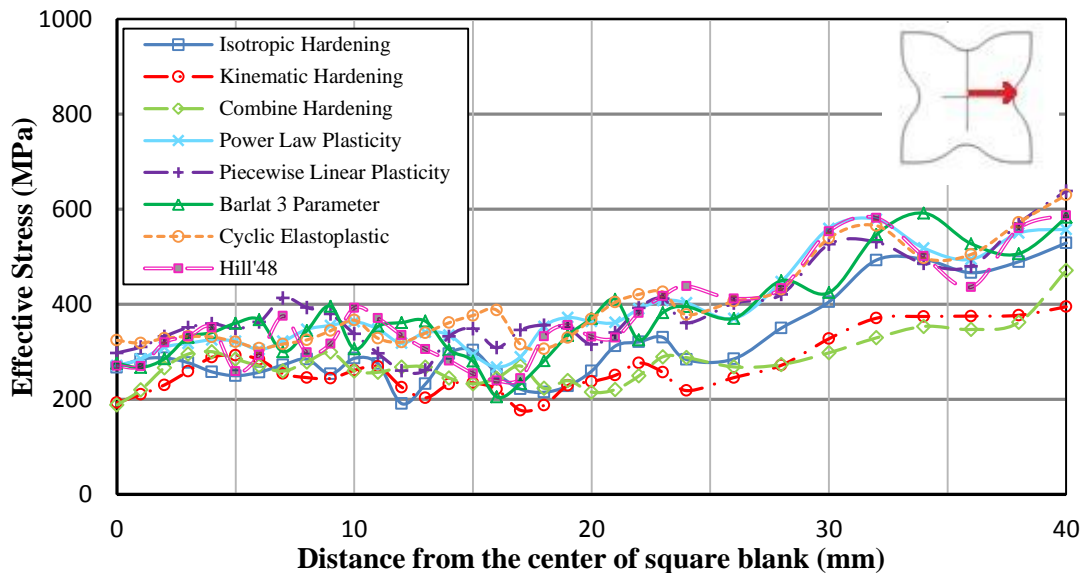


Figure 5.32: Comparison of the effective stress distributions obtained for different models for 25 mm punch travel (Stainless steel 409 Ni, transverse direction).

### 5.3.2 Al-5182 Aluminum

In this section, simulations are performed by using Al-5182 aluminum. Figures 5.33-5.48 show the thickness strain and the effective stress distributions of square cup drawing, in diagonal and transverse directions for four different punch displacements; 10 mm, 15 mm, 20 mm and 25 mm respectively by considering 5 kN blank holder force.

Figures 5.33 and 5.34 show the thickness strain and the effective stress distributions of square cup drawing, respectively, in diagonal direction for 10 mm punch displacement.

In Figures 5.35 and 5.36, the thickness strain and the effective stress distributions of square cup drawing are given, respectively, in transverse direction for 10 mm punch displacement.

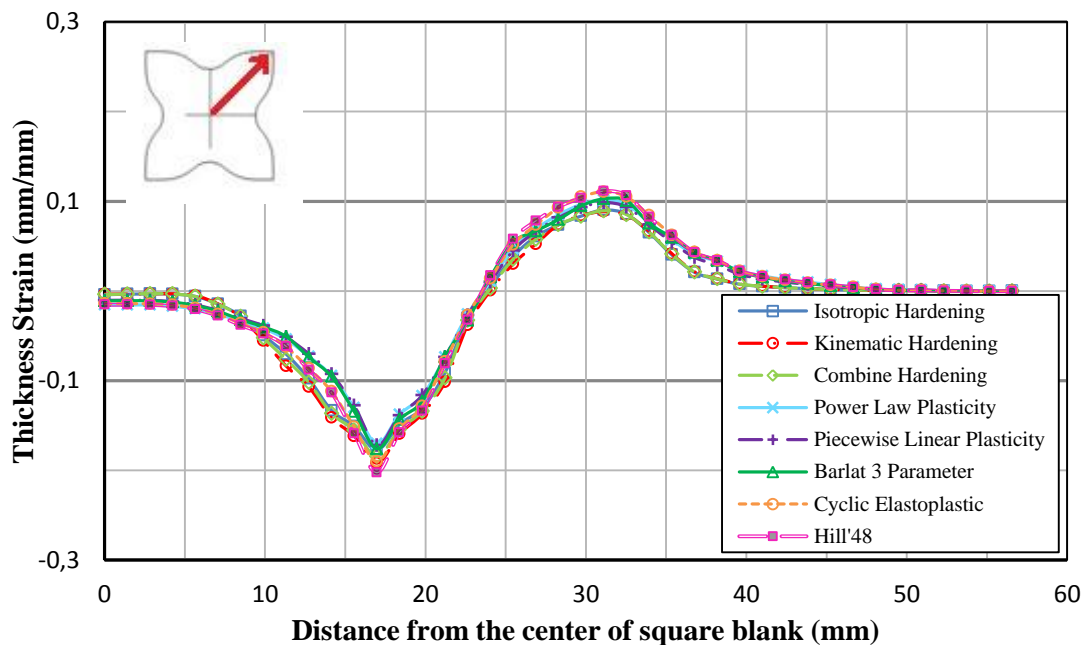


Figure 5.33: Comparison of the thickness strain distributions obtained for different models for 10 mm punch travel (Al-5182, diagonal direction).

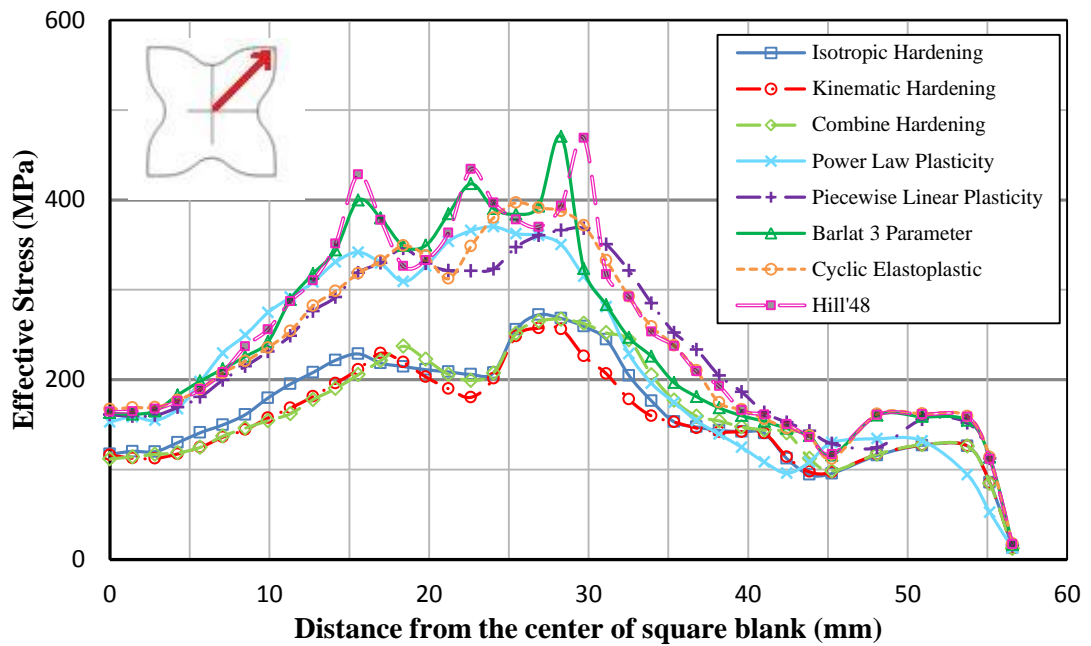


Figure 5.34: Comparison of the effective stress distributions obtained for different models for 10 mm punch travel (Al-5182, diagonal direction).

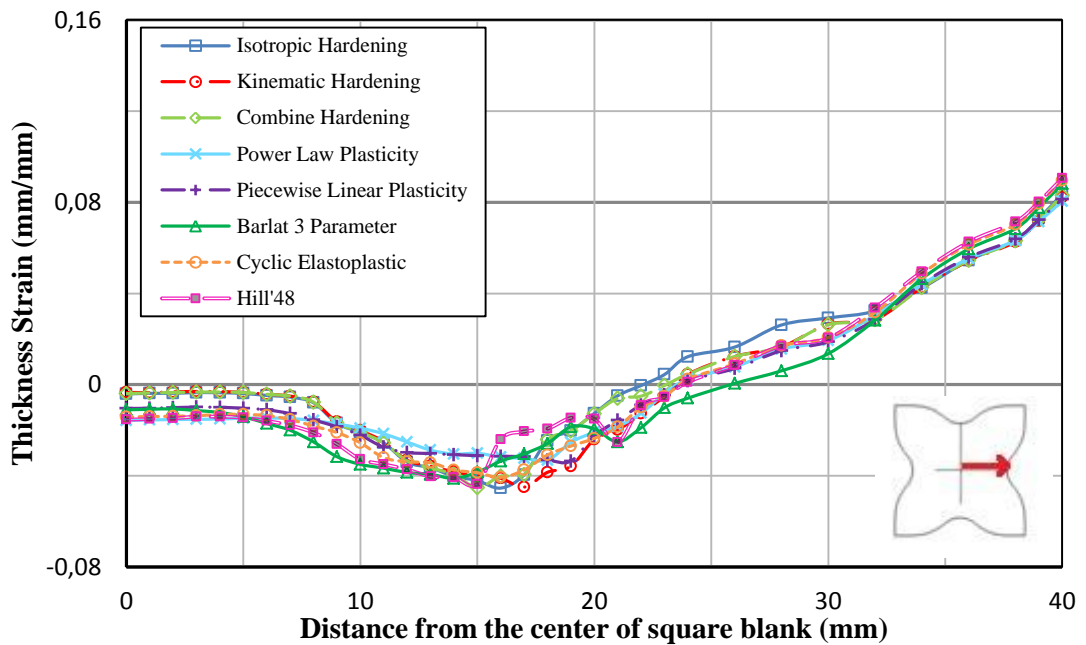


Figure 5.35: Comparison of the thickness strain distributions obtained for different models for 10 mm punch travel (Al-5182, transverse direction).

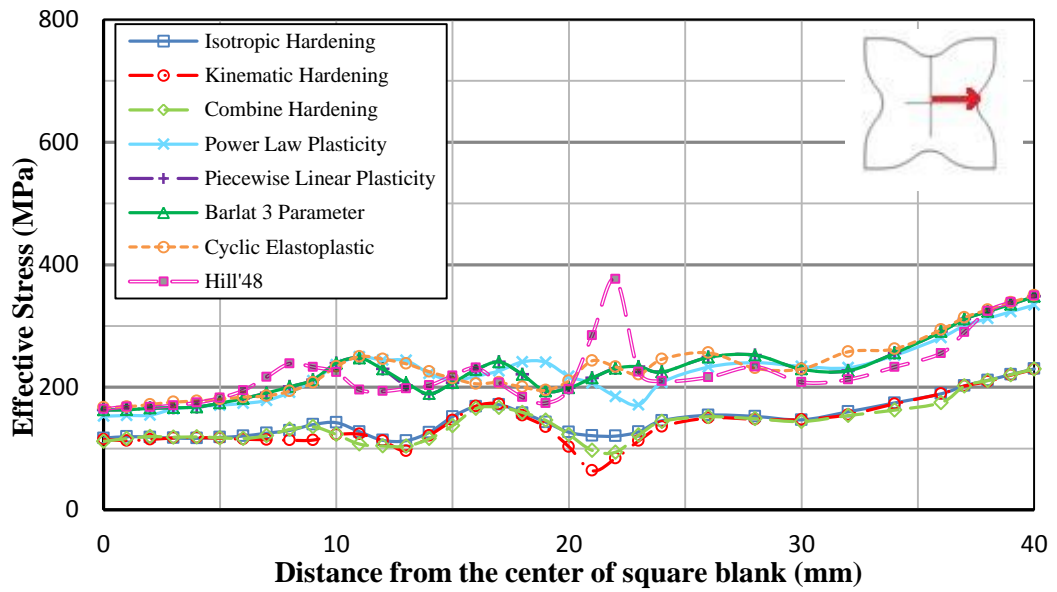


Figure 5.36: Comparison of the effective stress distributions obtained for different models for 10 mm punch travel (Al-5182, transverse direction).

Figures 5.37 and 5.38 show the thickness strain and the effective stress distributions of square cup drawing, respectively, in diagonal direction for 15 mm punch displacement.

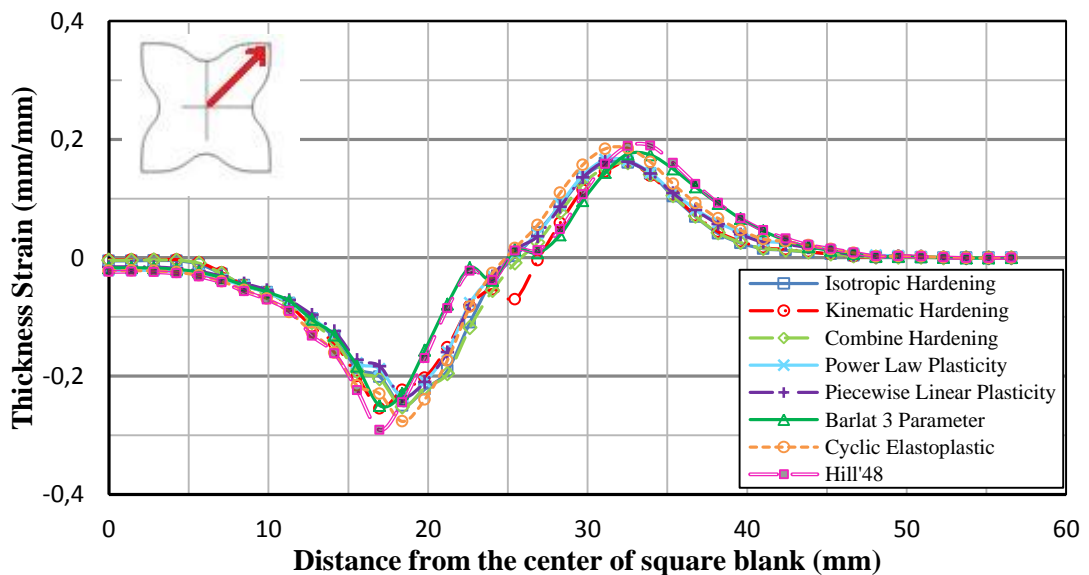


Figure 5.37: Comparison of the thickness strain distributions obtained for different models for 15 mm punch travel (Al-5182, diagonal direction).

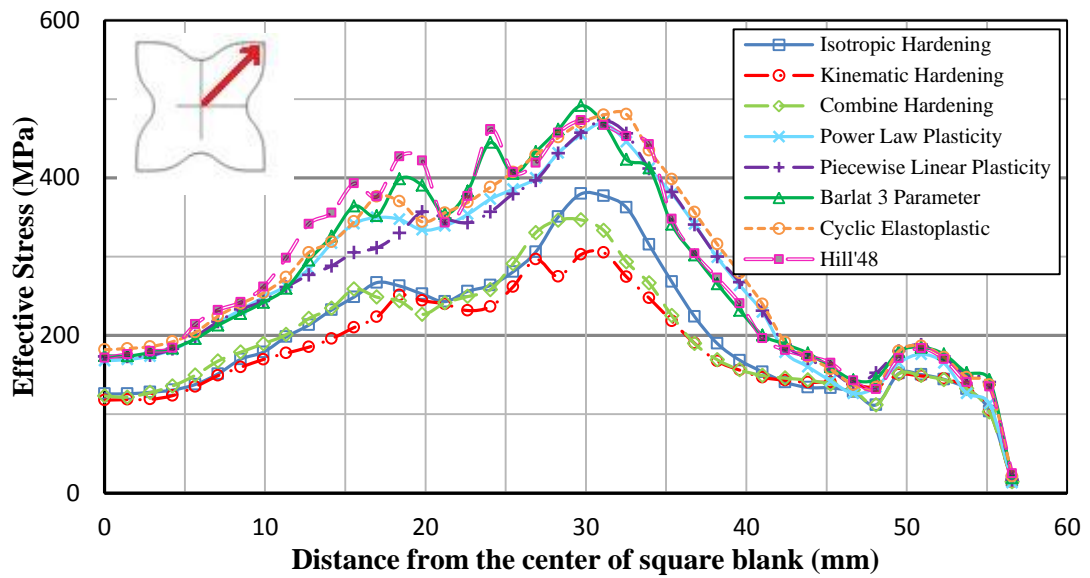


Figure 5.38: Comparison of the effective stress distributions obtained for different models for 15 mm punch travel (Al-5182, diagonal direction).

In Figures 5.39 and 5.40, the thickness strain and the effective stress distributions of square cup drawing are given, respectively, in transverse direction for 15 mm punch displacement.

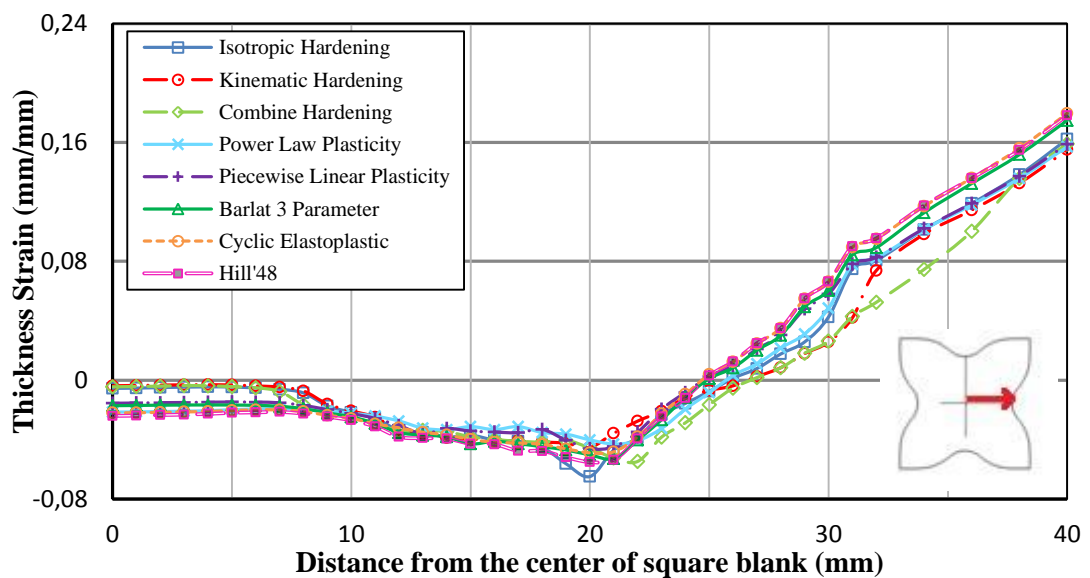


Figure 5.39: Comparison of the thickness strain distributions obtained for different models for 15 mm punch travel (Al-5182, transverse direction).

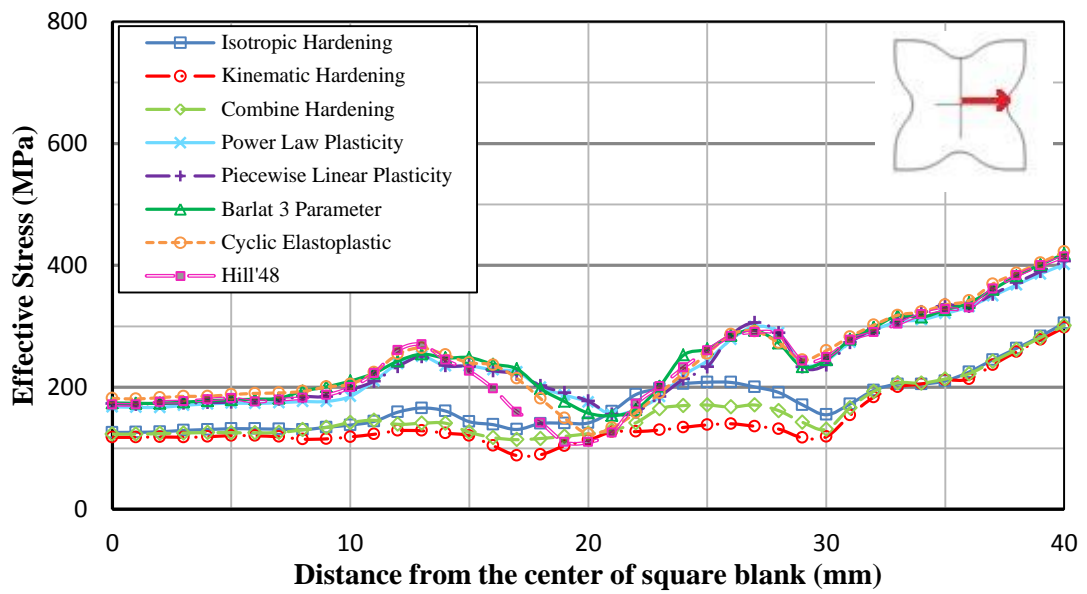


Figure 5.40: Comparison of the effective stress distributions obtained for different models for 15 mm punch travel (Al-5182, transverse direction).

Figures 5.41 and 5.42 show the thickness strain and the effective stress distributions of square cup drawing, respectively, in diagonal direction for 20 mm punch displacement.

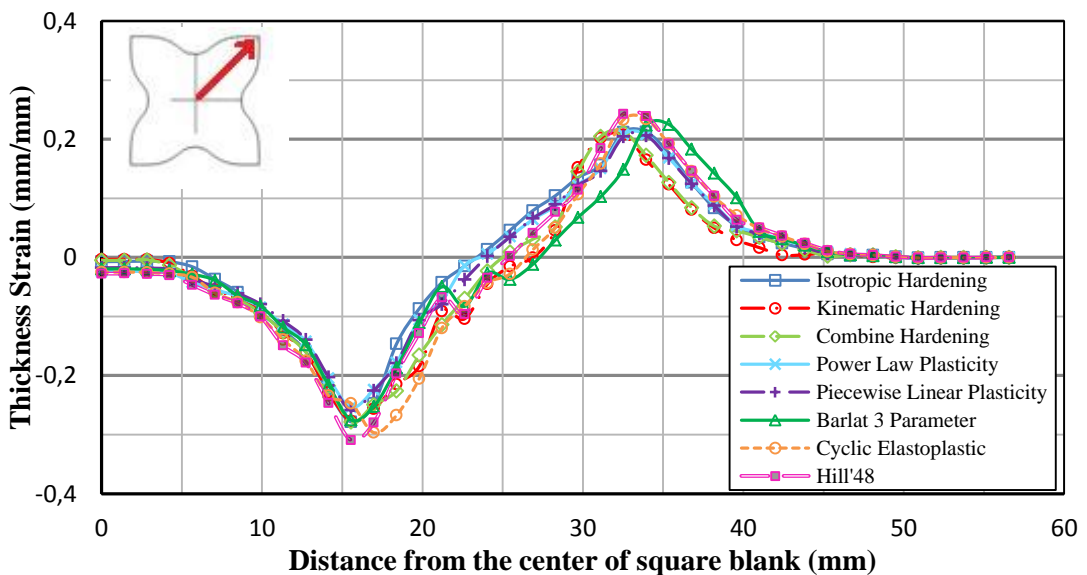


Figure 5.41: Comparison of the thickness strain distributions obtained for different models for 20 mm punch travel (Al-5182, diagonal direction).

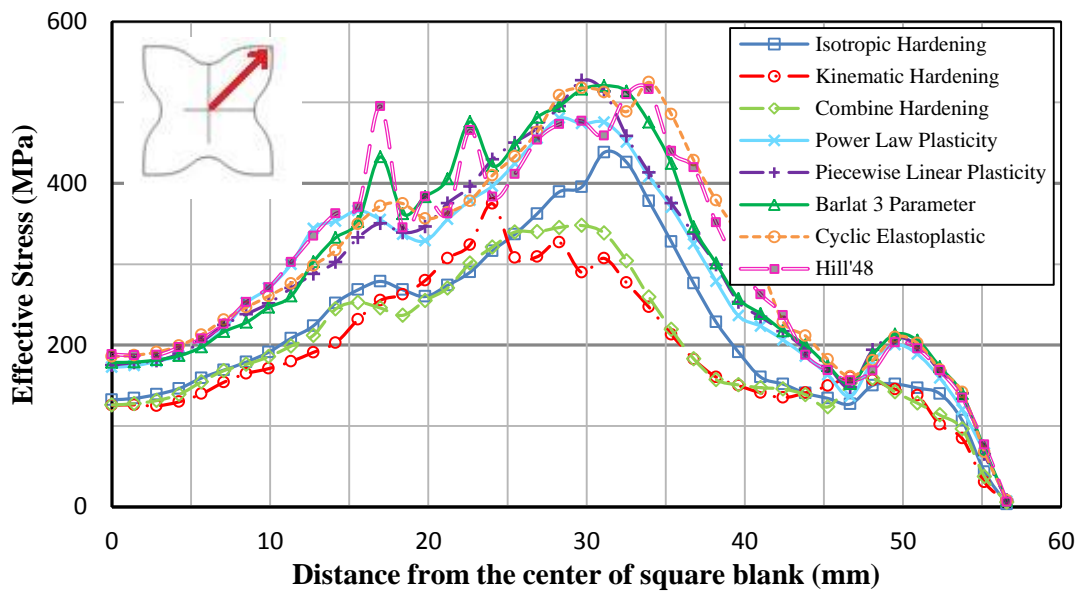


Figure 5.42: Comparison of the effective stress distributions obtained for different models for 20 mm punch travel (Al-5182, diagonal direction).

In Figures 5.43 and 5.44, the thickness strain and the effective stress distributions of square cup drawing are given, respectively, in transverse direction for 20 mm punch displacement.

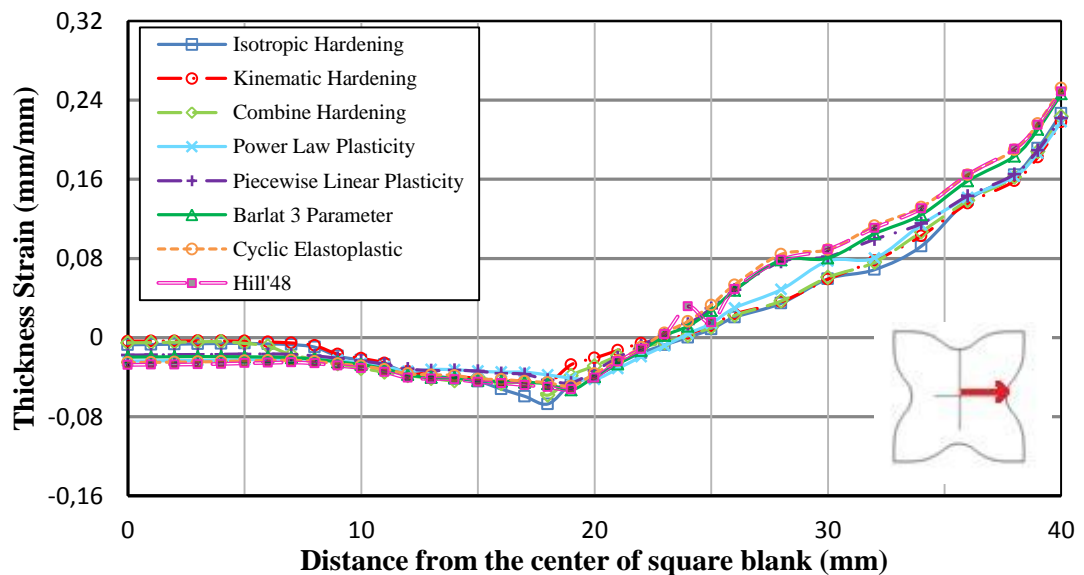


Figure 5.43: Comparison of the thickness strain distributions obtained for different models for 20 mm punch travel (Al-5182, transverse direction).

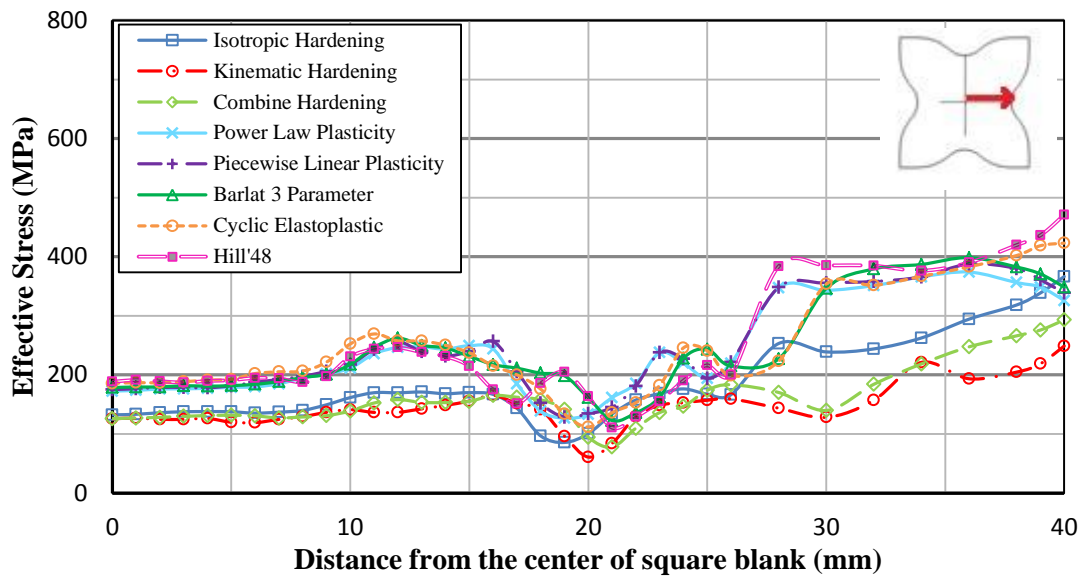


Figure 5.44: Comparison of the effective stress distributions obtained for different models for 20 mm punch travel (Al-5182, transverse direction).

Figures 5.45 and 5.46 show the thickness strain and the effective stress distributions of square cup drawing, respectively, in diagonal direction for 25 mm punch displacement.

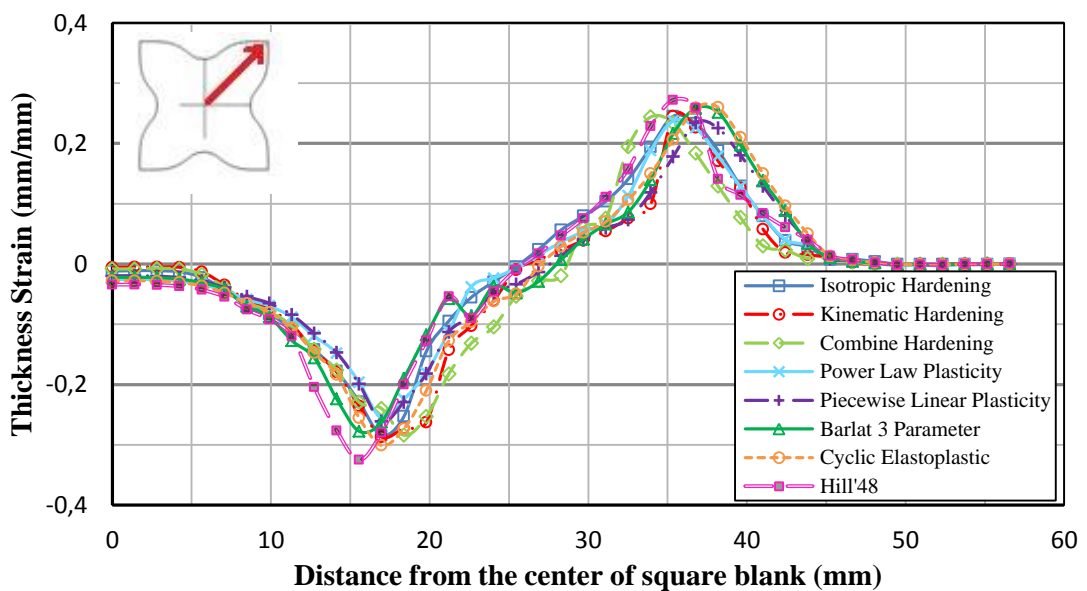


Figure 5.45: Comparison of the thickness strain distributions obtained for different models for 25 mm punch travel (Al-5182, diagonal direction).

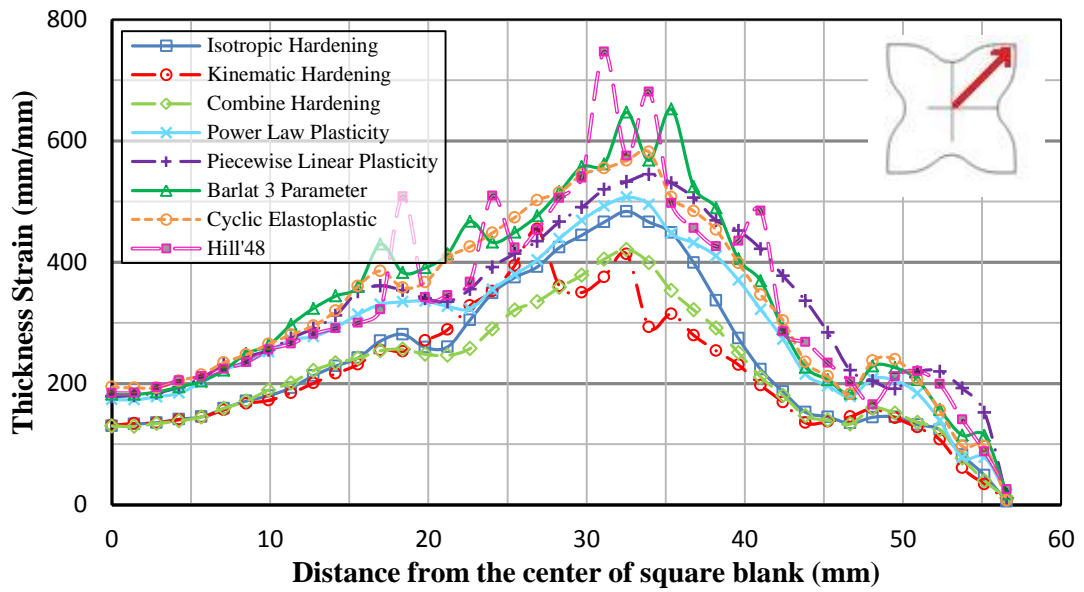


Figure 5.46: Comparison of the effective stress distributions obtained for different models for 25 mm punch travel (Al-5182, diagonal direction).

In Figures 5.47 and 5.48, the thickness strain and the effective stress distributions of square cup drawing are given, respectively, in transverse direction for 25 mm punch displacement.

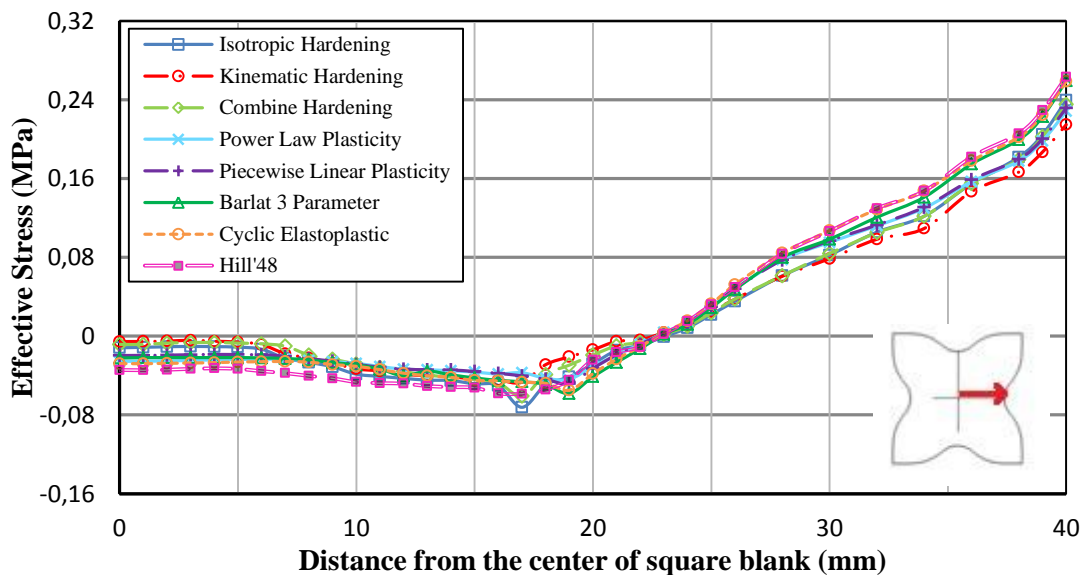


Figure 5.47: Comparison of the thickness strain distributions obtained for different models for 25 mm punch travel (Al-5182, transverse direction).

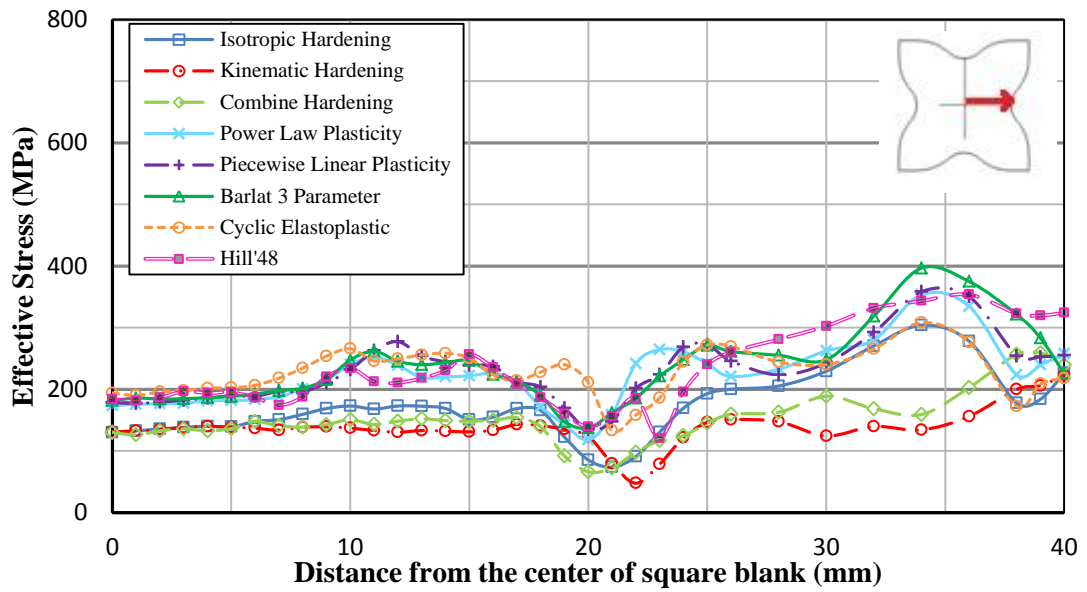


Figure 5.48: Comparison of the effective stress distributions obtained for different models for 25 mm punch travel (Al-5182, transverse direction).

### 5.3.3 St12 Steel

In this section in order to investigate effects of constitutive models and blank holding forces, simulations are performed by using St12 steel under the action of three different blank holder forces; 2 kN, 4 kN and 5 kN.

Figures 5.49 and 5.50 show the thickness strain and the effective stress distributions of square cup drawing, respectively, in diagonal direction by considering 2 kN blank holder force for 10 mm punch displacement.

In Figures 5.51 and 5.52, the thickness strain and the effective stress distributions of square cup drawing are given, respectively, in transverse direction by considering 2 kN blank holder force for 10 mm punch displacement.

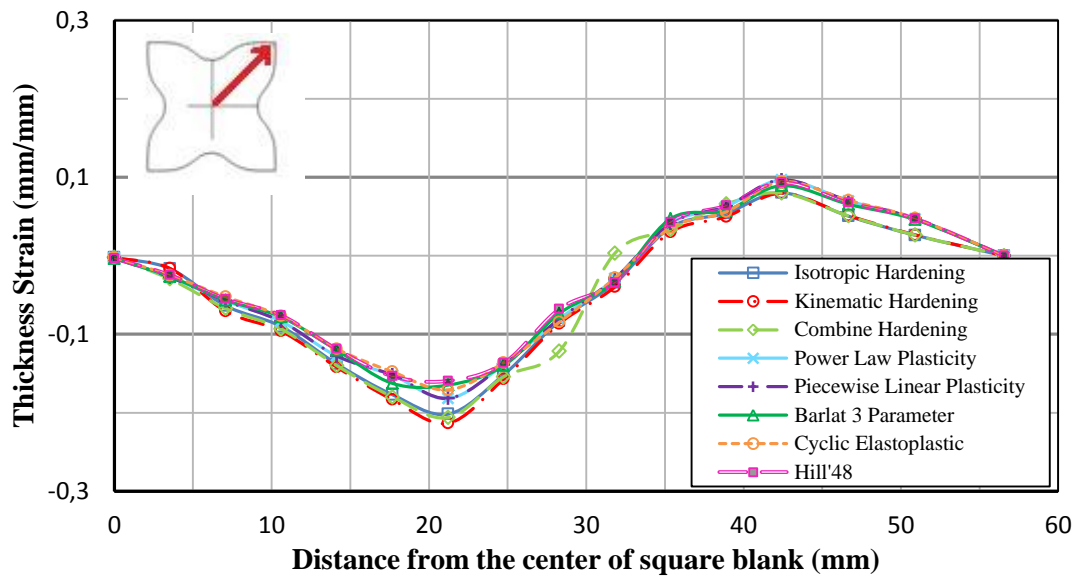


Figure 5.49: Comparison of the thickness strain distributions obtained for different models for 10 mm punch travel (St12 steel, diagonal direction, blank holder 2 kN).

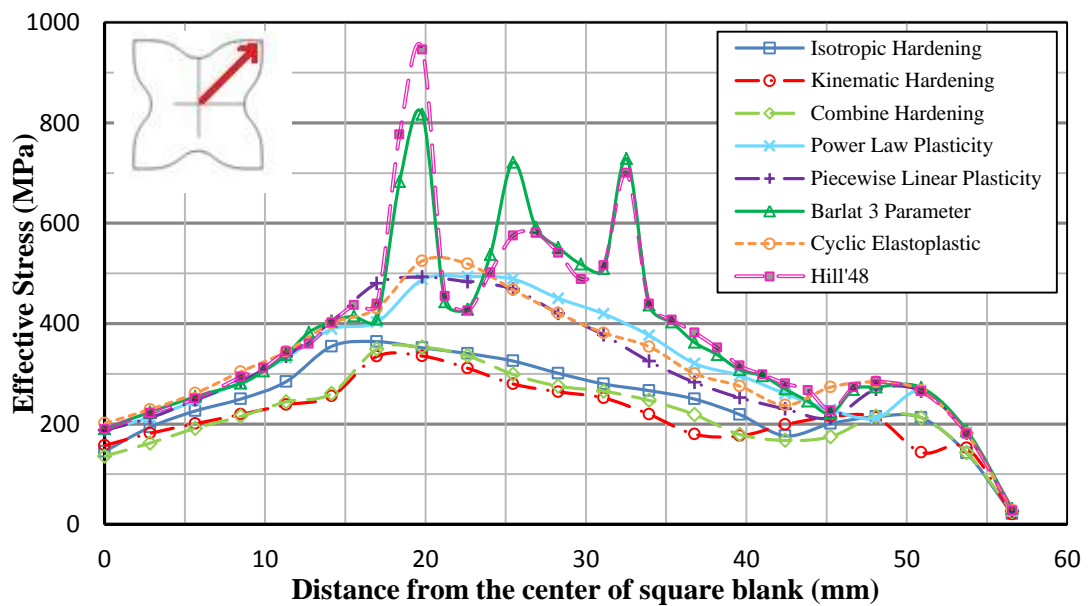


Figure 5.50: Comparison of the effective stress distributions obtained for different models for 10 mm punch travel (St12 steel, diagonal direction, blank holder 2 kN).

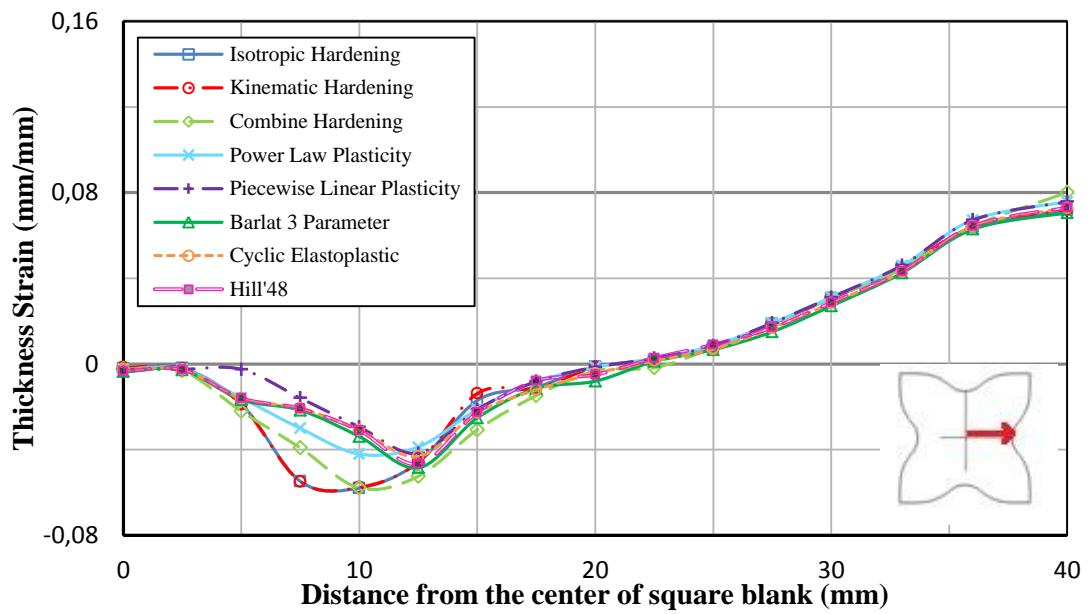


Figure 5.51: Comparison of the thickness strain distributions obtained for different models for 10 mm punch travel (St12 steel, transverse direction, blank holder 2 kN).

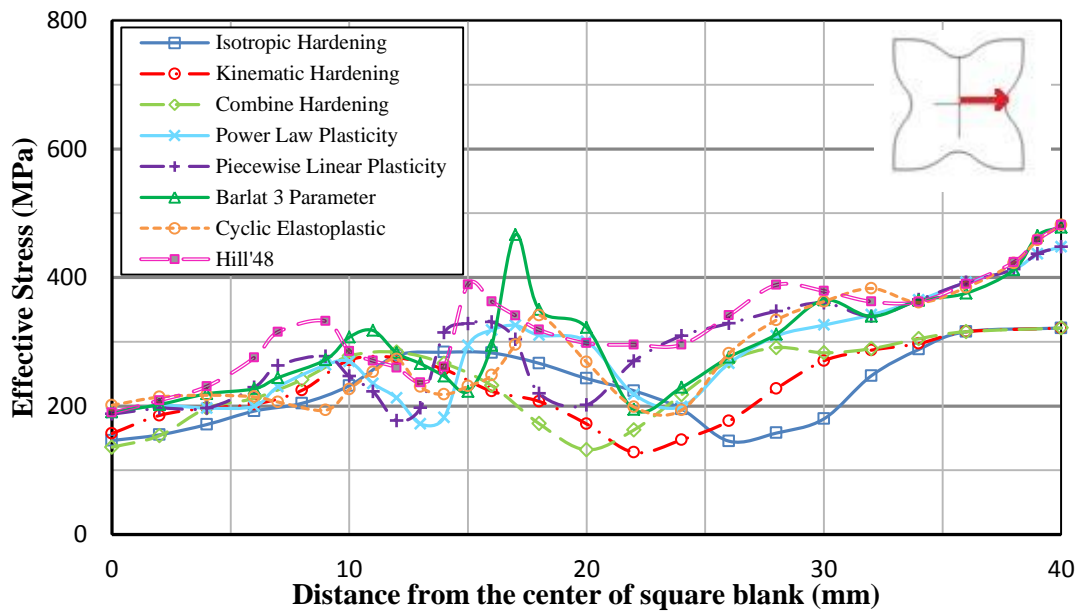


Figure 5.52: Comparison of the effective stress distributions obtained for different models for 10 mm punch travel (St12 steel, transverse direction, blank holder 2 kN).

Figures 5.53 and 5.54 show the thickness strain and the effective stress distributions of square cup drawing, respectively, in diagonal direction by considering 2 kN blank holder force for 15 mm punch displacement.

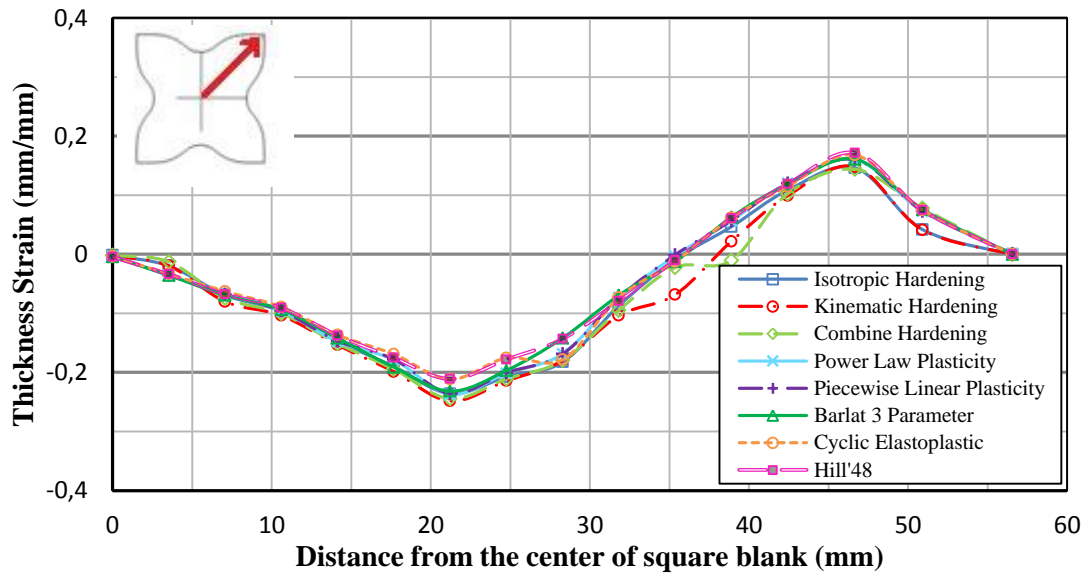


Figure 5.53: Comparison of the thickness strain distributions obtained for different models for 15 mm punch travel (St12 steel, diagonal direction, blank holder 2 kN).

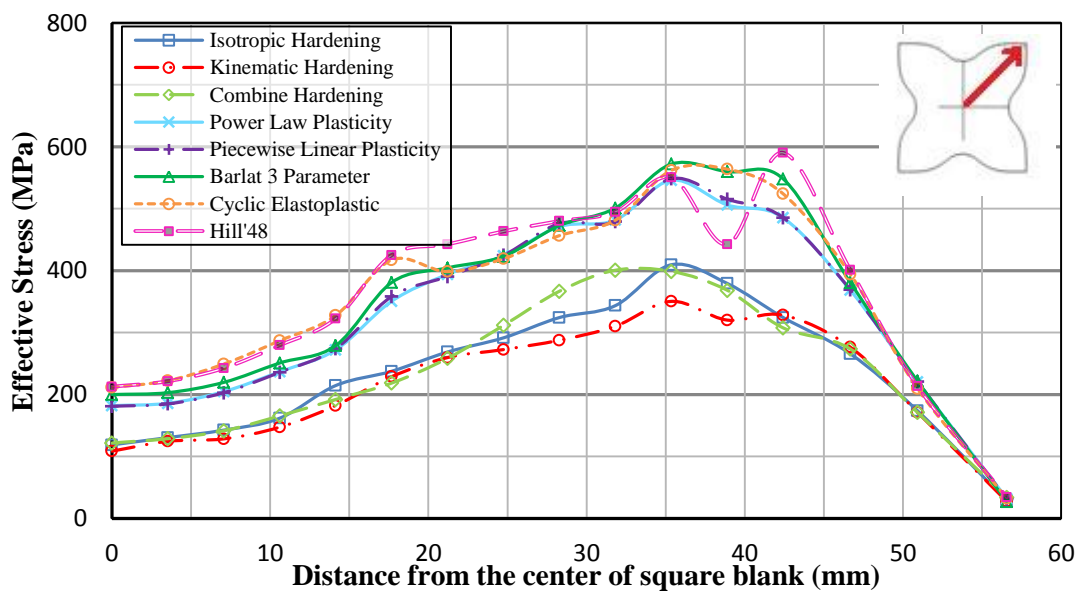


Figure 5.54: Comparison of the effective stress distributions obtained for different models for 15 mm punch travel (St12 steel, diagonal direction, blank holder 2 kN).

In Figures 5.55 and 5.56, the thickness strain and the effective stress distributions of square cup drawing are given, respectively, in transverse direction by considering 2 kN blank holder force for 15 mm punch displacement.

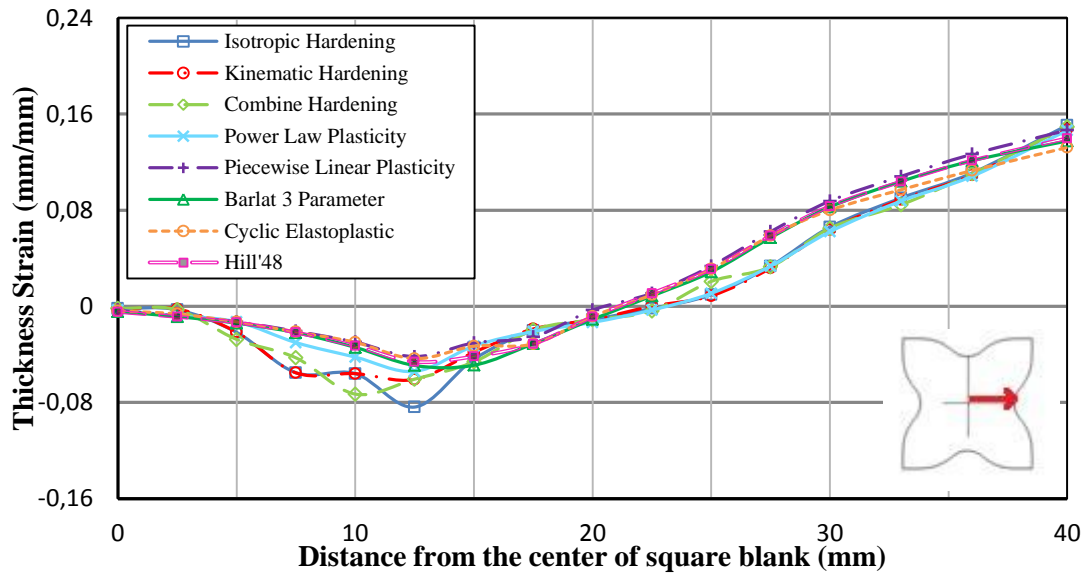


Figure 5.55: Comparison of the thickness strain distributions obtained for different models for 15 mm punch travel (St12 steel, transverse direction, blank holder 2 kN).

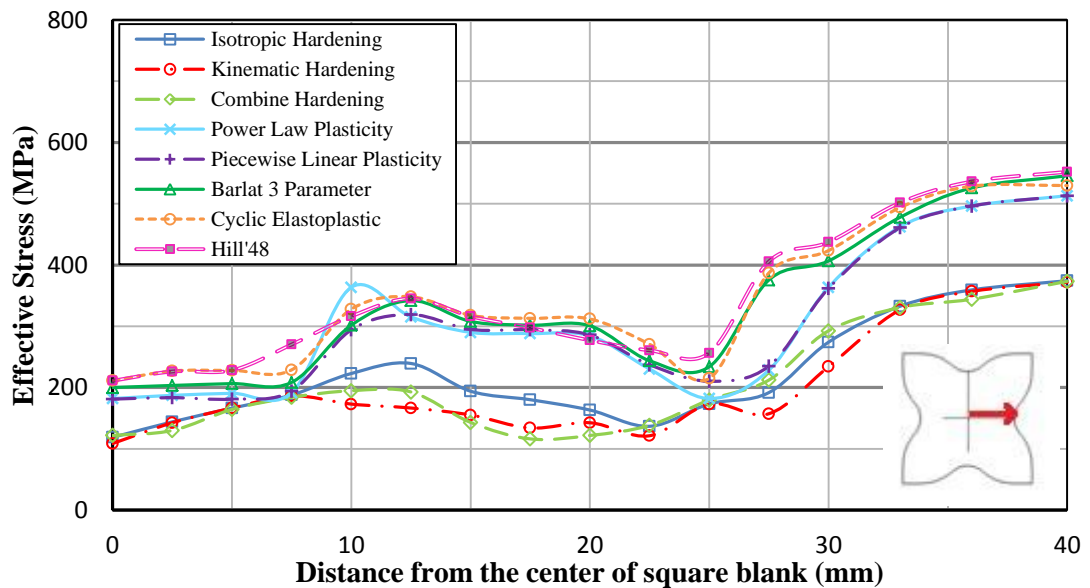


Figure 5.56: Comparison of the effective stress distributions obtained for different models for 15 mm punch travel (St12 steel, transverse direction, blank holder 2 kN).

Figures 5.57 and 5.58 show the thickness strain and the effective stress distributions of square cup drawing, respectively, in diagonal direction by considering 2 kN blank holder force for 20 mm punch displacement.

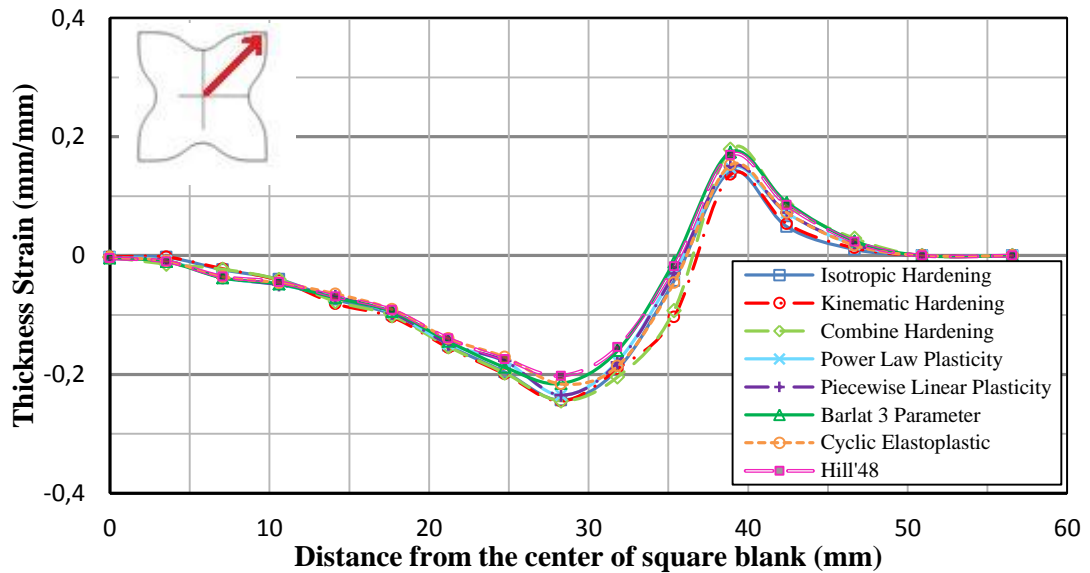


Figure 5.57: Comparison of the thickness strain distributions obtained for different models for 20 mm punch travel (St12 steel, diagonal direction, blank holder 2 kN).

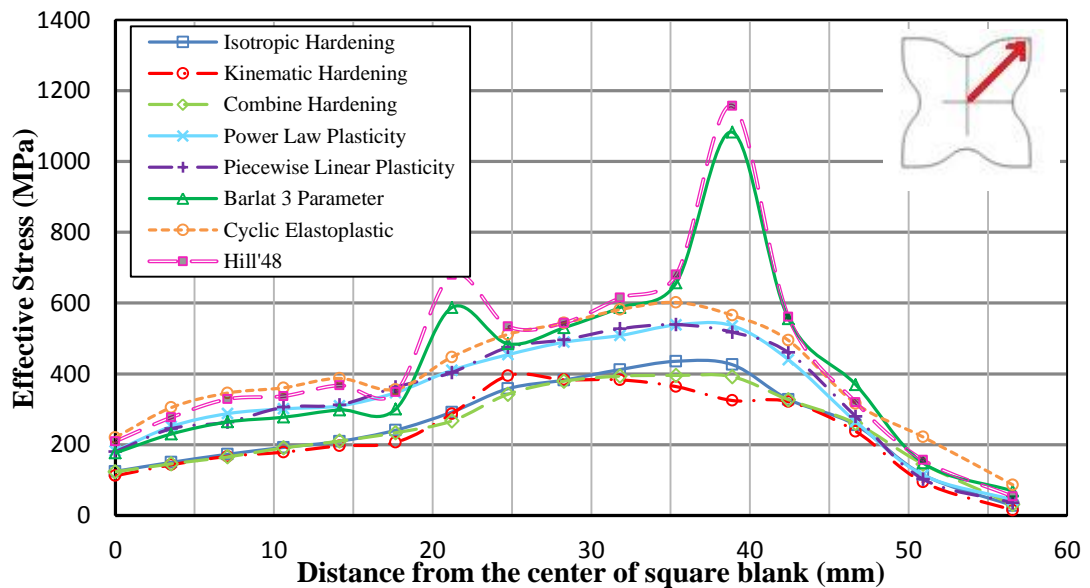


Figure 5.58: Comparison of the effective stress distributions obtained for different models for 20 mm punch travel (St12 steel, diagonal direction, blank holder 2 kN).

In Figures 5.59 and 5.60, the thickness strain and the effective stress distributions of square cup drawing are given, respectively, in transverse direction by considering 2 kN blank holder force for 20 mm punch displacement.

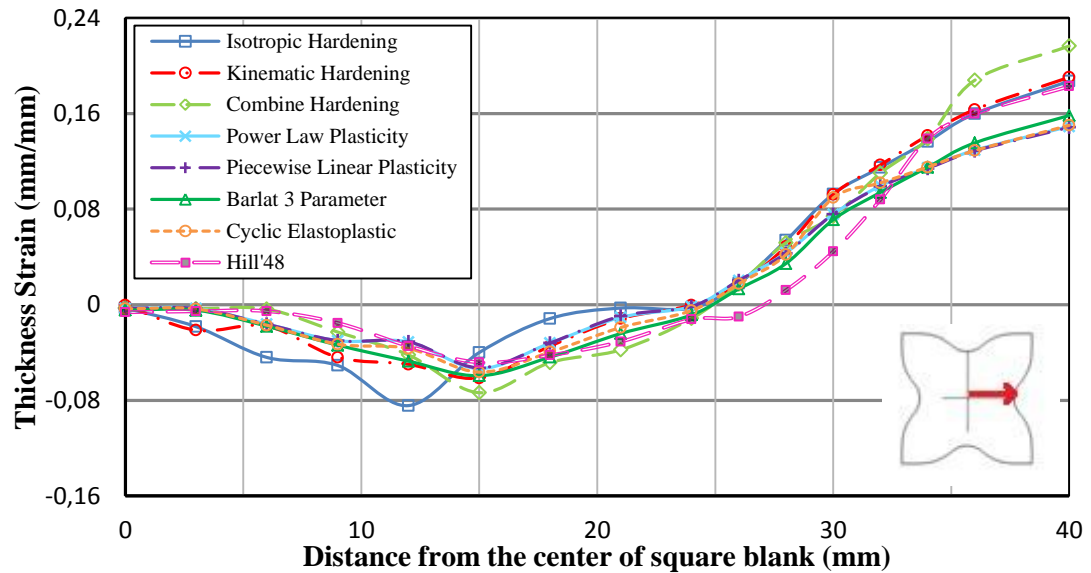


Figure 5.59: Comparison of the thickness strain distributions obtained for different models for 20 mm punch travel (St12 steel, transverse direction, blank holder 2 kN).

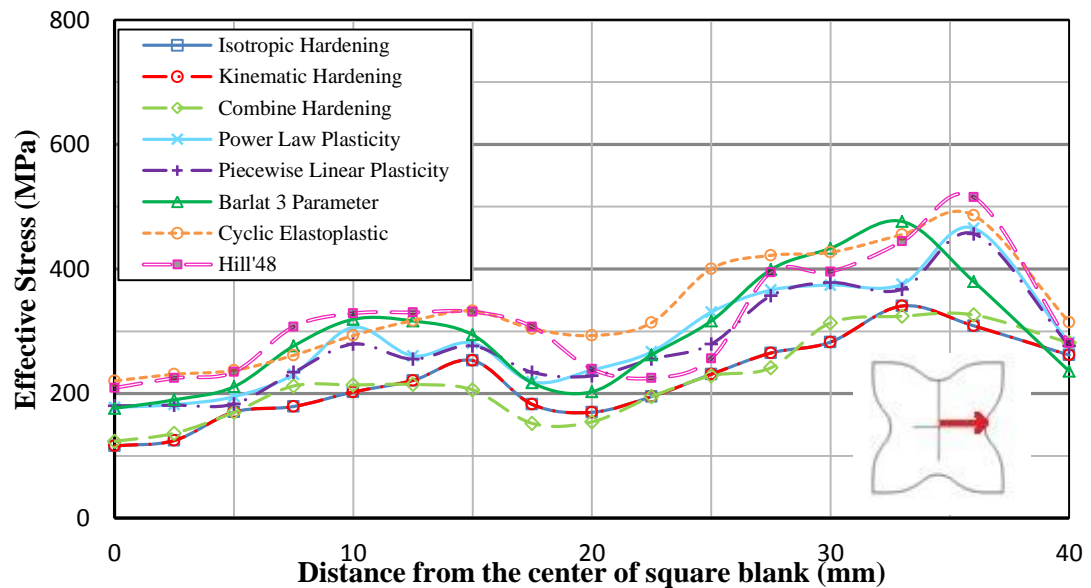


Figure 6.60: Comparison of the effective stress distributions obtained for different models for 20 mm punch travel (St12 steel, transverse direction, blank holder 2 kN).

Figures 5.61 and 5.62 show the thickness strain and the effective stress distributions of square cup drawing, respectively, in diagonal direction by considering 2 kN blank holder force for 25 mm punch displacement.

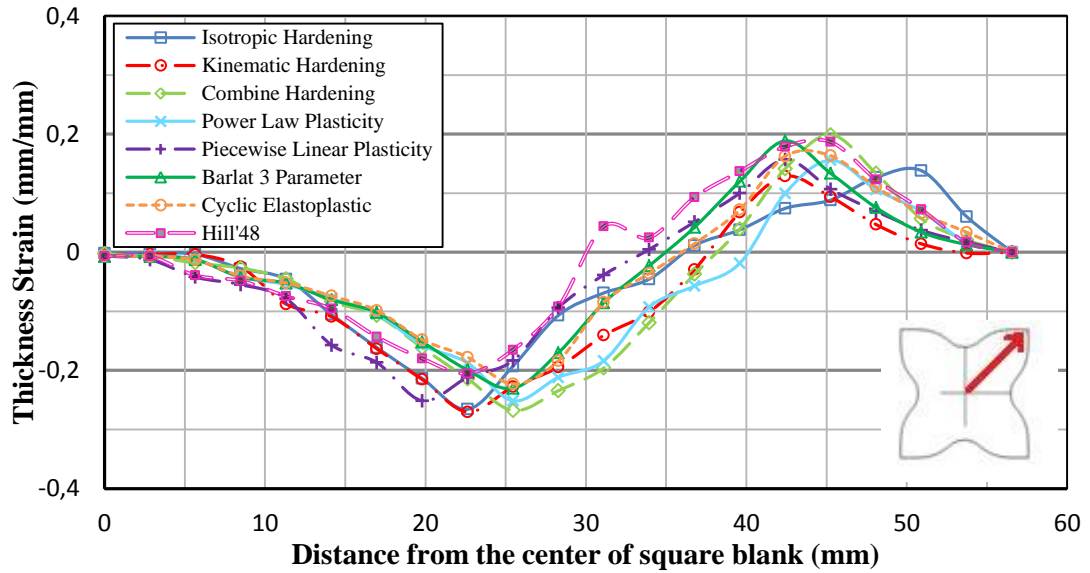


Figure 5.61: Comparison of the thickness strain distributions obtained for different models for 25 mm punch travel (St12 steel, diagonal direction, blank holder 2 kN).

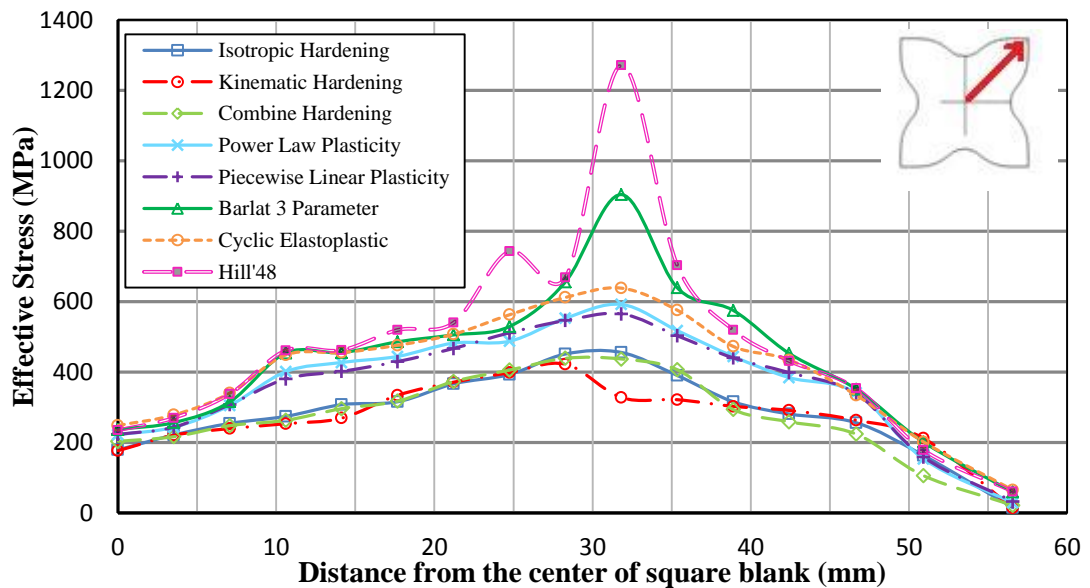


Figure 5.62: Comparison of the effective stress distributions obtained for different models for 25 mm punch travel (St12 steel, diagonal direction, blank holder 2 kN).

In Figures 5.63 and 5.64, the thickness strain and the effective stress distributions of square cup drawing are given, respectively, in transverse direction by considering 2 kN blank holder force for 25 mm punch displacement.

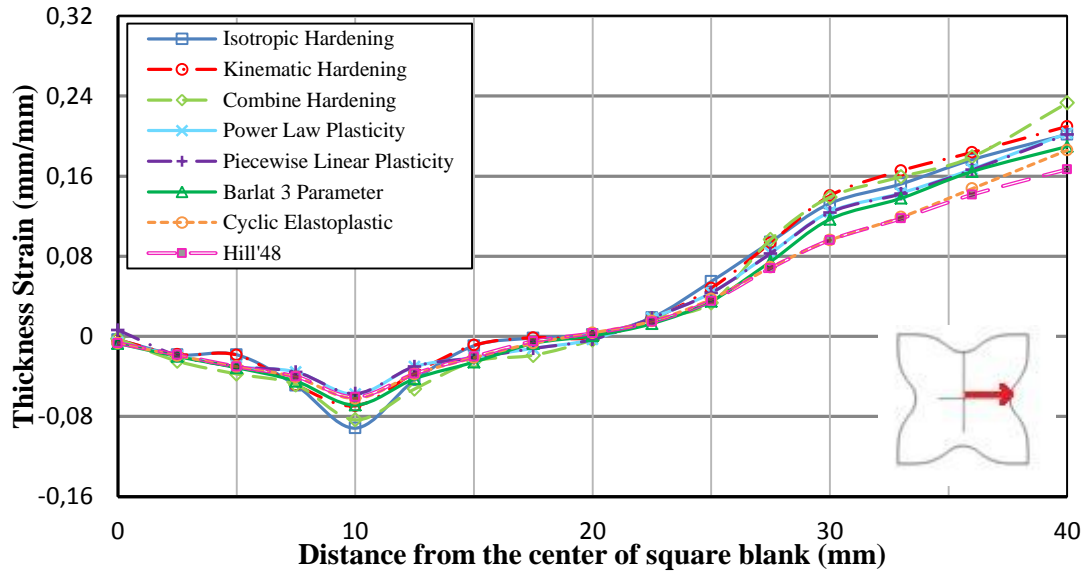


Figure 5.63: Comparison of the thickness strain distributions obtained for different models for 25mm punch travel (St12 steel, transverse direction, blank holder 2 kN).

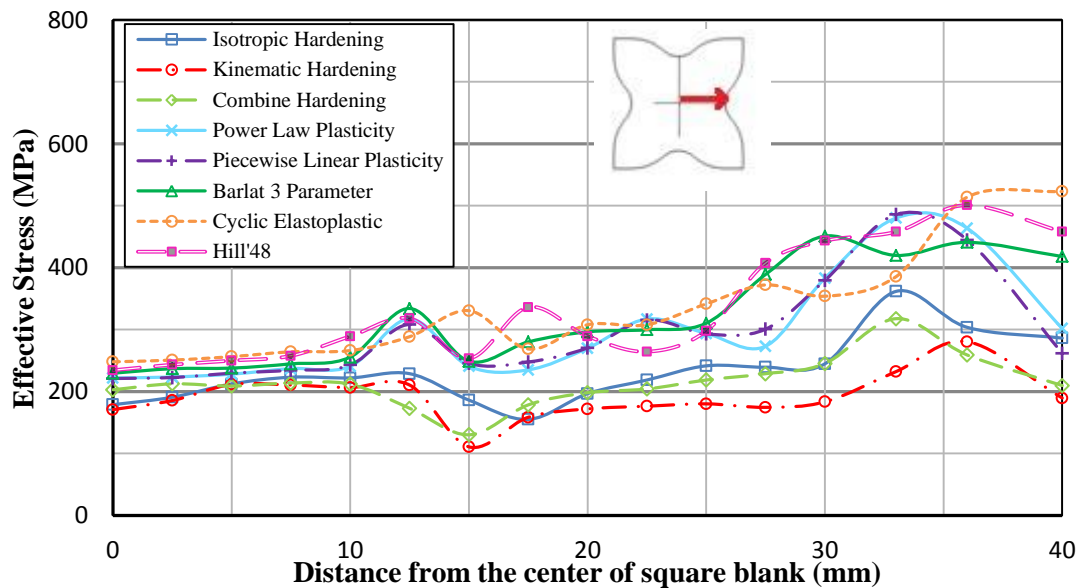


Figure 5.64: Comparison of the effective stress distributions obtained for different models for 25 mm punch travel (St12 steel, transverse direction, blank holder 2 kN).

Figures 5.65 and 5.66 show the thickness strain and the effective stress distributions of square cup drawing, respectively, in diagonal direction by considering 4 kN blank holder force for 10 mm punch displacement.

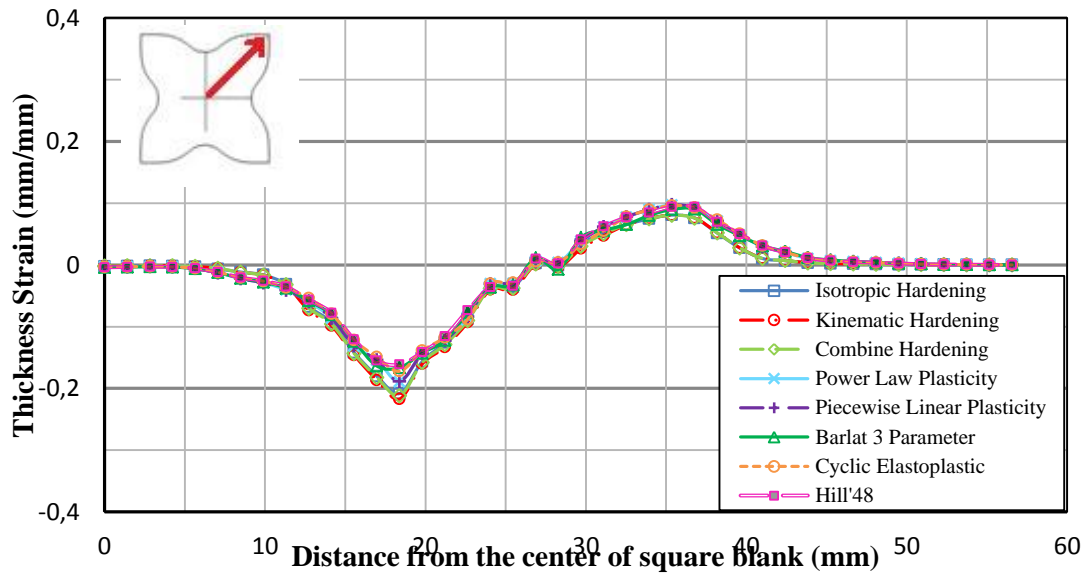


Figure 5.65: Comparison of the thickness strain distributions obtained for different models for 10 mm punch travel (St12 steel, diagonal direction, blank holder 4 kN).

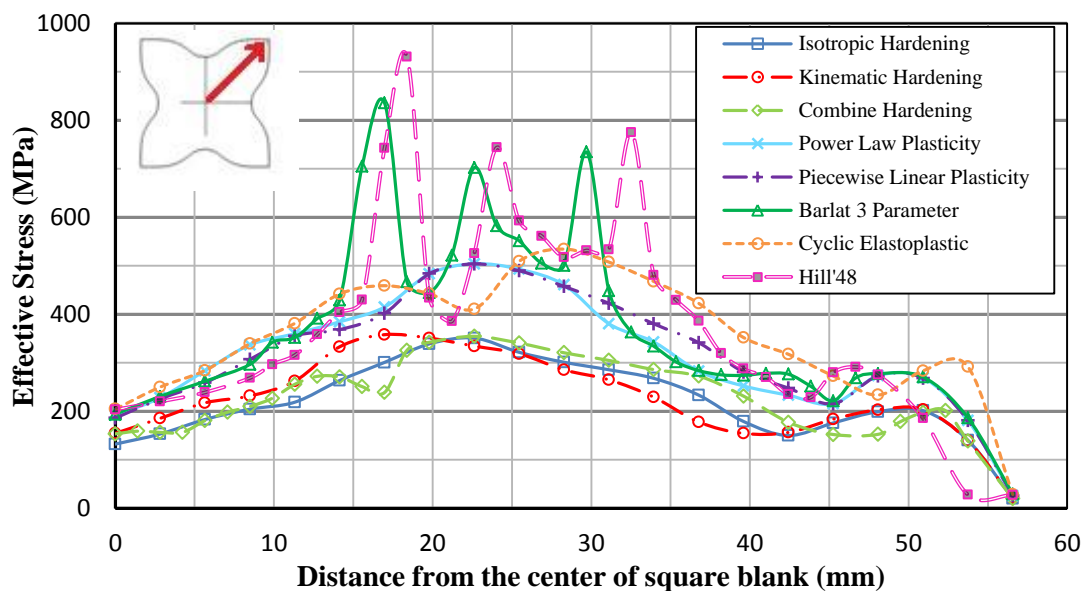


Figure 5.66: Comparison of the effective stress distributions obtained for different models for 10 mm punch travel (St12 steel, diagonal direction, blank holder 4 kN).

In Figures 5.67 and 5.68, the thickness strain and the effective stress distributions of square cup drawing are given, respectively, in transverse direction by considering 4 kN blank holder force for 10 mm punch displacement.

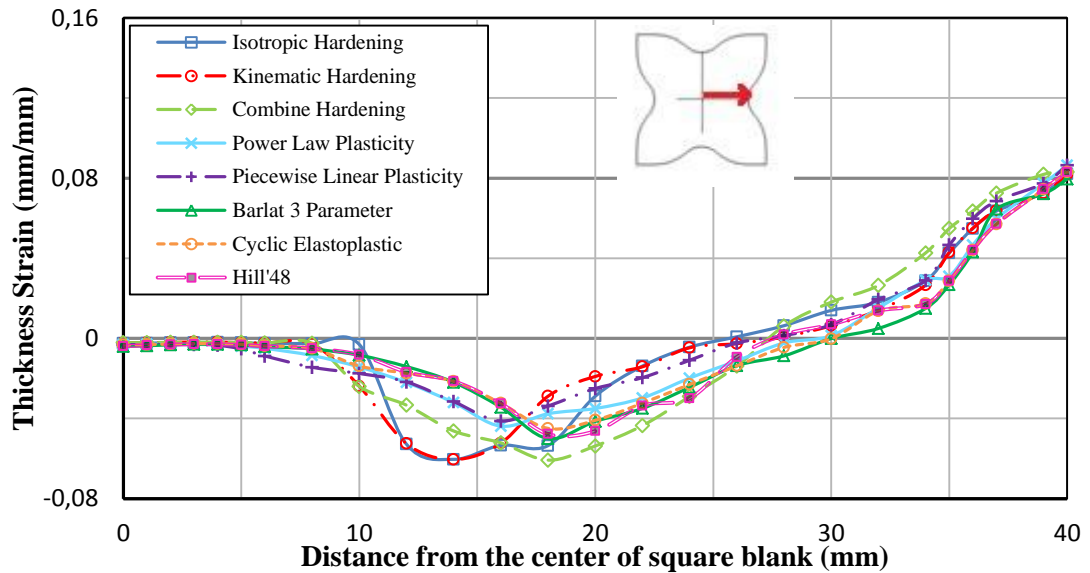


Figure 5.67: Comparison of the thickness strain distributions obtained for different models for 10 mm punch travel (St12 steel, transverse direction, blank holder 4 kN).

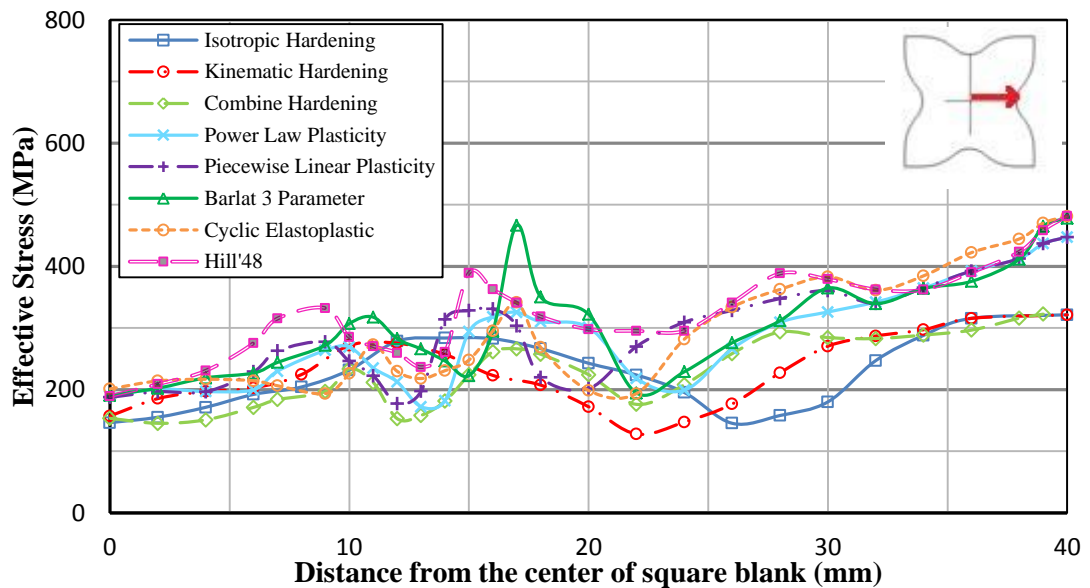


Figure 5.68: Comparison of the effective stress distributions obtained for different models for 10 mm punch travel (St12 steel, transverse direction, blank holder 4 kN).

Figures 5.69 and 5.70 show the thickness strain and the effective stress distributions of square cup drawing, respectively, in diagonal direction by considering 4 kN blank holder force for 15 mm punch displacement.

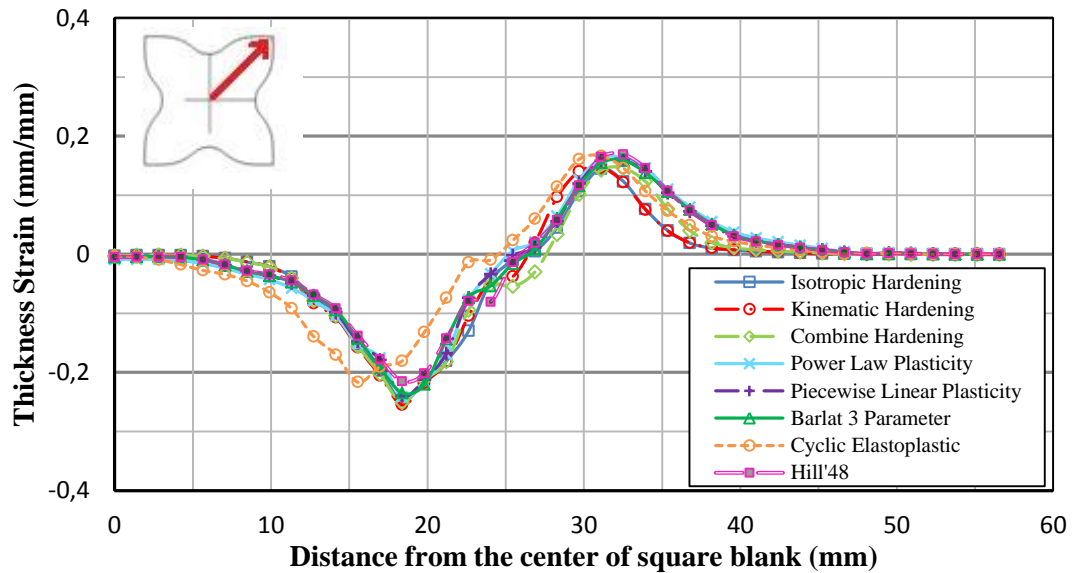


Figure 5.69: Comparison of the thickness strain distributions obtained for different models for 15 mm punch travel (St12 steel, diagonal direction, blank holder 4 kN).

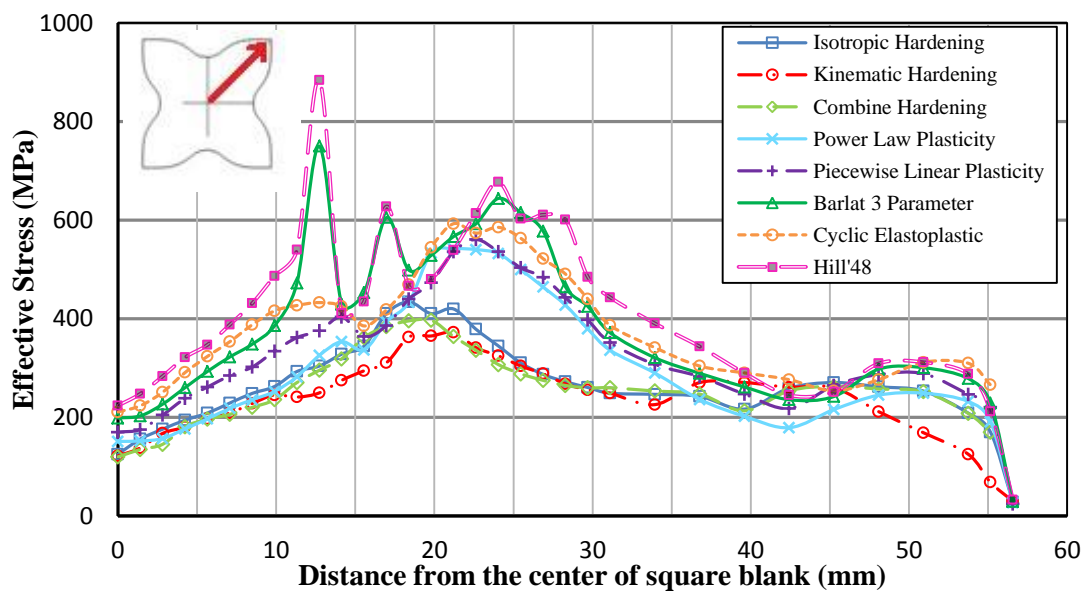


Figure 5.70: Comparison of the effective stress distributions obtained for different models for 15 mm punch travel (St12 steel, diagonal direction, blank holder 4 kN).

In Figures 5.71 and 5.72, the thickness strain and the effective stress distributions of square cup drawing are given, respectively, in transverse direction by considering 4 kN blank holder force for 15 mm punch displacement.

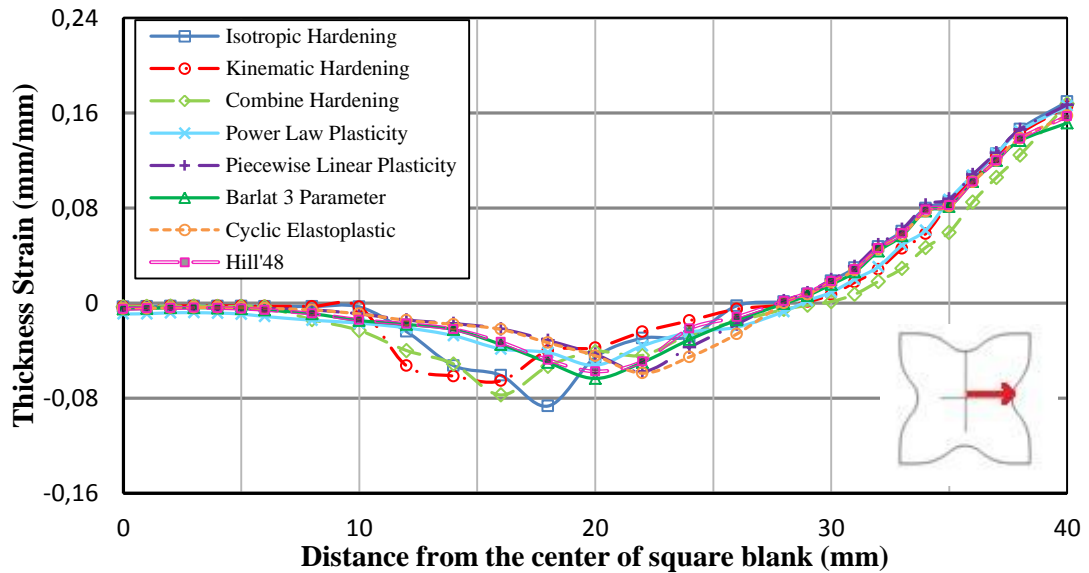


Figure 5.71: Comparison of the thickness strain distributions obtained for different models for 15 mm punch travel (St12 steel, transverse direction, blank holder 4 kN).

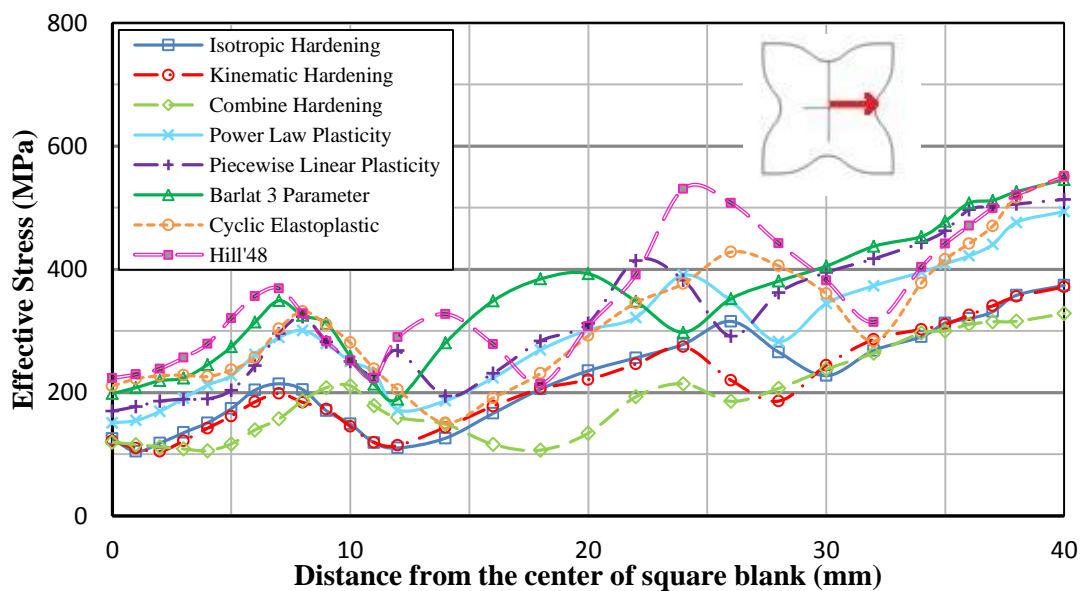


Figure 5.72: Comparison of the effective stress distributions obtained for different models for 15 mm punch travel (St12 steel, transverse direction, blank holder 4 kN).

Figures 5.73 and 5.74 show the thickness strain and the effective stress distributions of square cup drawing, respectively, in diagonal direction by considering 4 kN blank holder force for 20 mm punch displacement.

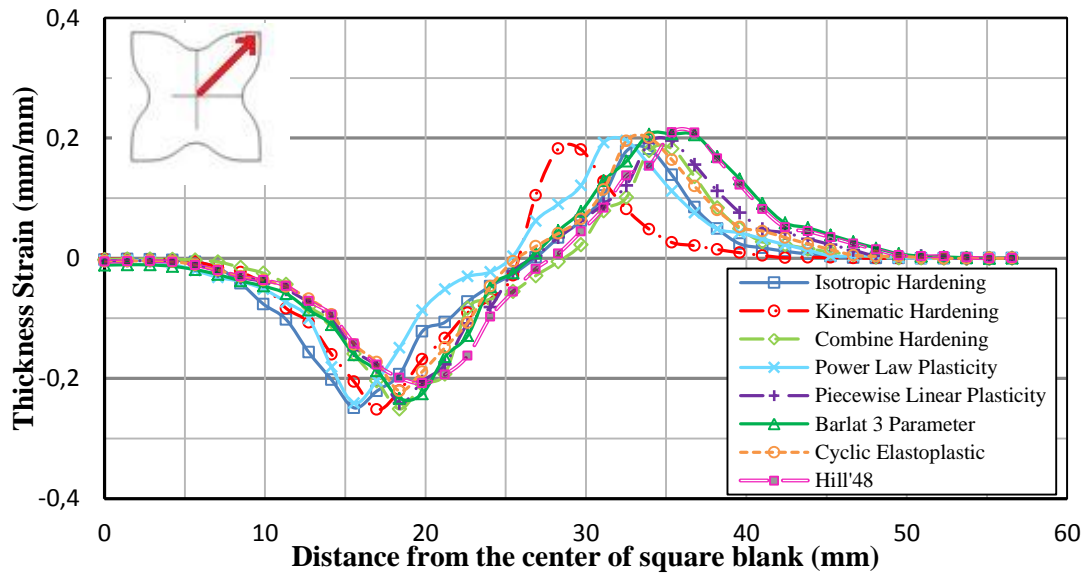


Figure 5.73: Comparison of the thickness strain distributions obtained for different models for 20 mm punch travel (St12 steel, diagonal direction, blank holder 4 kN).

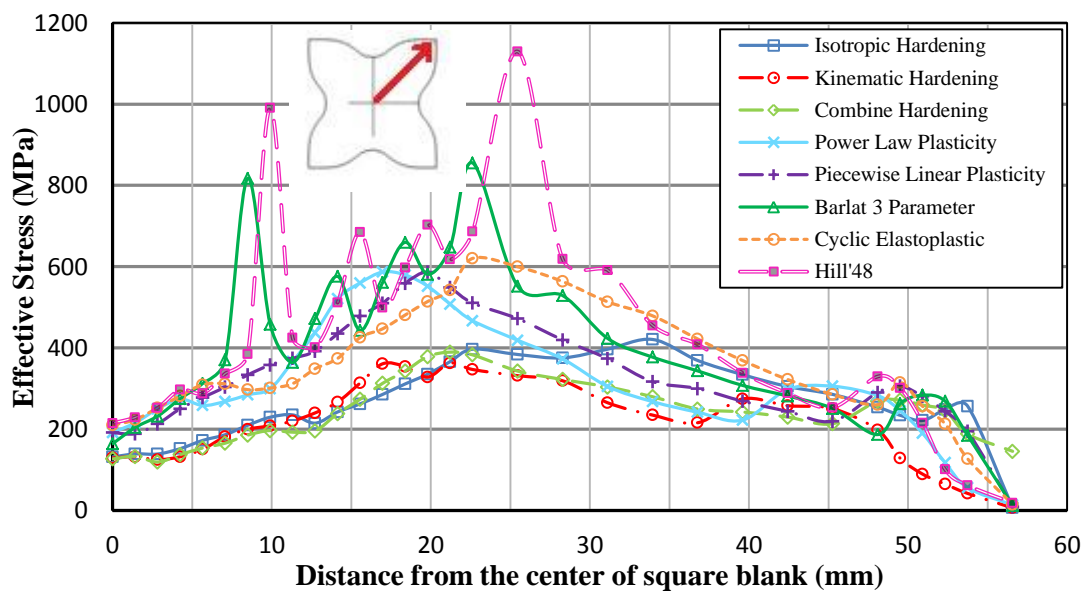


Figure 5.74: Comparison of the effective stress distributions obtained for different models for 20 mm punch travel (St12 steel, diagonal direction, blank holder 4 kN).

In Figures 5.75 and 5.76, the thickness strain and the effective stress distributions of square cup drawing are given, respectively, in transverse direction by considering 4 kN blank holder force for 20 mm punch displacement.

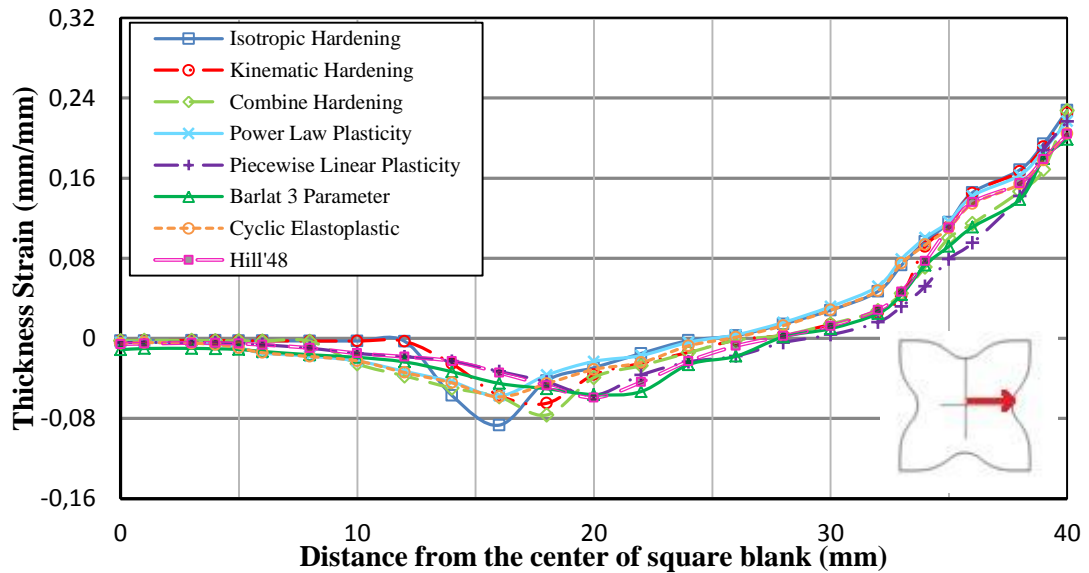


Figure 5.75: Comparison of the thickness strain distributions obtained for different models for 20 mm punch travel (St12 steel, transverse direction, blank holder 4 kN).

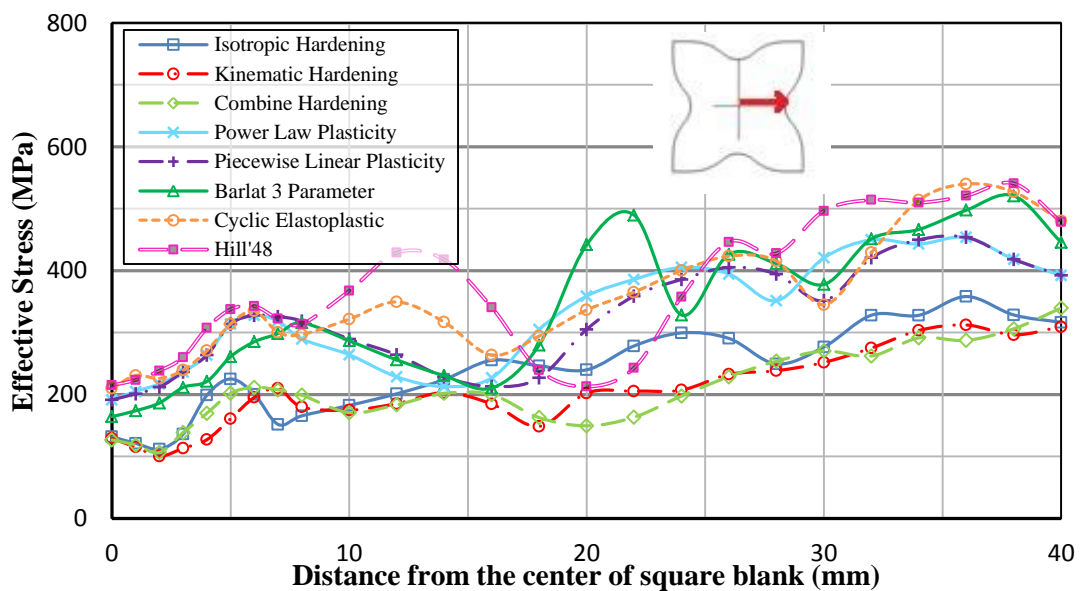


Figure 5.76: Comparison of the effective stress distributions obtained for different models for 20 mm punch travel (St12 steel, transverse direction, blank holder 4 kN).

Figures 5.77 and 5.78, the show thickness strain and the effective stress distributions of square cup drawing, respectively, in diagonal direction by considering 4 kN blank holder force for 25 mm punch displacement.

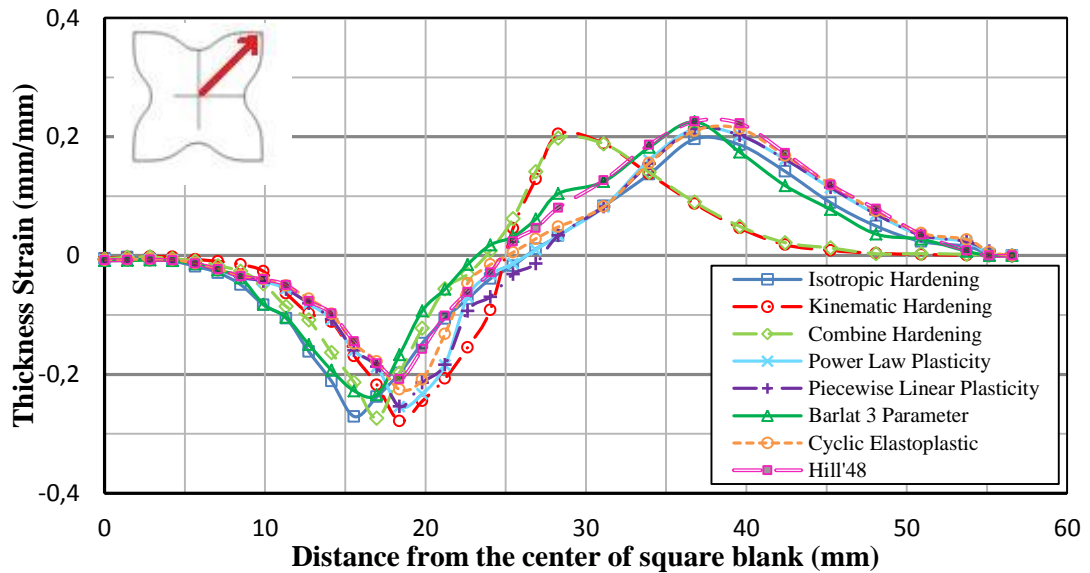


Figure 5.77: Comparison of the thickness strain distributions obtained for different models for 25 mm punch travel (St12 steel, diagonal direction, blank holder 4 kN).

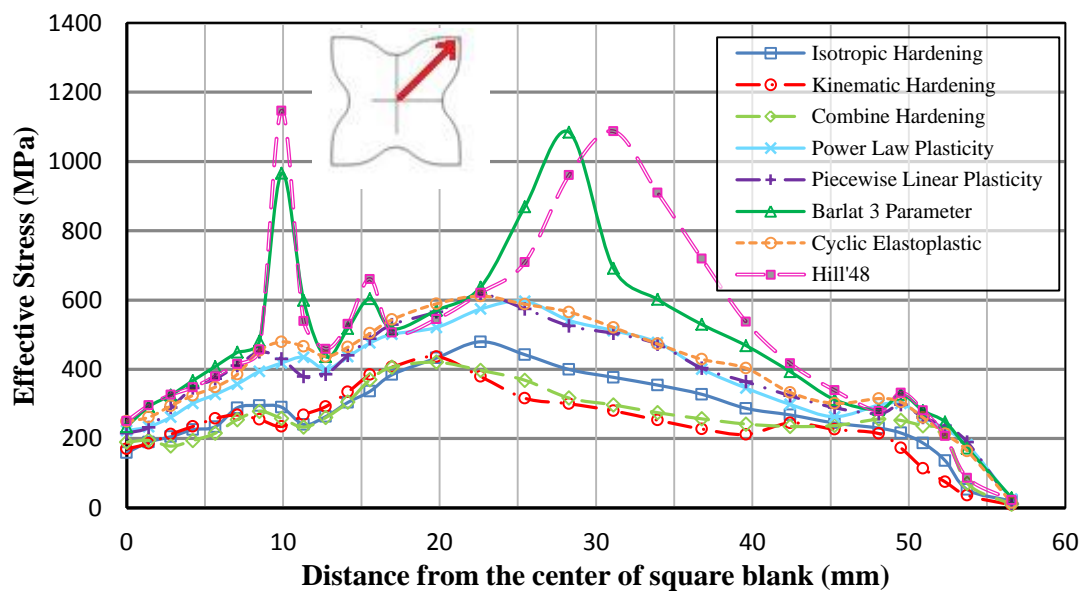


Figure 5.78: Comparison of the effective stress distributions obtained for different models for 25 mm punch travel (St12 steel, diagonal direction, blank holder 4 kN).

In Figures 5.79 and 5.80, the thickness strain and the effective stress distributions of square cup drawing are given, respectively, in transverse direction by considering 4 kN blank holder force for 25 mm punch displacement.

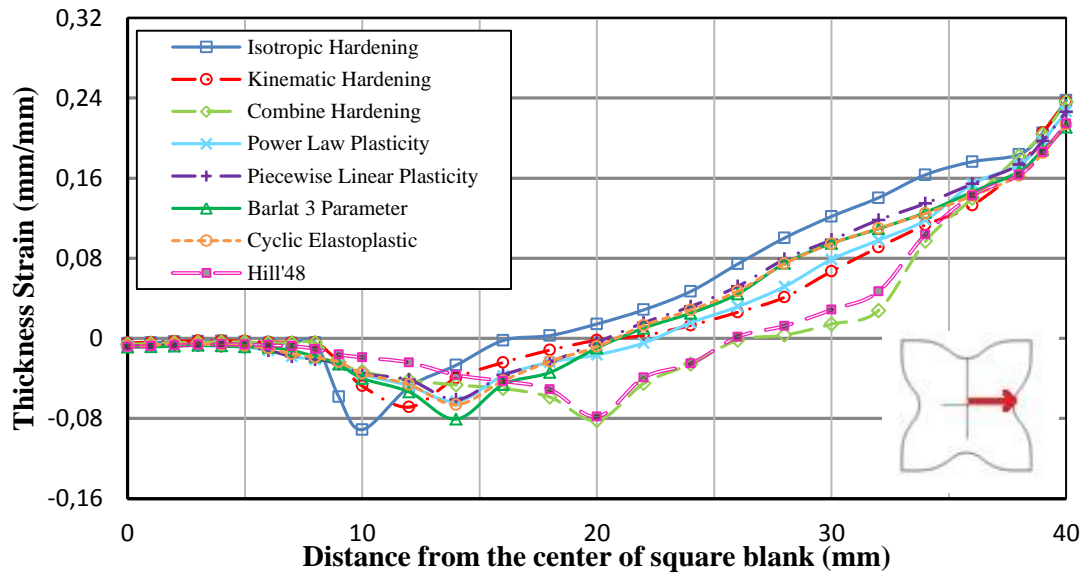


Figure 5.79: Comparison of the thickness strain distributions obtained for different models for 25 mm punch travel (St12 steel, transverse direction, blank holder 4 kN).

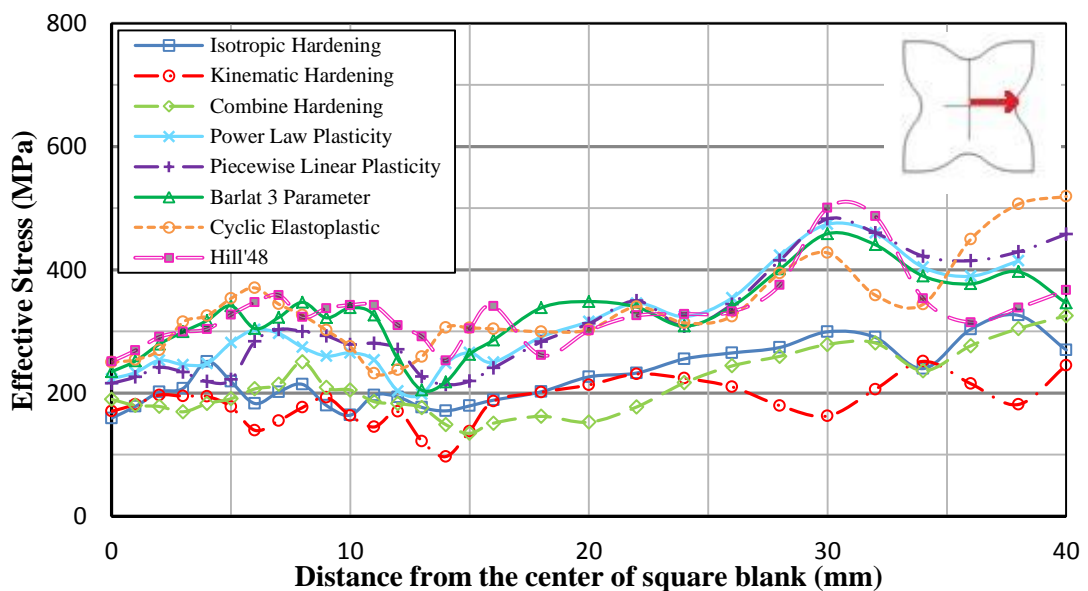


Figure 5.80: Comparison of the effective stress distributions obtained for different models for 25 mm punch travel (St12 steel, transverse direction, blank holder 4 kN).

Figures 5.81 and 5.82 show the thickness strain and the effective stress distributions of square cup drawing, respectively, in diagonal direction by considering 5 kN blank holder force for 10 mm punch displacement.

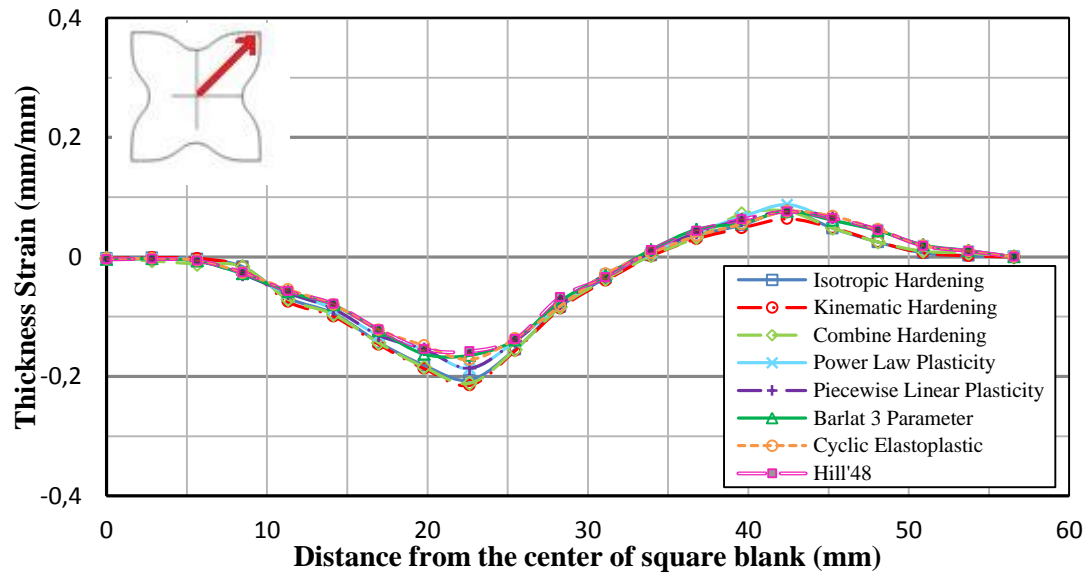


Figure 5.81: Comparison of the thickness strain distributions obtained for different models for 10 mm punch travel (St12 steel, diagonal direction, blank holder 5 kN).

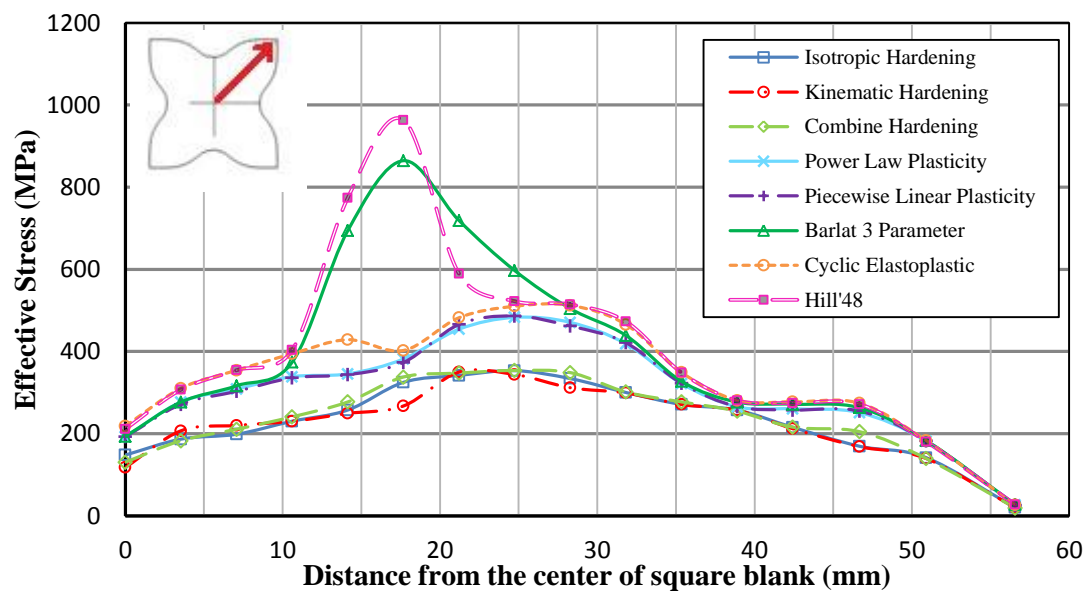


Figure 5.82: Comparison of the effective stress distributions obtained for different models for 10 mm punch travel (St12 steel, diagonal direction, blank holder 5 kN).

In Figures 5.83 and 5.84, the thickness strain and the effective stress distributions of square cup drawing are given, respectively, in transverse direction by considering 5 kN blank holder force for 10 mm punch displacement.

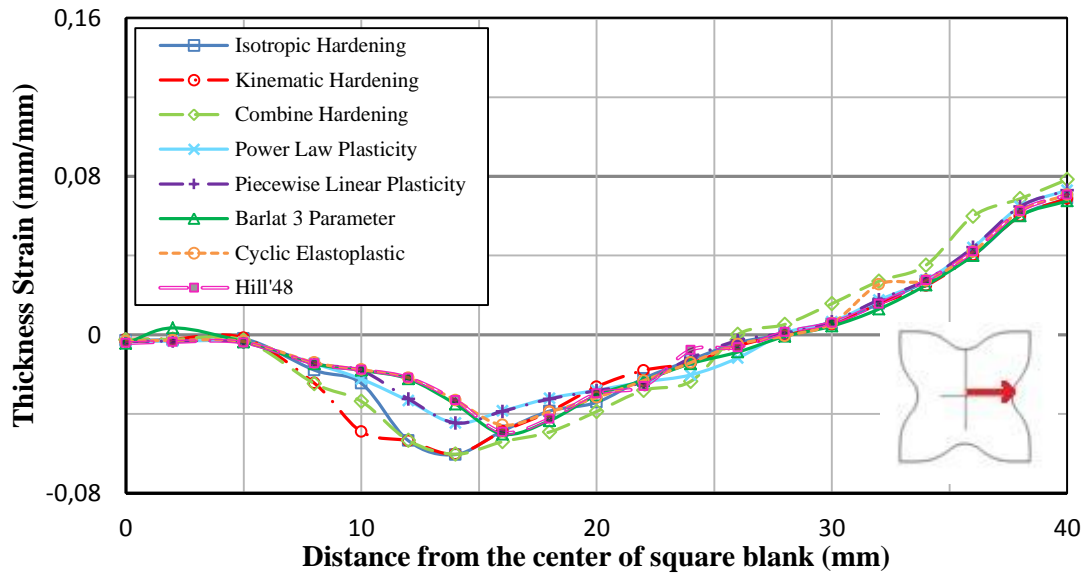


Figure 5.83: Comparison of the thickness strain distributions obtained for different models for 10 mm punch travel (St12 steel, transverse direction, blank holder 5 kN).

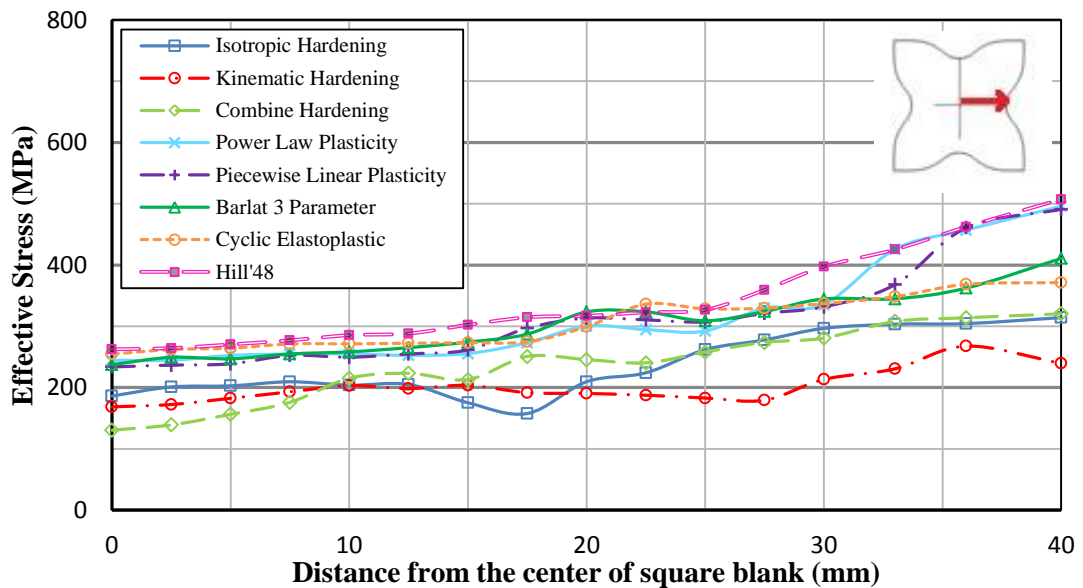


Figure 5.84: Comparison of the effective stress distributions obtained for different models for 10 mm punch travel (St12 steel, transverse direction, blank holder 5 kN).

Figures 5.85 and 5.86 show the thickness strain and the effective stress distributions of square cup drawing, respectively, in diagonal direction by considering 5 kN blank holder force for 15 mm punch displacement.

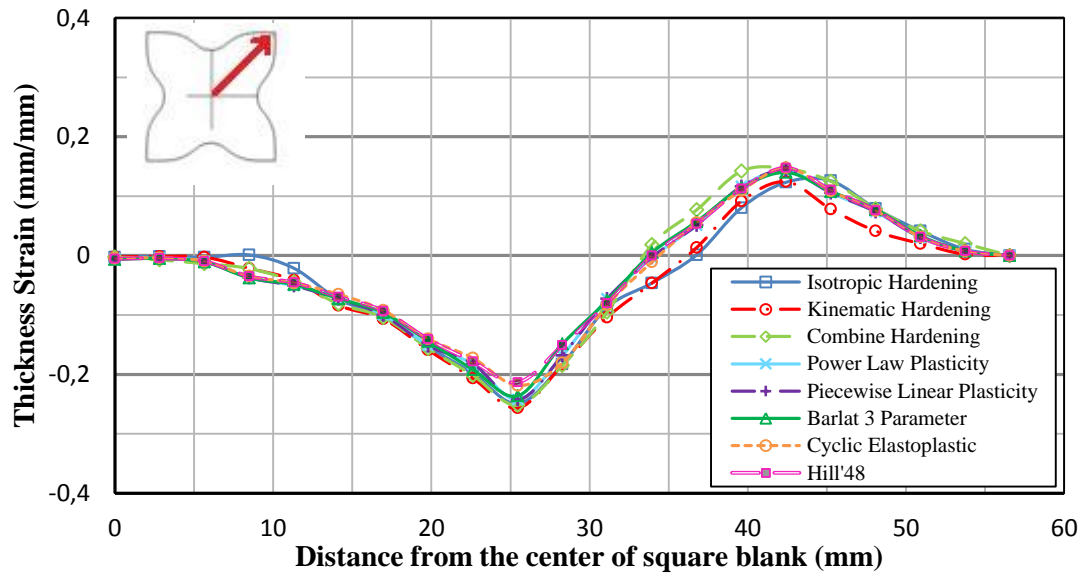


Figure 5.85: Comparison of the thickness strain distributions obtained for different models for 15 mm punch travel (St12 steel, diagonal direction, blank holder 5 kN).

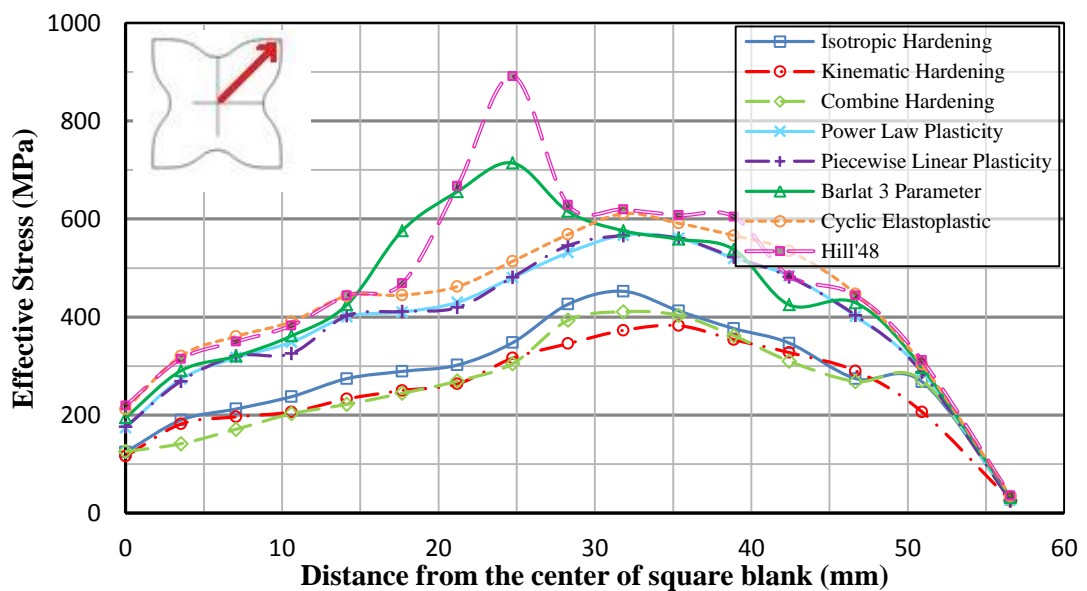


Figure 5.86: Comparison of the effective stress distributions obtained for different models for 15 mm punch travel (St12 steel, diagonal direction, blank holder 5 kN).

In Figures 5.87 and 5.88, the thickness strain and the effective stress distributions of square cup drawing are given, respectively, in transverse direction by considering 5 kN blank holder force for 15 mm punch displacement.

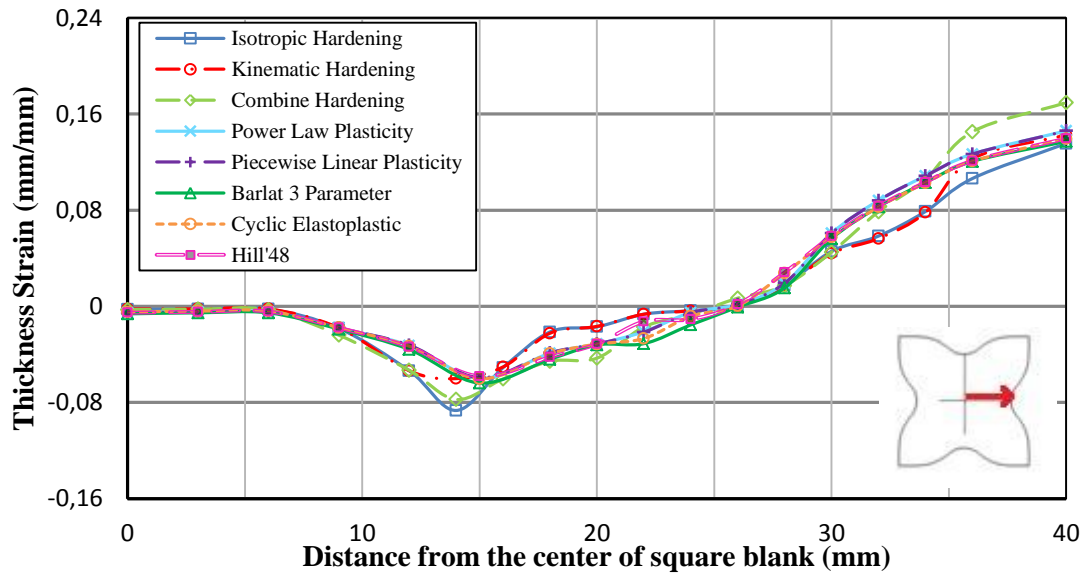


Figure 5.87: Comparison of the thickness strain distributions obtained for different models for 15mm punch travel (St12 steel, transverse direction, blank holder 5 kN).

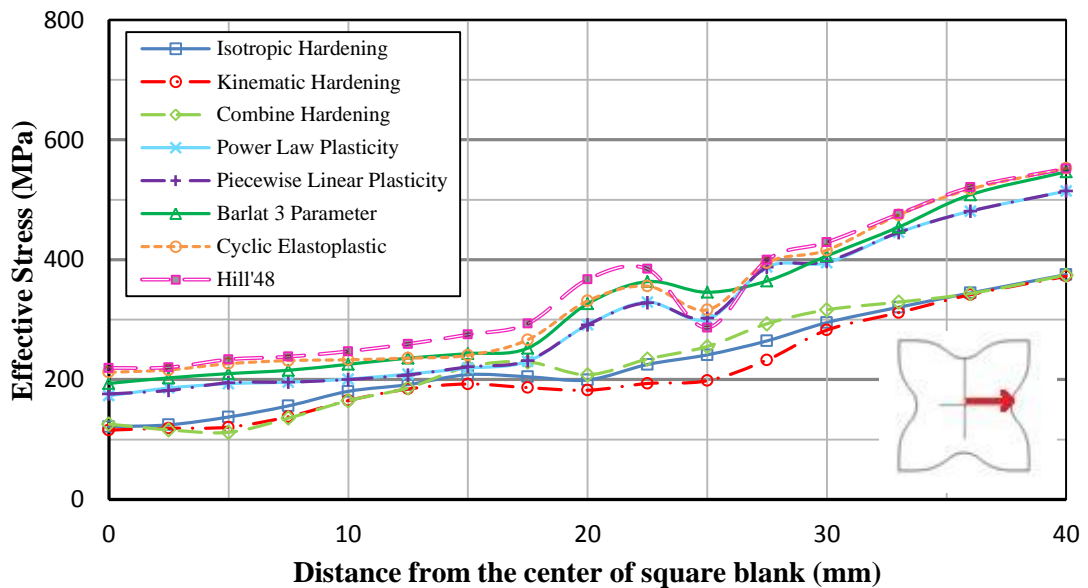


Figure 5.88: Comparison of the effective stress distributions obtained for different models for 15 mm punch travel (St12 steel, transverse direction, blank holder 5 kN).

Figures 5.89 and 5.90 show the thickness strain and the effective stress distributions of square cup drawing, respectively, in diagonal direction by considering 5 kN blank holder force for 20 mm punch displacement.

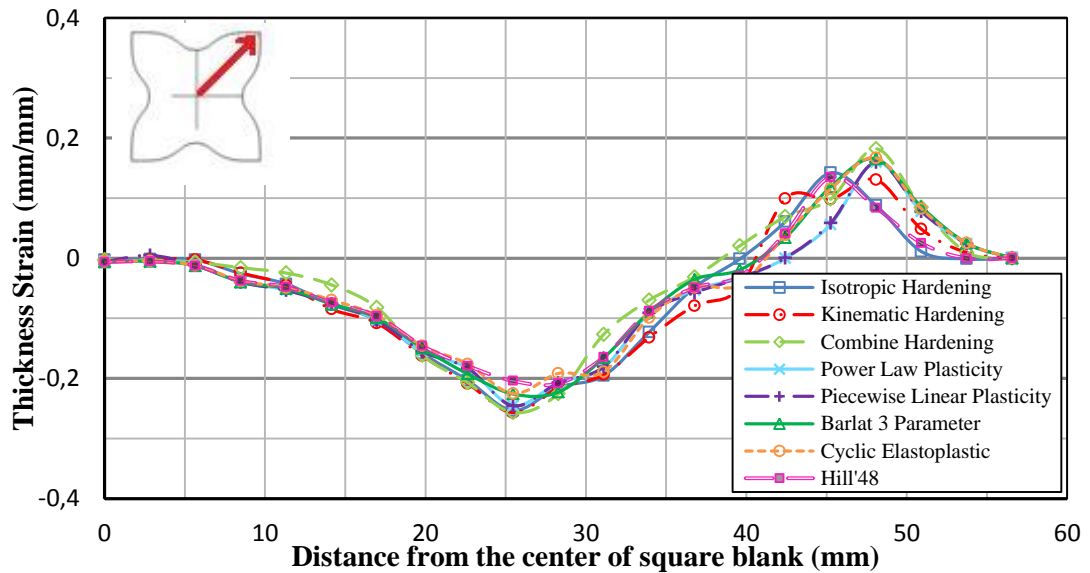


Figure 5.89: Comparison of the thickness strain distributions obtained for different models for 20 mm punch travel (St12 steel, diagonal direction, blank holder 5 kN).

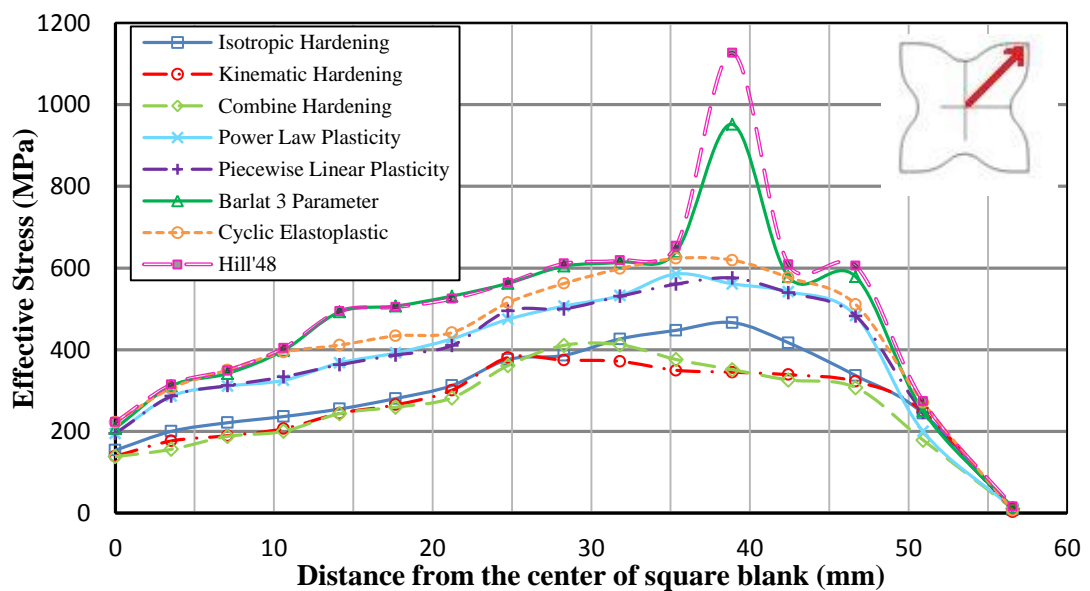


Figure 5.90: Comparison of the effective stress distributions obtained for different models for 20 mm punch travel (St12 steel, diagonal direction, blank holder 5 kN).

In Figures 5.91 and 5.92, the thickness strain and the effective stress distributions of square cup drawing are given, respectively, in transverse direction by considering 5 kN blank holder force for 20 mm punch displacement.

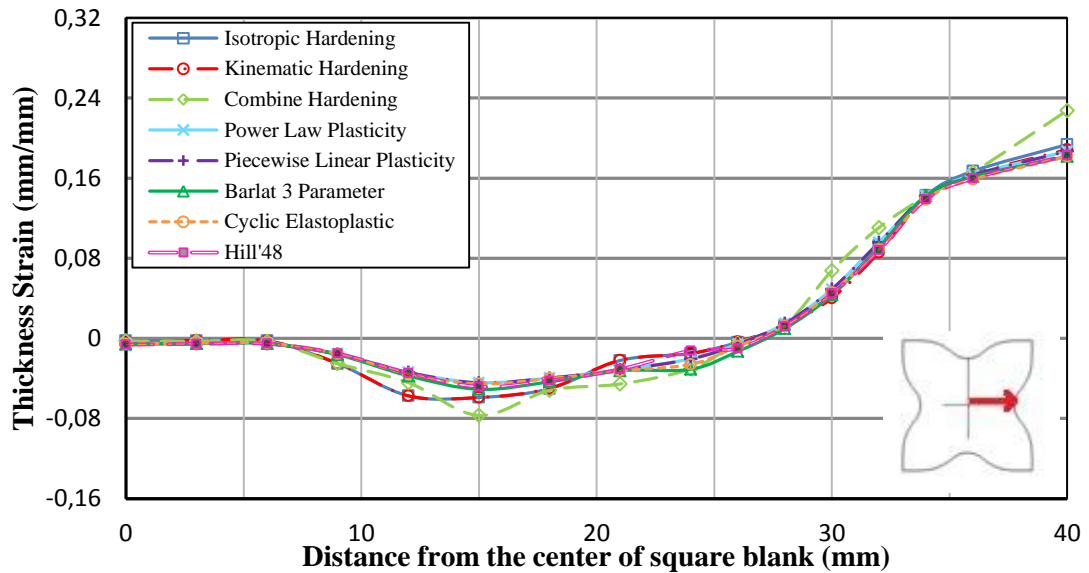


Figure 5.91: Comparison of the thickness strain distributions obtained for different models for 20 mm punch travel (St12 steel, transverse direction, blank holder 5 kN).

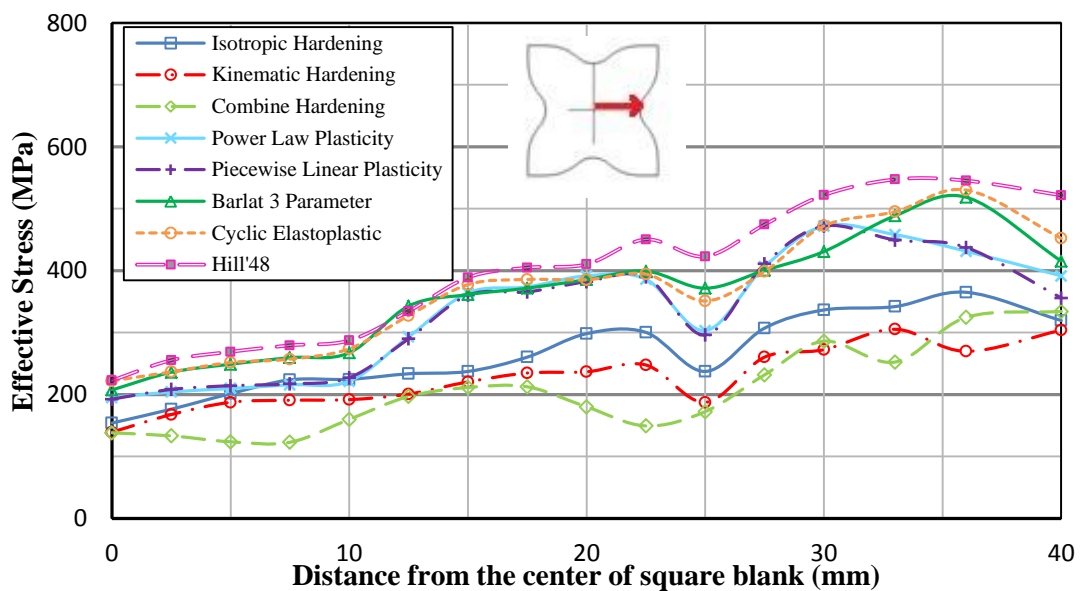


Figure 5.92: Comparison of the effective stress distributions obtained for different models for 20 mm punch travel (St12 steel, transverse direction, blank holder 5 kN).

Figures 5.93 and 5.94 show the thickness strain and the effective stress distributions of square cup drawing, respectively, in diagonal direction by considering 5 kN blank holder force for 25 mm punch displacement.

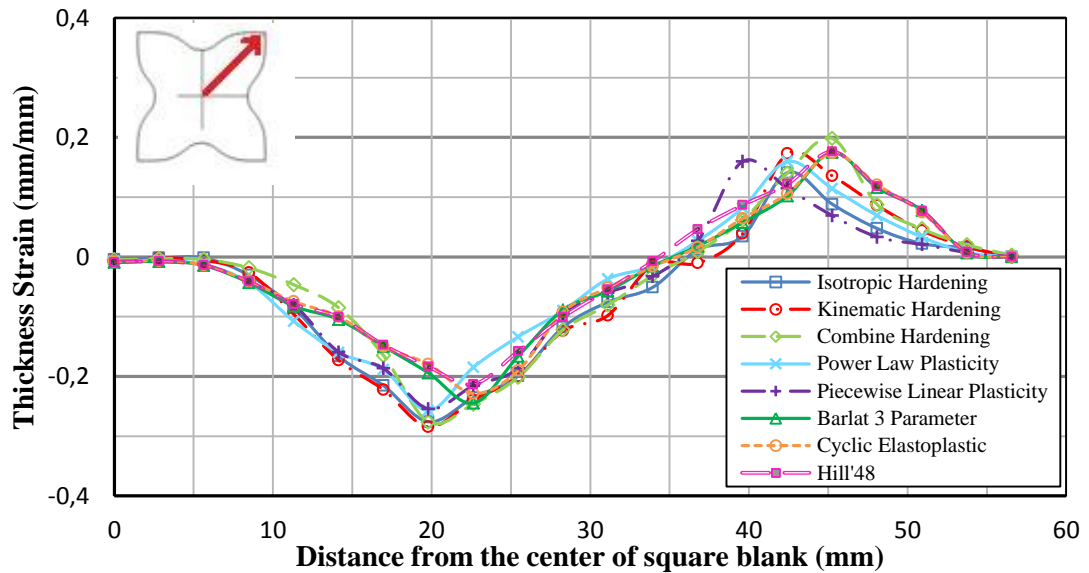


Figure 5.93: Comparison of the thickness strain distributions obtained for different models for 25 mm punch travel (St12 steel, diagonal direction, blank holder 5 kN).

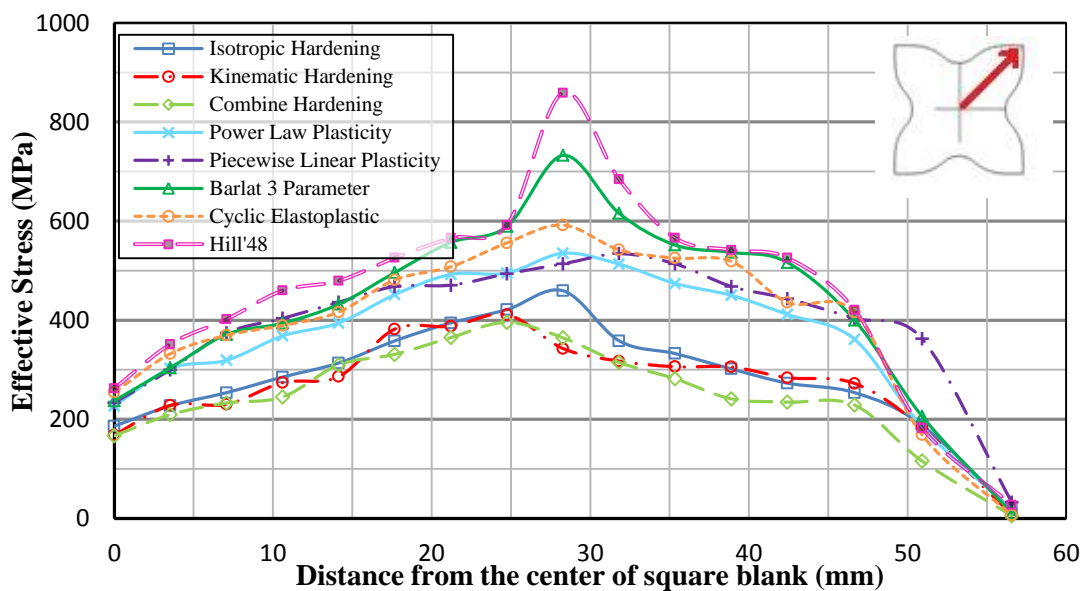


Figure 5.94: Comparison of the effective stress distributions obtained for different models for 25 mm punch travel (St12 steel, diagonal direction, blank holder 5 kN).

In Figures 5.95 and 5.96, the thickness strain and the effective stress distributions of square cup drawing are given, respectively, in transverse direction by considering 5 kN blank holder force for 25 mm punch displacement.

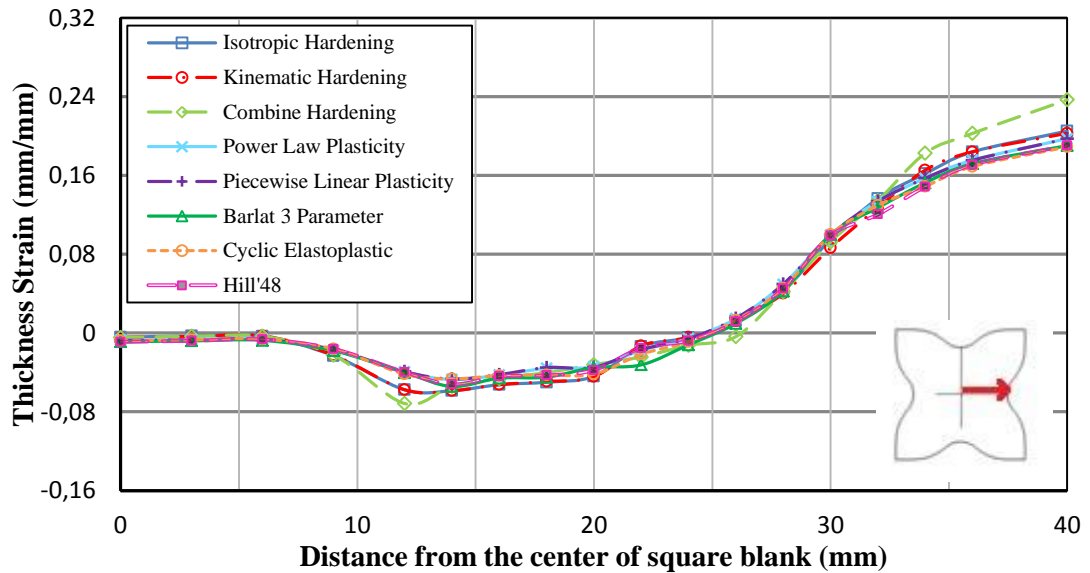


Figure 5.95: Comparison of the thickness strain distributions obtained for different models for 25 mm punch travel (St12 steel, transverse direction, blank holder 5 kN).

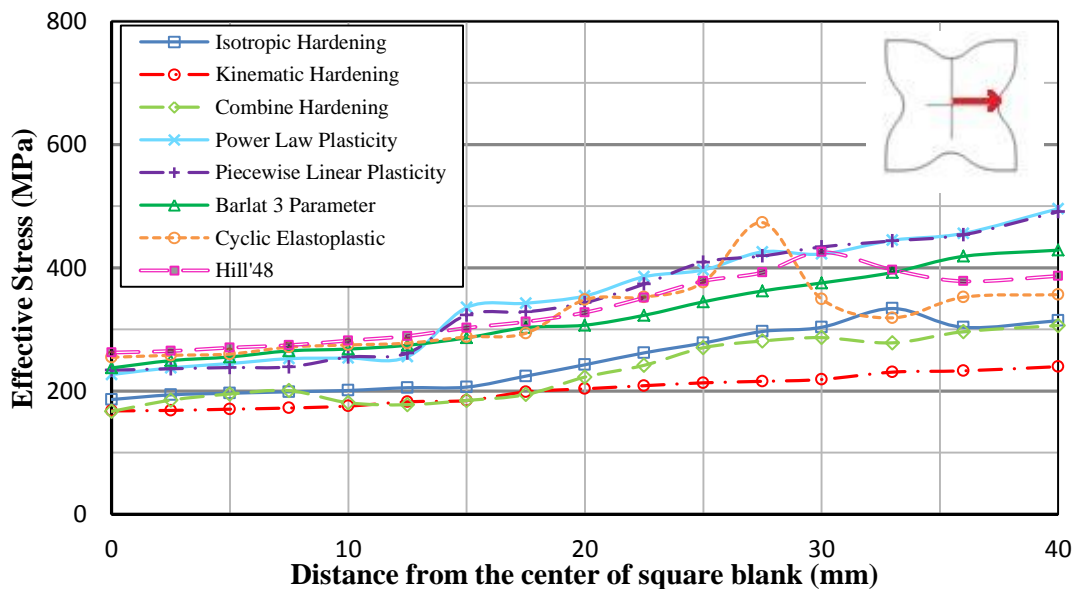


Figure 5.96: Comparison of the effective stress distributions obtained for different models for 25 mm punch travel (St12 steel, transverse direction, blank holder 5 kN).

### 5.3.4 Comparison with Experiments

In this section, comparison of the edge contours obtained by the numerical analysis for eight constitutive models with the geometries that are obtained in the experiments are given for St12 Steel. The experiments are conducted by using three different blank holder forces; 2 kN, 4 kN and 5 kN for 10 mm, 15 mm, 20 mm and 25 mm punch travels.

In Figures 5.97-5.100, comparison of the final geometries of square cup drawing are given by considering 2 kN blank holder force for 10 mm, 15 mm, 20 mm and 25 mm punch travels, respectively.

In Figures 5.101-5.104, comparison of the final geometries of square cup drawing are given by considering 4 kN blank holder force for 10 mm, 15 mm, 20 mm and 25 mm punch travels, respectively.

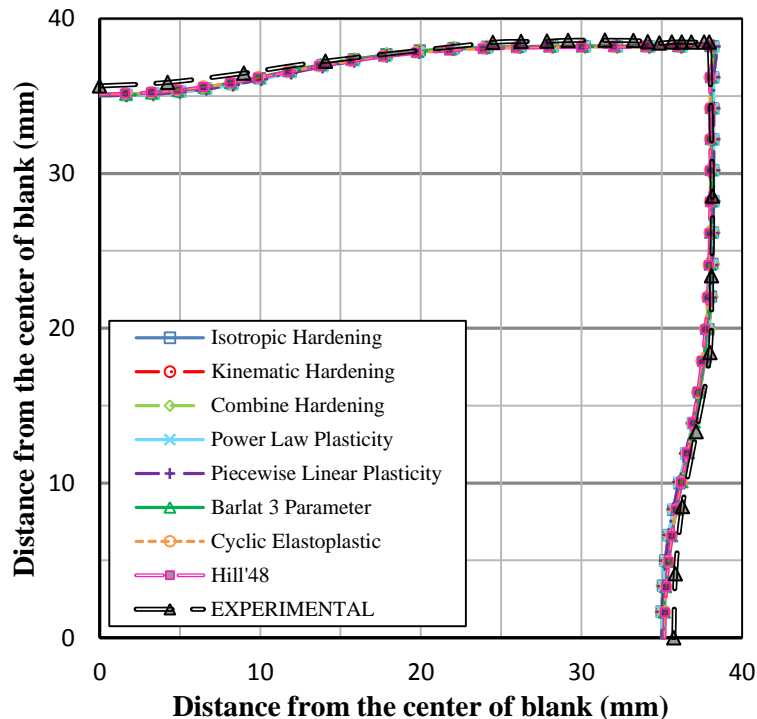


Figure 5.97: Edge contour comparison obtained for different models and experiments for 10 mm punch travel (blank holder 2 kN).

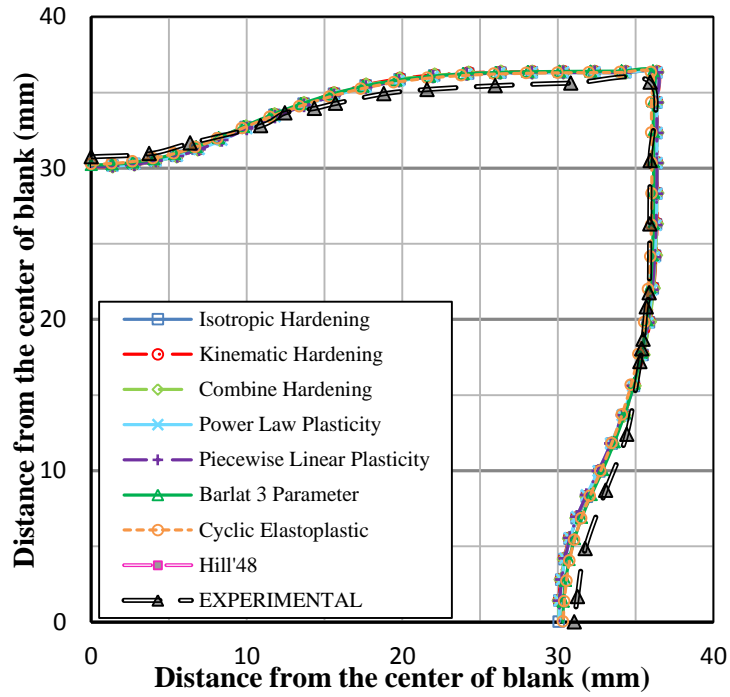


Figure 5.98: Edge contour comparison obtained for different models and experiments for 15 mm punch travel (blank holder 2 kN).

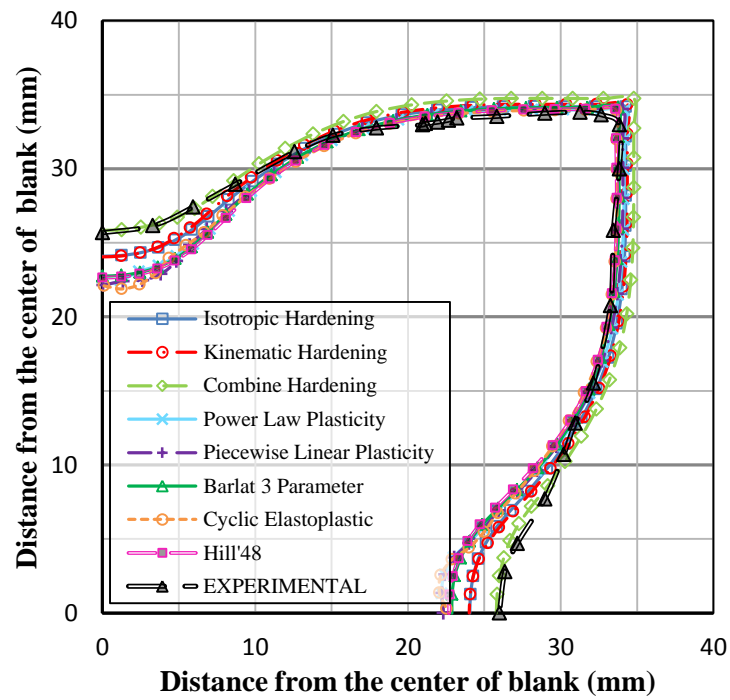


Figure 5.99: Edge contour comparison obtained for different models and experiments for 20 mm punch travel (blank holder 2 kN).

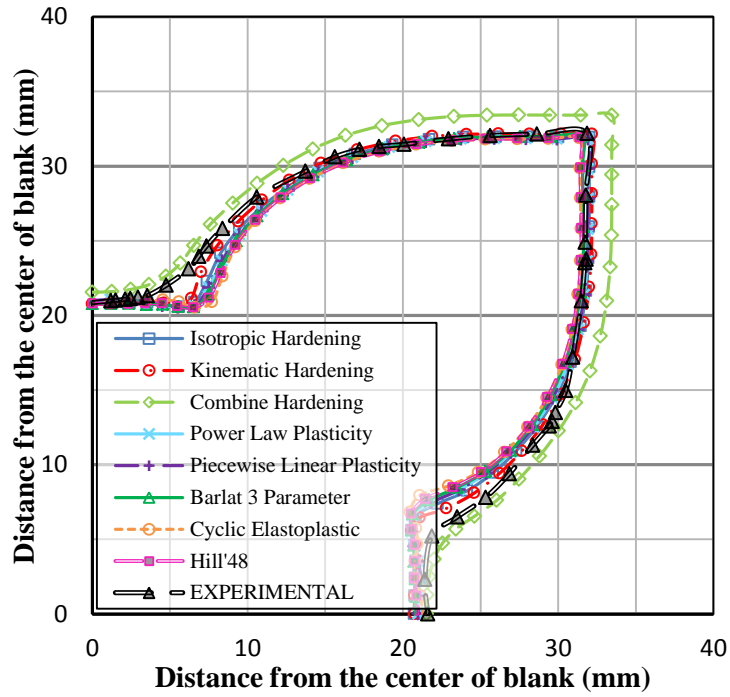


Figure 5.100: Edge contour comparison obtained for different models and experiments for 25 mm punch travel (blank holder 2 kN).

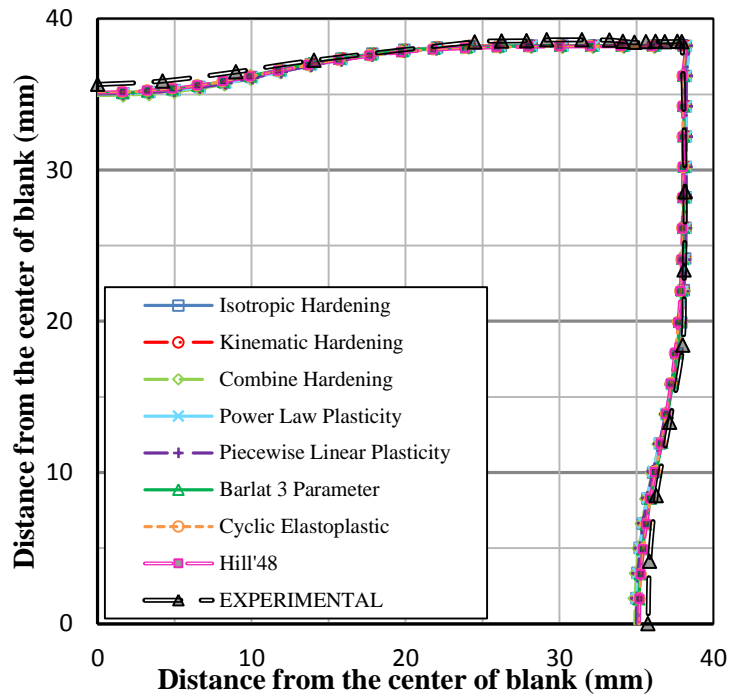


Figure 5.101: Edge contour comparison obtained for different models and experiments for 10 mm punch travel (blank holder 4 kN).

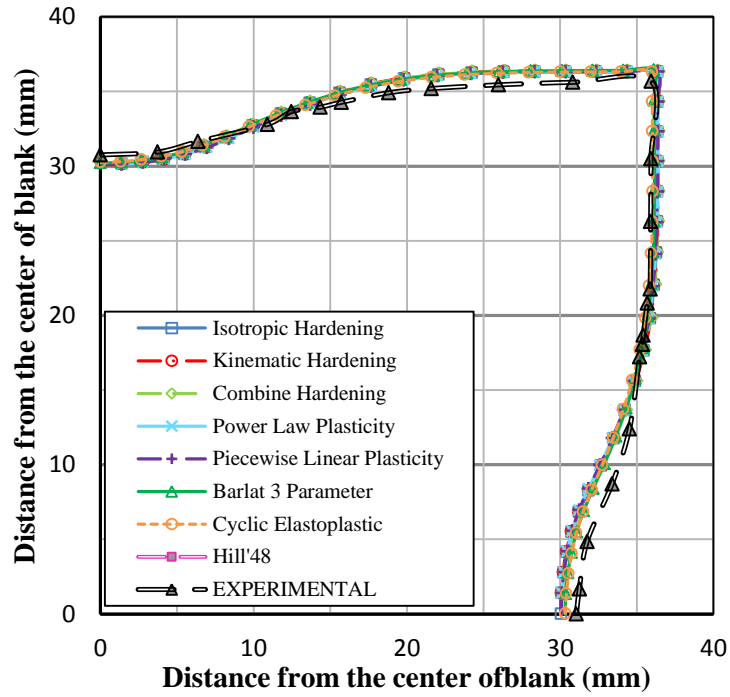


Figure 5.102: Edge contour comparison obtained for different models and experiments for 15 mm punch travel (blank holder 4 kN).

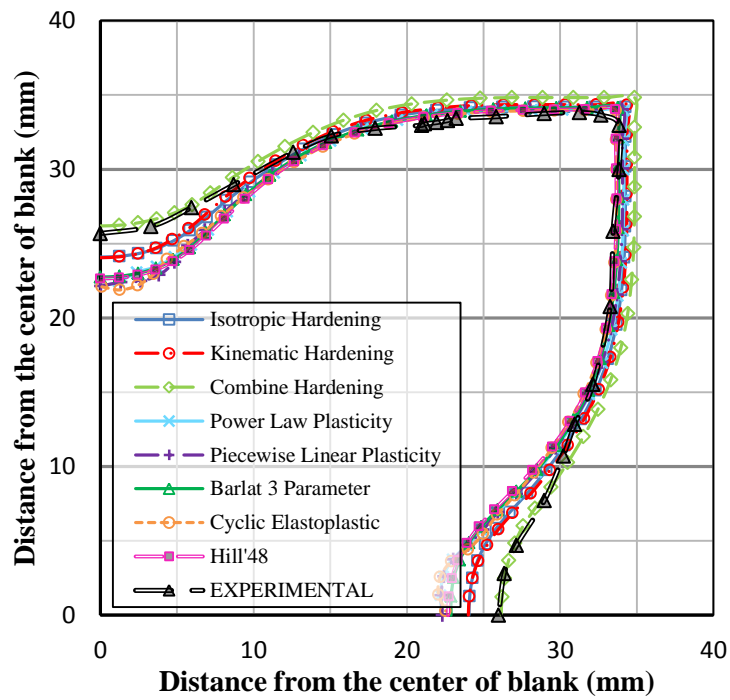


Figure 5.103: Edge contour comparison obtained for different models and experiments for 20 mm punch travel (blank holder 4 kN).

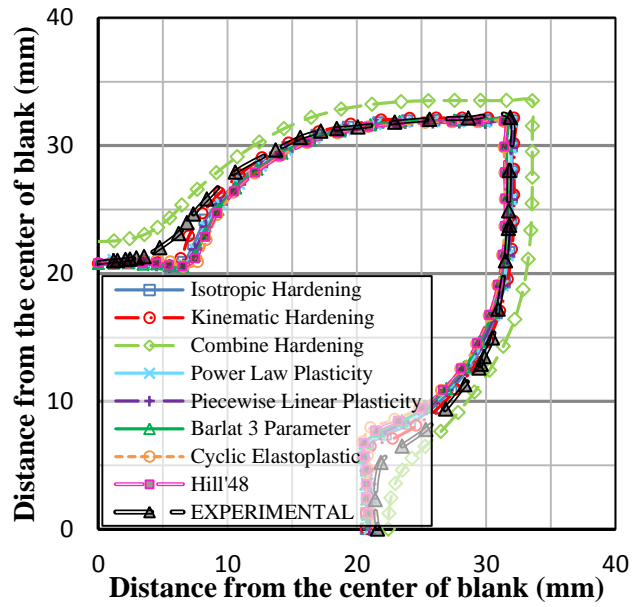


Figure 5.104: Edge contour comparison obtained for different models and experiments for 25 mm punch travel (blank holder 4 kN).

In Figures 5.105-5.108, comparison of the final geometries of square cup drawing are given by considering 5 kN blank holder force for 10 mm, 15 mm, 20 mm and 25 mm punch travels, respectively.

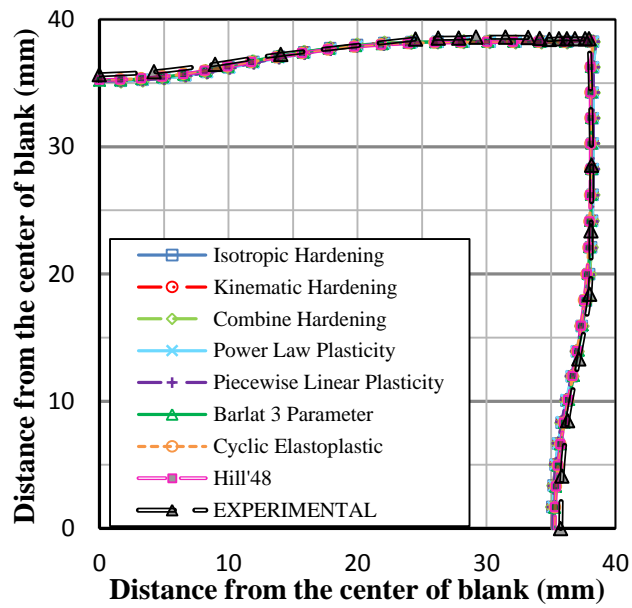


Figure 5.105: Edge contour comparison obtained for different models and experiments for 10 mm punch travel (blank holder 5 kN).

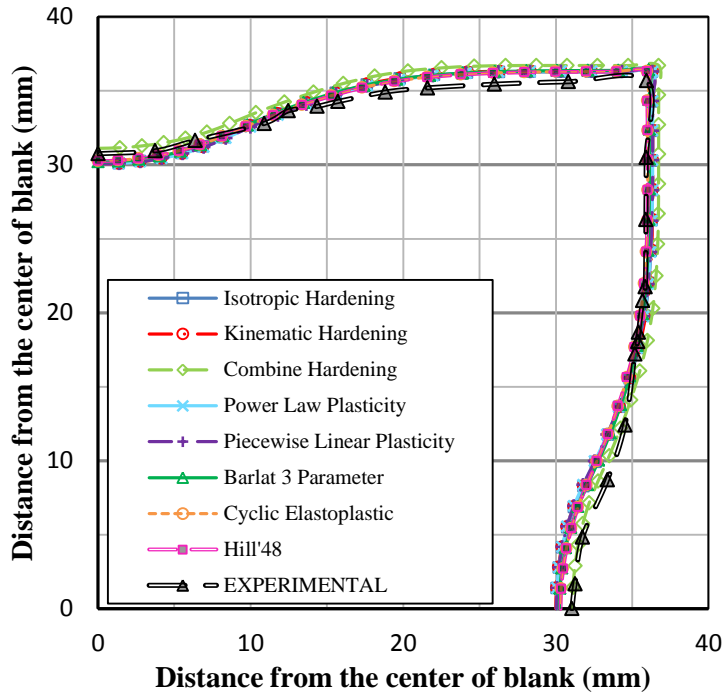


Figure 5.106: Edge contour comparison obtained for different models and experiments for 15 mm punch travel (blank holder 5 kN).

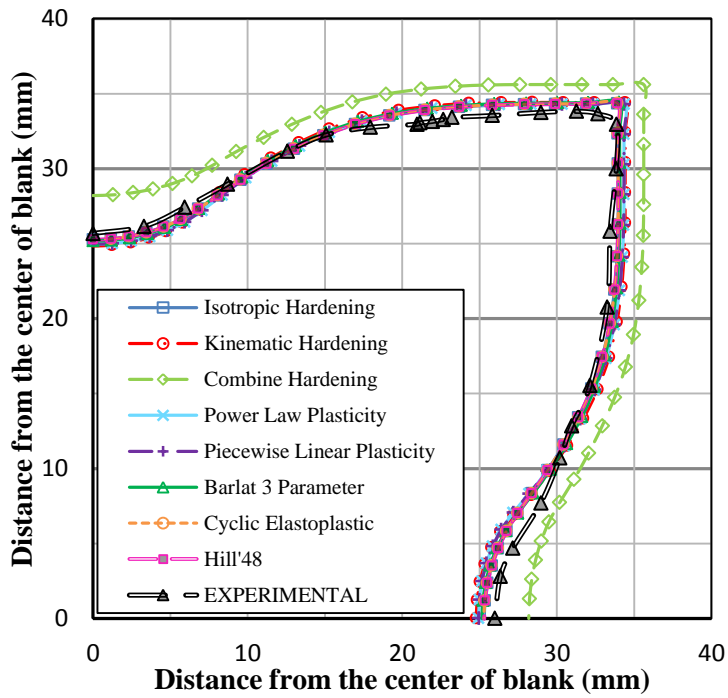


Figure 5.107: Edge contour comparison obtained for different models and experiments for 20 mm punch travel (blank holder 5 kN).

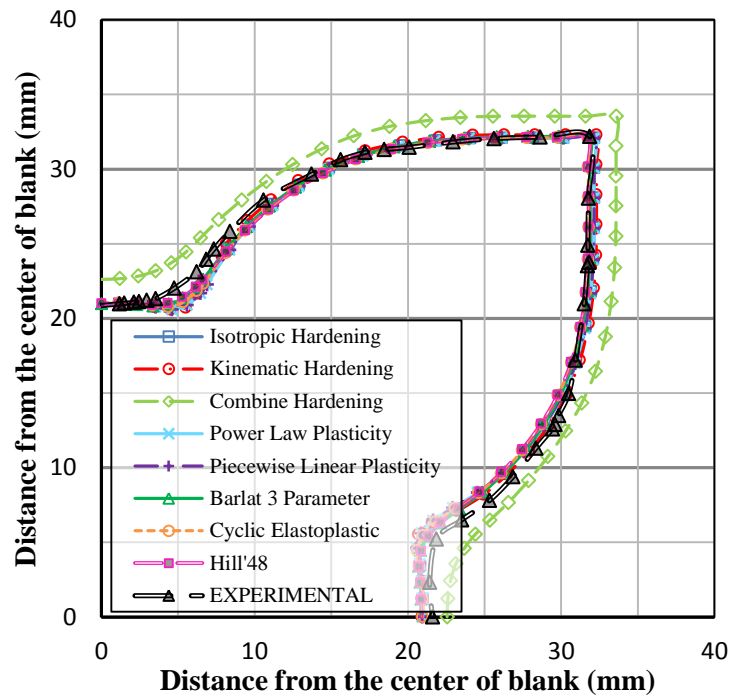


Figure 5.108: Edge contour comparison obtained for different models and experiments for 25 mm punch travel (blank holder 5 kN).

#### 5.4 V-Bending

In order to compare the effect of different constitutive models in springback prediction, V-bending operation is simulated by using St12 steel as blank material and the simulation results are compared with the experimental results. FEM model of the V-bending operation is shown in Figure 5.109.

In Figure 5.110, the comparison of the springback amounts that have been obtained from the V-bending experiment and simulations are shown.

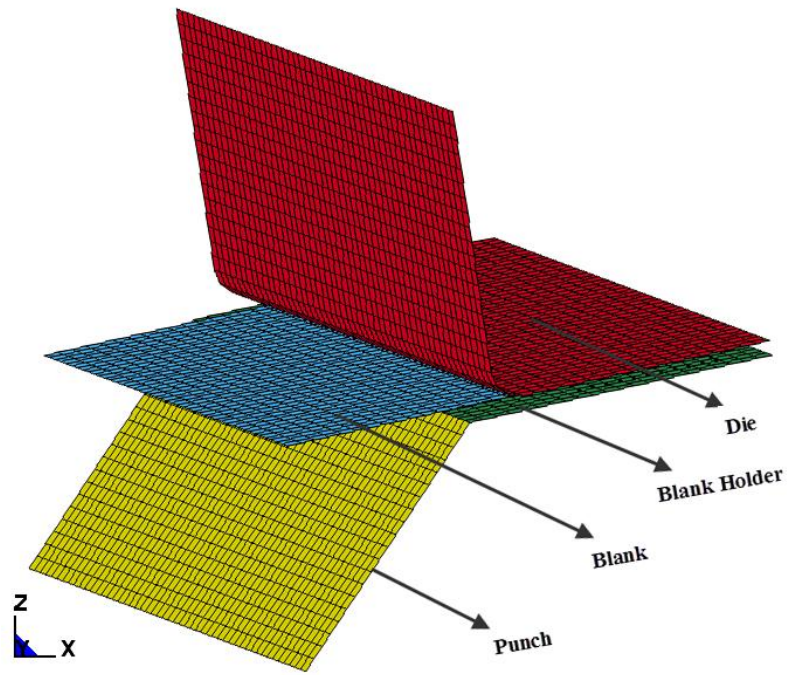


Figure 5.109: FEM model of V-bending operation.

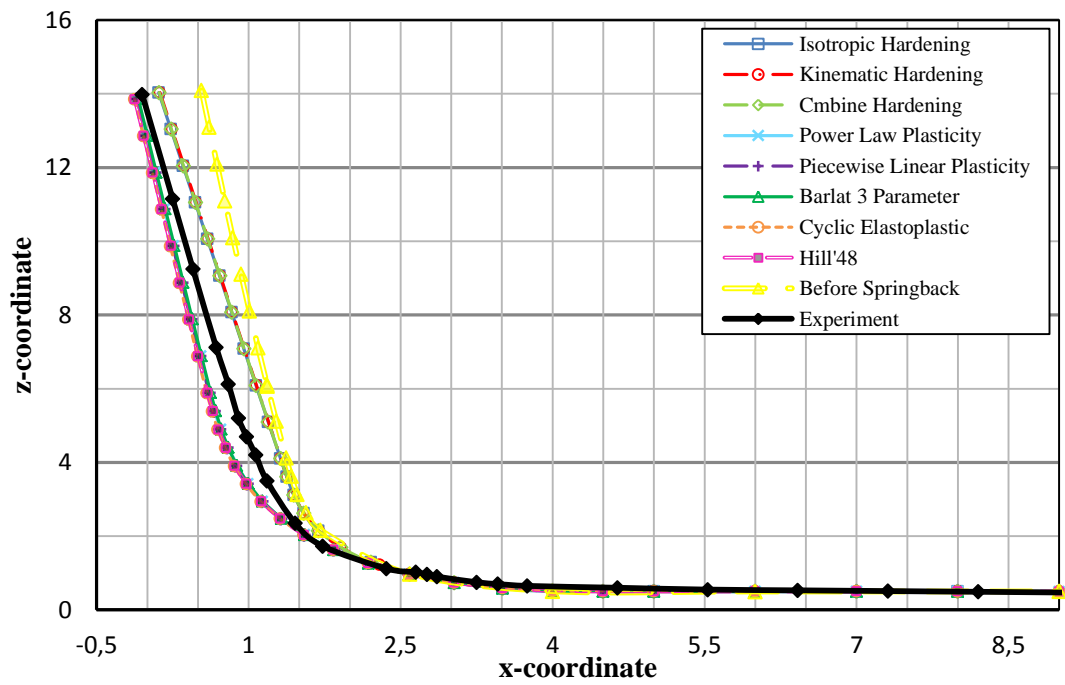


Figure 5.110: Springback amount comparison obtained for different models and experiments.

## 5.5 Comparison of the Results

The thickness strain and effective stress distributions obtained from the simulations and analytic calculations are in agreement for the flange region of the cylindrical cup, as shown in Figures 5.5 and 5.6. At the rim, all the models display a thickness strain value at about 0.08 mm/mm and the analytical calculation gives a strain value of 0.11 mm/mm. At  $r_0/R_0 \cong 0.62$ , the differences between the results of analytical calculation and the simulation for different models become minimum where cyclic elastoplastic and Hill'48 models are closer to analytic calculation results than the rest of the models.

For the effective stress distribution in cylindrical cup drawing, the isotropic, kinematic and combined hardening models produce identical results with each other. However, it is observed that, these models show the greatest difference with other constitutive models and the analytical calculation result. Specifically at the rim, this difference is the maximum, whereas at  $r_0/R_0 \cong 0.5$ , effective stress values display consistent results with the analytical solution. Other constitutive models; power law isotropic plasticity, piecewise linear isotropic plasticity, Barlat three-parameter, cyclic elastoplastic and Hill'48 give closer results to analytical calculation for effective stress distributions and the difference is minimum at  $r_0/R_0 \cong 0.62$ . Amongst the models discussed above, power law and piecewise linear isotropic plasticity are very consistent with the analytical calculation. At the rim, the analytical calculation give a higher effective stress value 810 MPa compared to power law and piecewise linear isotropic plasticity models which display a stress value of approximately 720 MPa. However, towards the center of the cylindrical cup, the differences in the stress values obtained from these two models and the analytical calculation decrease and the results are almost identical with the analytical calculation in the region  $0.50 < r_0/R_0 < 0.60$ .

The differences in effective stress and thickness strain distributions between the constitutive models and analytical calculation can be attributed to the simplification assumptions in the analytical approach. Moreover, shear stresses are also neglected in the analytical calculations of the effective stresses.

In square cup drawing, the simulation results obtained for stainless steel 409 Ni demonstrate that, the thickness strain distribution in diagonal and transverse directions for all the models show the same tendency as shown in Figures 5.17, 5.19, 5.21, 5.23, 5.25, 5.27, 5.29 and 5.31. In diagonal direction, the effective stress distributions for Hill'48 and Barlat three-parameter, which display similar characteristics, diverge significantly from the results of the other models as seen in Figures 5.18, 5.20, 5.22, 5.24, 5.26, 5.28, 5.30 and 5.32. In the transverse direction, effective stress distributions show considerable variations which increase towards the rim (Figure 12). For isotropic, kinematic and combined hardening models effective stress values can be grouped being close to each other while the other models display similar behavior. However, towards the rim, results of isotropic hardening model deviate from kinematic and combined hardening models and become closer to the other models.

For Al-5182 aluminum, thickness strain distribution obtained in diagonal and transverse directions display closer results with each other for all the constitutive models as can be observed from the Figures 5.33, 5.35, 5.37, 5.39, 5.41, 5.43, 5.45 and 5.47. However, the effective stress distributions obtained for the different models deviate significantly in diagonal direction, as seen in Figures 5.34, 5.38, 5.42 and 5.46. Effective stress distributions of kinematic and combined hardening models generally display close results. Although the rest of the models display similar behavior, in some regions the stress values obtained from the Hill'48 and Barlat three-parameter constitutive models deviate from others. In the transverse direction, for kinematic and combined hardening models effective stress distributions are close to each other and deviate from the rest of the models that display similar tendency as observed in Figures 5.36, 5.40, 5.44 and 5.48.

For the St12 steel, numerical analyses are done by considering three different blank holder forces; 2 kN, 4 kN and 5kN. The thickness strain distributions obtained in diagonal and transverse directions for 2 kN and 4 kN blank holder forces, models show similar behavior for 10 mm and 15 mm punch travels. As the punch displacement increases the behavior of the constitutive models becomes different. For 5 kN blank holder force as it is observed from the Figures 5.89, 5.91 and 5.93

that the models show almost the same behavior even for 20 mm and 25 mm punch travels.

The effective stress distributions that are obtained in the diagonal and transverse directions differ for three blank holder forces for the 10 mm and 15 mm punch travels, whereas as the displacement increases the stress values for the 2 kN blank holder forces becomes higher than the results obtained for the 4 kN and 5 kN as observed from the Figures 5.62, 5.64, 5.78, 5.80, 5.94 and 5.96. The simulation results obtained for effective stress distributions in diagonal direction show three different types of behavior regarding the constitutive models for these three different blank holder forces. The isotropic, kinematic and the combined hardening models behave close to each other, whereas Hill'48 and Barlat three-parameter models diverge significantly from the results of the others and power law isotropic plasticity, piecewise linear isotropic plasticity and cyclic elastoplastic models give similar results. In the transverse direction, effective stress distributions for isotropic, kinematic and combined hardening models display similar characteristic, whereas the distributions for power law isotropic plasticity, piecewise linear isotropic plasticity, Hill'48 and Barlat three-parameter models are in vicinity of each other as seen in Figure 5.96. For cyclic elastoplastic model the effective stress distributions various remarkably towards the rim.

Figures 5.97-5.108 show comparison of edge contours for square cup drawing obtained from the simulation results and experiments for St12 steel by considering three different blank holder forces at four different punch travels. It is observed that, all of the models are in good agreement with the experimental results for 10 and 15 mm punch displacements. When the punch displacement is more than 20 mm, the combined hardening model shows significant difference with the results of other constitutive models and experiments as seen from the Figures 5.100, 5.104, 5.107 and 5.108.

Springback amounts obtained in the simulations and experiments are in good agreement for all constitutive models in V-bending as observed from the Figure 5.110. Isotropic, kinematic and combined hardening models result in less amounts of springback compared to the experimental values. The springback amounts obtained

for power law isotropic plasticity, piecewise linear isotropic plasticity, cyclic elastoplastic, Barlat three-parameter, and Hill'48 constitutive models, display similar behavior but more springback values than that obtained by the experiments.

As a general result it can be stated that, from the comparisons for the effective stress and thickness strain distributions with analytical calculations and edge contour comparisons with experiments by considering different blank holder forces at different punch displacements; piecewise linear isotropic plasticity and power law isotropic plasticity constitutive models are better to estimate the behavior of the sheet metal in these simulations. Moreover, it can be said from these results that, the combined hardening model is not appropriate to predict the behavior of the materials considered.

## CHAPTER 6

### CONCLUSION AND FUTURE WORK

#### 6.1 Conclusion

In this study, the effects of different constitutive models in sheet metal forming are investigated by performing cylindrical cup drawing, square cup drawing and V-bending simulations. The applied constitutive models are; elastic plastic constitutive model with isotropic hardening, elastic plastic constitutive model with kinematic hardening, elastic plastic constitutive model with combined hardening, power law isotropic plasticity, piecewise linear isotropic plasticity, three-parameter Barlat, cyclic elastoplastic and Hill'48 model. From this study, the following conclusions have been obtained:

1. In cylindrical cup drawing, numerical results obtained for power law isotropic plasticity and piecewise linear isotropic plasticity models are reasonably in good agreement with analytically determined thickness strain and the effective stress distributions compared to the other models.
2. In square cup drawing, the geometries of the edge contours of the drawn cups obtained in the simulations are consistent with the experiments for all the constitutive models. However, the geometry obtained by the combined hardening model displays the highest difference with other experiments as the punch displacement becomes more than 20 mm.

3. Though the simulations for edge contours display good agreement with the experiments in square cup drawing, the stress distributions obtained for different constitutive models vary significantly within the cup.
4. For kinematic and combined hardening models, effective stress distributions display close results with each other, but give smaller stress values compared to the other models. Although the isotropic hardening model shows closer results with these two models, the effective stress distribution varies significantly.
5. For Hill'48 and Barlat three-parameter models, the effective stress distributions show close results with each other, but yield higher stress values compared to the other models.
6. For, power law isotropic plasticity, piecewise linear isotropic plasticity models, the effective stress distributions display close results with each other, with acceptable stress values compared to the other models. Although the cyclic elastoplastic model shows closer results to these two models, the effective stress distribution varies considerably in cylindrical and square cup drawing.
7. In V-bending, springback amounts that have been obtained by the simulations are in good agreement with the experiments.
8. It can be deduced that, the simulations using the power law plasticity and piecewise linear isotropic plasticity models reflect the material behavior better than the other six models in sheet metal forming operations.

## **6.2 Future Works**

Future works can be suggested as follows;

1. Further research could be performed to determine the effect of strain rate on sheet forming and constitutive models.

2. To obtain more reliable results in the finite element analyses, rather than using the material data from the used code's library, required parameters can be obtained by appropriate tests i.e., tensile test, shear test, bulge test etc.
3. Different elements could be used to model the simulations in order to show the effects of element types in the results.

## REFERENCES

- [1] S. Semiatin, "ASM Handbook, Volume 14B, Metal Working: Sheet Forming", ASM International, 2006.
- [2] Z. Marciniak, "Mechanics of Sheet Metal Forming" Butterworth-Heinemann, 2002.
- [3] C. Wang, "Mechanics of Bending, Flanging and Deep Drawing and a Computer-Aided Modeling System for Predictions of Strain Fracture Wrinkling and Springback in Sheet Metal Forming", Ph. D. Thesis in Ohio State University, 1993.
- [4] T. Altan, "Metal Forming and the Finite Element Method", Oxford University Press, 1989.
- [5] S. Semiatin, "ASM Handbook, Volume 14, Forming and Forging", ASM International, 1996.
- [6] M. Kleiner: Tiefziehen, LFU-Querschnitt, Dortmund, 2004.
- [7] H. Kuhn, D. Medlin, "ASM Handbook, Volume 8: Mechanical Testing and Evaluation", ASM International, 2000.
- [8] M. P. Groover, "Fundamentals of Modern Manufacturing Second Edition", John Wiley, 2002.
- [9] Edmundo Corona, "A Simple Analysis for Bend-Stretch Forming of Aluminum Extrusions", International Journal of Mechanical Sciences, 46, 433–448, 2004.
- [10] M. Ahmetoğlu, "A Computer Aided Engineering System for Process Design in Sheet Metal Forming", Ph. D. Thesis in Ohio State University, 1993.

- [11] W.M. Chan, H.I. Chew, H.P. Lee, B.T. Cheok, “Finite Element Analysis of Springback of V-Bending Sheet Metal Forming Processes”, *Journal of Materials Processing Technology*, 148,15–24, 2004.
- [12] Mark Colgan, John Monaghan, “Deep Drawing Process: Analysis and Experiment”, *Journal of Materials Processing Technology*, 132, 35–41, 2003.
- [13] Braxton manufacturing, web site: “<http://www.braxtonmfg.com/Braxton-Manufacturing.pdf>”, last accessed, 11 June 2011.
- [14] N. E. Abedrabbo, "Forming of aluminum alloys at elevated temperatures", Ph. D. Thesis in Michingan state University, 2005.
- [15] P.A. Eggertsen, K. Mattiasson, “On the Modeling of the Bending–Unbending Behavior for Accurate Springback Predictions”, *International Journal of Mechanical Science*, 51, 547–563, 2009.
- [16] FMA Group, web site: “<http://www.thefabricator.com/article/tc/die-basics-101-part-xv>”, last accessed, 11 June 2011.
- [17] S. Chatti, “Effect of the elasticity formulation in finite strain on springback prediction”, *Computers and Structures*, 88, 796–805, 2010.
- [18] Rui P.R. Cardoso, Jeong Whan Yoon, “Stress Integration Method for a Nonlinear Kinematic/Isotropic Hardening Model and Its Characterization Based on Polycrystal Plasticity”, *International journal of plasticity*, 25, 1684-1710, 2009
- [19] Nader Abedrabbo, Michael A. Zampaloni, Farhang Pourboghrat, “Wrinkling Control in Aluminum Sheet Hydroforming”, *International Journal of Mechanical Science*, 47, 333–358, 2005.
- [20] J. Cao and M. C. Boyce, “Wrinkling Behavior of Rectangular Plates Under Lateral Constraint”, *International Journal of Solids Structures*, 34, 153–176, 1997.
- [21] Jian Cao, Xi Wang, “An Analytical Model for Plate Wrinkling Under Tri-Axial Loading and Its Application”, *International Journal of Mechanical Sciences*, 42, 617–633, 2000.

- [22] R. Hill, “A Theory of the Yielding and Plastic Flow of Anisotropic Metals”, Proceedings of the Royal Society of London, Series A, Mathematical and Physical, 193, 281–297, 1948.
- [23] Xuechun Li, Yuying Yanga, Yongzhi Wanga, Jun Baoa, Shunping Li, “Effect of the Material-Hardening Mode on the Springback Simulation Accuracy of V-Free Bending”, Journal of Materials Processing Technology, 123, 209–211, 2002.
- [24] Luc Papeleux, Jean-Philippe Ponthot, “Finite Element Simulation of Springback in Sheet Metal Forming”, Journal of Materials Processing Technology, 125, 785–791, 2002.
- [25] J.Chung, J. M. Hulbert, “A Time Integration Algorithms for Structural Dynamics with Improved Numerical Dissipations: The Generalized (alpha) Method”, Journal of Applied Mechanics 60, 371–375, 1993.
- [26] J. B. Kim, J. W. Yoon, D. Y. Yang, “Investigation into the Wrinkling Behavior of Thin Sheets in the Cylindrical Cup Deep Drawing Process Using Bifurcation Theory”, International for Numerical Methods in Engineering, 56, 1673–1705, 2003.
- [27] Frederic Barlat, Daniel J. Lege, and John C. Brem, “A Six-Component Yield Function for Anisotropic Materials”, International Journal of Plasticity, 7, 693–712, 1991.
- [28] Yangwook Choi, "Modeling Evolution of Anisotropy and Hardening for Sheet Metals", Ph. D. Thesis in Ohio State University, 2003.
- [29] Fuh-Kuo Chen, Tyng-Bin Huang, Chih-Kun Chang, “Deep Drawing of Square Cups with Magnesium Alloy AZ31 Sheets”, International Journal of Machine Tools & Manufacture, 46, 1553–1559, 2003.
- [30] Kwansoo Chung, Myoung-Gyu Lee, Daeyong Kim, Chongmin Kim, Michael L. Wenner, Frederic Barlat, “Springback Evaluation of Automotive Sheets Based on Isotropic-Kinematic Hardening Laws and Non-Quadratic Anisotropic Yield Functions Part I: Theory and Formulation”, International Journal of Plasticity, 21, 861–882, 2005.

- [31] F. Barlat, J. C. Brem, J. W. Yoon, K. Chung, R. E. Dick, S. H. Choi, F. Pourboghrat, E. Chu, D. J. Lege, “Plane Stress Yield Function For Aluminum Alloy Sheets”, *International Journal of Plasticity*, 19, 1297-1319, 2003.
- [32] Myoung-Gyu Lee, Daeyong Kim, Chongmin Kim, Michael L. Wenner, Robert H. Wagoner, Kwansoo Chung, “Springback Evaluation of Automotive Sheets Based on Isotropic-Kinematic Hardening Laws and Non-Quadratic Anisotropic Yield Functions Part II: Characterization of Material Properties”, *International Journal of Plasticity*, 21, 883–914, 2005.
- [33] Myoung-Gyu Lee, Daeyong Kim, Chongmin Kim, Michael L. Wenner, Kwansoo Chung, “Springback Evaluation of Automotive Sheets Based on Isotropic-Kinematic Hardening Laws and Non-Quadratic Anisotropic Yield Functions Part III: Applications, *International Journal of Plasticity*”, 21, 915–953, 2005.
- [34] J. W. Yoon, S. H. Hong, “Modeling of Aluminum Alloy Sheets Based on New Anisotropic Yield Functions”, *Journal of Materials Processing Technology*, 177, 134–137, 2006.
- [35] F. Barlat, H. Aretz, J. W. Yoon, M. E. Karabin, J. C. Brem, R. E. Dick, “Linear Transformation Based Anisotropic Yield Functions”, *International Journal of Plasticity*, 21, 1009–1039, 2005.
- [36] Junehyung Kim, Wonoh Lee, Daeyong Kim, Jinhak Kong, Chongmin Kim, Michael L. Wenner, and Kwansoo Chung, “Effect of Hardening Laws and Yield Function Types on Springback Simulations of Dual-Phase Steel Automotive Sheets”, *Metals and Materials International*, 12, 293–305, 2006.
- [37] M. C. Oliveira a, J. L. Alves, B. M. Chaparro, L. F. Menezes, “Study on the Influence of Work-Hardening Modeling in Springback Prediction”, *International Journal of Plasticity*, 23, 516–543, 2007.
- [38] J. Lemaitre, J. L. Chaboche, “Mechanics of Solid Materials”, Cambridge University Press, 1990.
- [39] L. Geng, R. H. Wagoner, “Springback Analysis with a Modified Hardening Model”, SAE paper No.2000-01-0768, SAE, Inc., 2000.

- [40] F. Yoshida, T. Uemori, “A model of Large-Strain Cyclic Plasticity and Its Application to Springback Simulation”, *International Journal of Mechanical Sciences*, 45, 1687–702, 2003.
- [41] Barlat F., Lian J., “Plastic Behavior and Stretch Ability of Sheet Metals. Part I: A Yield Function for Orthotropic Sheets under Plane Stress Condition”, *International Journal of Plasticity*, 5, 51–66, 1989.
- [42] D. Banabic, H. Aretz, D. S. Comsa, L. Paraianu, “An Improved Analytical Description of Orthotropy in Metallic Sheets”, *International Journal of Plasticity*, 21, 493–512, 2005.
- [43] F. Ayari, T. Lazghab, E. Bayraktar, “Parametric Finite Element Analysis of Square Cup Deep Drawing”, *Computational Materials Science and Surface Engineering*, 1, 106–111, 2009.
- [44] Haibo Wang, Min Wan, Xiangdong Wu, Yu Yan, “The Equivalent Plastic Strain Dependent Yld2000-2d Yield Function and the Experimental Verification”, *Computational Materials Science*, 47, 12–22, 2009.
- [45] Bingtao Tang, Xiaoyang Lu, Zhaoqing Wang, Zhen Zhao, “Springback Investigation of Anisotropic Aluminum Alloy Sheet with a Mixed Hardening Rule and Barlat Yield Criteria in Sheet Metal Forming”, *Materials and Design*, 31, 2043–2050, 2010.
- [46] Ravindra K. Saxena, P.M. Dixit, “Prediction of Flange Wrinkling in Deep Drawing Process Using Bifurcation Criterion”, *Journal of Manufacturing Processes*, 12, 19–29, 2010.
- [47] J. W. Yoon, F. Barlat, R. E. Dick, M. E. Karabin, “Prediction of Six or Eight Ears in a Drawn Cup Based on a New Anisotropic Yield Function”, *International Journal of Plasticity*, 22, 174–193, 2006.
- [48] Aboozar Taherizadeh, Daniel E. Green, Abbas Ghaei, Jeong-Whan Yoon, “A Non-Associated Constitutive Model with Mixed Isotropic-Kinematic Hardening for Finite Element Simulation of Sheet Metal Forming”, *International Journal of Plasticity*, 26, 288–309, 2010.

- [49] N. Ivaylo Vladimirov, Michael P. Pietryga, Stefanie Reese, “Anisotropic Finite Elasto Plasticity with Nonlinear Kinematic and Isotropic Hardening and Application to Sheet Metal Forming”, *International Journal of Plasticity*, 26, 659–687, 2010.
- [50] R. Tirupathi Chandrupatla, D. Ashok Belegundu, “Introduction to Finite Elements in Engineering”, Third Edition, Prentice Hall, 2002.
- [51] Robert D. Cook, David S. Malkus, Micheal E. Plesha, “Concepts and Application of Finite Element Analysis”, Third Edition, John Wiley, 1989.
- [52] Singiresu S. Rao, “The Finite Element Method in Engineering”, Fourth Edition, Elsevier Science & Technology Books, 2004.
- [53] David V. Hutton, “Fundamentals of Finite Element Analysis”, Mc Graw Hill, 2004.
- [54] K. Nielsen, "Sheet Metal Forming Simulation Using Explicit Finite Element Methods", Ph.D. Thesis in Aalborg University, 2000.
- [55] Lakshmi G. Narasaiah, “Finite Element Analysis”, BS Publication, 2008.
- [56] J. N. Reddy, “An Introduction to nonlinear Finite Element Analysis”, Oxford University Press, 2004.
- [57] S. S. Bhavikatti, “Finite Element Analysis”, New Age International (P) Publishers, 2005.
- [58] Peter Wriggers, “Nonlinear Finite Element Methods”, Springer, 2008.
- [59] Remo M. de Souza, "Force-based Finite Element for Large Displacement Inelastic Analysis of Frames", Ph. D. Thesis in University of California, 2000.
- [60] Klaus J. Bathe, “Finite Element Procedures in Engineering Analysis”, Prentice Hall, 1982.
- [61] John O. Hallquist, “Ls-Dyna Theory Manual”, Livermore Technology Corporation, 2006.
- [62] J. Wang, “Principles of the Draw Bend Springback Test”, Ph. D. Thesis in Ohio State University, 2004.

- [63] E. Van der Giessen, Theodore Y. Wu, “Advanced Applied Mechanics”, Volume 34, Academic Press, 1998.
- [64] Richard K. Boger, “Non-Monotonic Strain Hardening and Its Constitutive Representations”, Ph. D. Thesis in Ohio State University, 2006.
- [65] D. Banabic, “Sheet Metal Forming Processes Constitutive Modeling and Numerical Simulation”, Springer, 2010
- [66] S. Neto, D. Peric, Drj Owen, “Computational Methods for Plasticity, Theory and Applications”, Willey, 2008.
- [67] Brain W. Plunkett, “Plastic Anisotropy of Hexagonal Closed Packed Metals”, Ph.D. Thesis in University of Florida, 2005.
- [68] D. Banabic, E. Dannenmann, “Prediction of The Influence of Yield Locus on the Limit Strains in Sheet Metals”, Journal of Material processing Technolgy, 109, 9-12, 2001.
- [69] Li Zhang, “On Sheet Metal Formability Under Stretch Bending”, Ph. D. Thesis in Oakland University, 2009.
- [70] F. Barlat, R. C. Becker, Y. Hayashida, Y. Maeda, M. Yanagawa, K. Chung, J. C. Brem, D. J. Lege, K. Matsui, S. J. Murtha and S. Hattori, “Yielding Description for Solution Strengthened Aluminum Alloys”, International Journal of Plasticity, 13, 385-401, 1997
- [71] F. Barlat, Y. Maeda, K. Chung, M. Yanagawa, J. C. Brem, Y. Hayashida, D. J. Lege, K. Matsui, S. J. Murtha, S. Hattori, R. C. Becker and S. Makosey, “Yield Function Development for Aluminum Alloy Sheets, Mechanical Physics Solids”, 45, 1727-1763, 1997
- [72] J. Jackiewicz, “Assessing Coefficients of The Barlat Yield Criterion for Anisotropic Aluminum Alloy Sheets by Means of the Evolutionary Strategy”, Materials and Manufacturing Processes, 24 375–383, 2009
- [73] Ls-Dyna's Material Library
- [74] W. Johnson, P. B. Mellor, “Engineering Plasticity”, London, New York, Van Nostrand Reinhold Co., 1973.